the Energy to Lead

gti

FINAL PUBLIC REPORT

GTI PROJECT NUMBER 21500

EMAT Sensor for Small Diameter and Unpiggable Pipe
-- Final Public Report
Contract Number: DTPH56-13-T-000007

Report Issued: February 3, 2015

Prepared For:
U.S. Department of Transportation
Pipeline and Hazardous Materials Safety Administration
Office of Pipeline Safety
Joe Mataich
(404) 832-1159
joseph.mataich@dot.gov

Team:

Team Project Manager:
Maureen Droessler
Operations Technology Development
maureen.droessler@otd-co.org

Daniel Ersoy - GTI
R&D Exec. Director, Infrastructure
Gas Technology Institute
daniel.ersoy@gastechnology.org

Phil Bondurant – Quest Integrated
Vice President - Engineering
Quest Integrated, Inc.
P.Bondurant@qi2.com

Qi2 Team
Phil Bondurant, Hara Kannajosyula, Tony Mactutis, and Ron Lilley

Gas Technology Institute
1700 S. Mount Prospect Rd.
Des Plaines, Illinois 60018
www.gastechnology.org

Legal Notice

This information was prepared by Gas Technology Institute ("GTI") for DOT/PHMSA (Contract Number: DTPH56-13-T-000007).

Neither GTI, the members of GTI, the Sponsor(s), nor any person acting on behalf of any of them:

a. Makes any warranty or representation, express or implied with respect to the accuracy, completeness, or usefulness of the information contained in this report, or that the use of any information, apparatus, method, or process disclosed in this report may not infringe privately-owned rights. Inasmuch as this project is experimental in nature, the technical information, results, or conclusions cannot be predicted. Conclusions and analysis of results by GTI represent GTI's opinion based on inferences from measurements and empirical relationships, which inferences and assumptions are not infallible, and with respect to which competent specialists may differ.

b. Assumes any liability with respect to the use of, or for any and all damages resulting from the use of, any information, apparatus, method, or process disclosed in this report; any other use of, or reliance on, this report by any third party is at the third party's sole risk.

c. The results within this report relate only to the items tested.

Table of Contents

List of Figures

List of Tables

Executive Summary

This project successfully developed a bench-scale electromagnetic acoustic transducer (EMAT) sensor that can ultimately be used to assess small diameter and unpiggable pipelines containing reduced diameter fittings and other restricting features. The design is centered around the capability to find and characterize cracks in welds and pipe walls, as well as being platform independent, allowing integration with multiple piggable and unpiggable pipe inspection platforms.

Pipeline failure due to cracks and other planar manufacturing and construction defects is one of the core causes of gas pipeline failures. For example, there are well documented failures due to low frequency electrical resistance welded (LF-ERW) seam defects, hook cracks, low quality lap seams, and selective seam corrosion. A working EMAT sensor for smaller diameter transmission pipelines will allow operators to detect cracks and other tightly fitting defects in these pipelines that could lead to pipeline failure.

The project started with a detailed survey which was sent to ~ 20 operators with smaller diameter, high pressure transmission lines to establish the new technology need and operator requirements. The survey results were combined with the results of an in-depth literature search on EMAT technology to establish the design requirements of the sensor. The project then developed, in conjunction with internal QUEST funding, a unique design tool to aid in the acoustic/physical geometry selection of the EMAT sensor which incorporated the effects of the sensor physical shape, drive spectra, wall and coating thicknesses; and also provided a time domain output as a function of the EMAT geometry, operating frequency, wall thickness, beam divergence, and energy distribution across the wall cross-section. A sensor geometry design and operating points were selected. Parametric 2D and 3D FEA modeling was completed to aid in the confirmation of the results from the EMAT design tool and to determine the response of the guided waves to simulated cracks. A verification of the 2D model against published work was completed.

The sensor was constructed and refined and the sensor mounting design was completed. The sensor prototype was tested on precision machined defects and naturally cracked pipe. Finally the sensor went through wear testing.

The prototype was successful in detecting cracks on both pipe and flat plate and demonstrated superior wear resistance. The design considerations, requirements, and testing results are included in this report.

The recommended next step is to develop the EMAT sensor into a field-ready prototype capable of being tested with various defects and testing conditions in a controlled, unpressurized field environment. Based on controlled field testing, refinements to the sensor would be made in an iterative manner. The sensor could then ultimately be combined onto a platform, and any necessary industry certifications completed, leading up to a field demonstration on a live gas line and commercialization.

Project Objective

The objective for this project is to develop a bench-scale electromagnetic acoustic transducer (EMAT) sensor that can be used to assess small diameter and unpiggable pipelines containing reduced diameter fittings and other restricting features. The EMAT sensor will be designed to find and characterize cracks in welds and pipe walls. The EMAT sensor will be platform independent, allowing integration with multiple piggable and unpiggable pipe inspection platforms. Follow on work would construct and test a field prototype and ultimately commercialize the technology. The research will enable natural gas pipeline operators to identify traditionally difficult to find and assess defects and therefore improve system integrity and public safety.

Introduction

This report summarizes the work completed for Pipeline and Hazardous Materials and Safety Administration (PHMSA) and Operations Technology Development (OTD).

This Final Report integrates the series of project deliverables which included:

1. Requirements Definition Report
2. EMAT Sensor Design Report
3. EMAT Sensor Mounting Design Report
4. Bench-scale EMAT Sensor Prototype
5. Prototype Testing Report

In addition to the above deliverables, four quarterly reports were provided along with monthly updates.

To best understand how the various project activities supported the project deliverables, a flow chart is provided in Figure 1 which shows the most relevant activities, dependencies and interaction. The boxes shown in bold represent the five project deliverable reports, all of which have been incorporated into this final report.

This project, combined with QUEST co-funded work, resulted in the filing of 3 provisional patents.

Acknowledgements

GTI thanks the project sponsors Pipeline and Hazardous Materials and Safety Administration and Operations Technology Development for their financial and technical support of this effort.

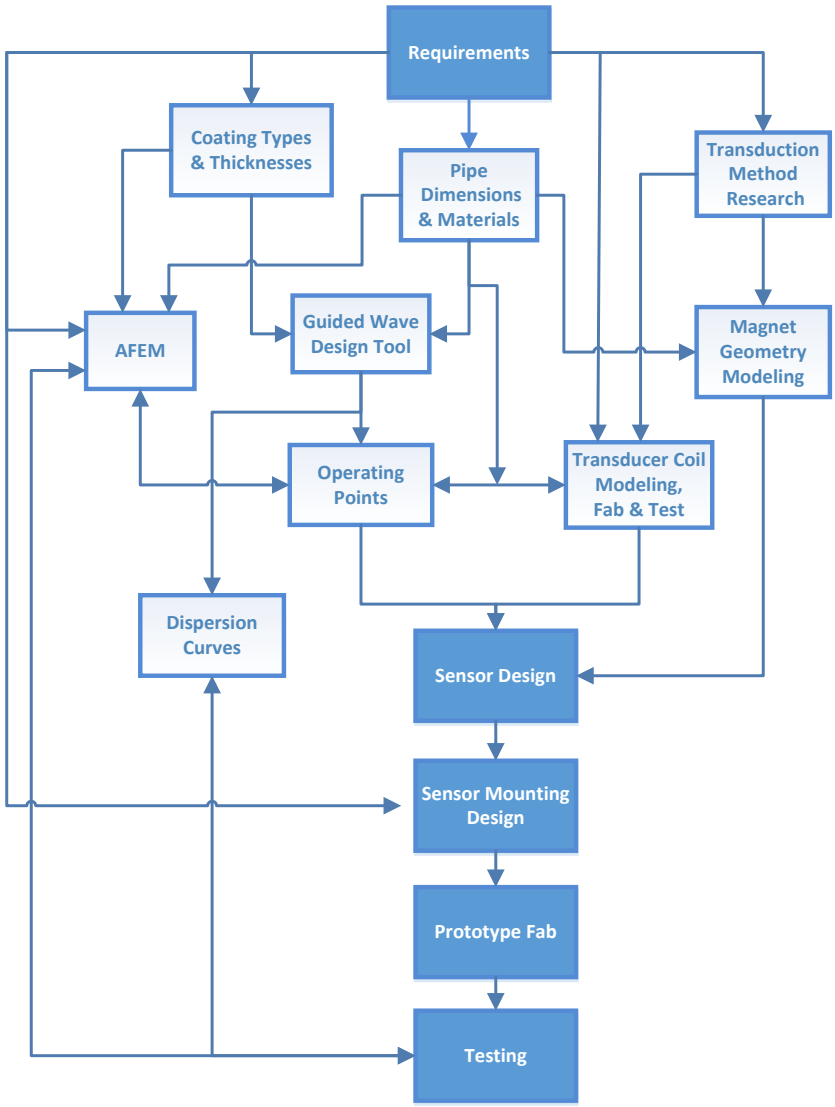

Figure 1. Flowchart Depicting Important Project Activities and their Relationships

1. Requirements

The goal of this project is to develop an EMAT sensor that can detect axial defects that would fail a typical construction hydrotest (currently required by the Federal Code).

This section summarizes the tool requirements for the proposed sensor and subsequent tool.

The primary focus for the sensor development under this project is the detection of axially oriented flaws. Axial flaws generate larger hoop stress as compared to similar size defects in the radial direction (that generate axial stress). This focus is reinforced by the observation that a great majority (> 95%)[1] of failures are caused by axially oriented defects that are perpendicular to the maximum hoop stress. Even so, the project will develop a sensor that could be reoriented for radial defects in a later project, through a sensing geometry rotation of 90 degrees.

GTI/OTD consulted with their sponsors to determine a relevant set of requirements, listed in Table 1. The most relevant requirements that drove the bench-scale prototype design included the wall thickness range, the critical flaw length, the axial speed, the initial pipeline diameter size (8”), crack orientation, crack depth resolution, bend radius and collapsibility. In addition, as part of the requirement development, a table of coating types and thicknesses developed. The coating and wall thicknesses are used to set the operating point and determine the signal levels and the guided wave modes that would be present for a selected operating point.

The critical flaw length determines the maximum allowable sensor axial length, and the crack depth resolution along with the sensor lift-off determines the required signal-to-noise ratio requirements that ultimately drive the Probability of Detection (POD). The speed determines the axial sampling rate and how much processing can be performed as the tool traverses the pipe. The bend radius and collapsibility constrain the overall tool mechanical design as well as sets constraints on the sensor sizes that can be used.

[1] OTD LRB Project subcontractor report, "Numerical Modeling and Validation for Determination of the Leak/Rupture Boundary for Low-Stress Pipelines," by John Kiefner, K. Kolovich, and R. Francini. Kiefner & Associates, Inc. May 9, 2010, Final Report No. 10-084. Reference (38) of this OTD report indicates that thirty (30) of the 1,318 incidents (2.3%) were caused by defective girth welds. Apparently, none of these incidents was hoop-stress related. Of the thirty (30) incidents, nineteen (19) were leaks, two (2) were categorized as “other,” nine (9) were categorized as ruptures (none of which occurred in a pipeline operating at a hoop stress below 30% of SMYS), and one was a miter weld that ruptured. The common theme was poor weld quality, and the failures appeared to be confined to the girth welds. The driving force for these types of failures is the longitudinal stress in the pipe, not the hoop stress. Reference (38) is: Zelenak, P.A., Haines, H. and Kiefner, J.F., Analysis of DOT Reportable Incidents for Gas Transmission and Gathering System Pipelines 1985 through 2000. s.1., Pipeline Research Committee International, January 2004.

Table 1. New Hydrotest EMAT Tool Requirements

Direct Requirements	Low Flow
Product temperature range	40F - 90F (4.4 - 32.2 C) (1)
Product flow rate	Not Applicable (2)
Product operating pressure	Up to 1,000 psig (6,894,757 Pa) (3)
Acceptable axial tool speed range	< 1 foot/sec (30.5 cm/sec)
Maximum inspection length	A function of the locomotive platform
Typical wall thickness	0.375 inches (9.5 mm)
Maximum wall thickness	0.500 inches (12.7 mm)
Minimum wall thickness	0.25 inches (6.4 mm)
Pipeline diameter range	6 – 16 inches (15.2 – 40.6 cm); Initial target: 8 inches (20.3 cm)
Multiple wall thicknesses in a single inspection run	Not typical
Critical flaw (crack) length	Typically > 2 inches (will refine from hydrotest study) (4)
Length sizing tolerance (near critical)	TBD (from Hydrotest study) (4)
Crack depth resolution at the critical flaw length.	Typically 0.02 inches (0.5mm) at 90% POD
Crack orientation	Axial, ±10°
Crack depth resolution at small crack depths: < 3 mm	TBD (4)
Crack depth resolution at larger crack depths: > 3 mm	TBD (4)
Collapse Factor/ID clearance (percent of OD) to account for unpiggable features	85% or better (5)
Minimum bend radius	1.5xD
Bi-directionality	Yes
Crack/Metal loss/Pipe feature discrimination (POI)	Yes
Wall thickness measurement (derived requirement)	Yes
Coatings	CTE, FBE, Wax, Tapes and Wraps
Locomotion	Tethered/Crawler

Notes:

(1) **Temperature**: Range should fall between these ranges. There may be upset conditions with slightly higher or lower temperatures.

(2) **Flow Rates**: The Local Distribution Company (LDC) transmission pipeline network does not lend itself to free swimming pigs (ILI). The sensor will be mounted on a platform with locomotive means, e.g., bi-direction tethered, coiled tube, robotic, power tethered crawler, etc. Since this sensor platform will not be on a free swimming pig, flow rates are not a concern. The locomotive will be able to provide the required axial sensor speed independent of flow rate. Therefore the sensor will work over the entire expected flow rate range, i.e. its performance will be independent of the system flow rate. This proposed work would have taken into account these flow rates if free swimming locomotive systems were an option, however this is not the case.

(3) **Pressure**: Most pressures will be less than 500 psig for the LDC transmission sector, however there are a limited number of instances with higher pressures.

(4) **Critical flaw depth, length, and acuity**: OTD is currently sponsoring an Alternative-Hydro testing project that is developing critical flaw curves for planar defects (i.e., crack depth vs. length plots).

Although estimates for depth, length, and acuity could be completed without the use of this body of work, the technical team feels that the best possible project results will be achieved through the use of this new information not currently available in the public domain.

(5) **Unpiggable features and diameter**: Many LDC transmission lines have unpiggable features like non full-bore valves, diameter changes, large inner weld beads, etc. This is why a large (≥ 85%) collapsibility feature was selected. The mechanical clearance is a function of the distance needed (closer is better) to get the tool/sensor close to the wall, but also to keep wear minimized. Since gas pipe is outer diameter controlled and thickness can vary, as well as bend radius for appurtenances, one would also like to have a clearance range to account for these variations. This is the basis of the clearance values.

Flaw Sizes/Types and Material Characteristics

The flaw sizes and types will be covered in detail once the critical flaw curves are complete (see note 4 from Table 1). This will include the range from smooth metal loss to a planar crack oriented perpendicular to the applied stress. A flaw index will account for the variation between these values that results from increasing notch acuity. The material characteristics are important as they relate to the critical flaw size, not the EMAT sensor definition, design, or specification. The key material factors will be yield strength and toughness (i.e., Charpy V-notch values and K1c and J1c values) and how they affect critical flaw sizes.

2. Modeling

This section summarizes the modeling considerations and results that fed into and guided the sensor design and construction.

Transduction Methods Research

There are two transduction methods that may be exploited for generation of shear waves using EMATs in both bulk and guided wave applications; Lorentz force and magnetostriction. EMATs based on either method are acoustically similar, meaning that they are analyzed with the same guided wave design tool discussed later in this report. It is important to understand each transduction mechanism so that it is clear what aspects of the sensor design will maximize the system signal-to-noise ratio.

There are a number of conclusions and observations that were extracted from the literature. These are summarized below and provide the design basis for the sensor.

- The Lorentz force approach is better understood as the electromagnetic and acoustic models can be decoupled which allows a much simpler analysis, unlike magnetostriction which has been modeled only using numerical multi-physics simulation software. In other words, for the Lorentz force approach, the electromagnetic component and the acoustic component can be separately modeled and then combined. More EMAT researchers tend toward the Lorentz approach because of this. There is only one study (Ribichini 2010) that directly compares the two approaches in steel and it was mostly simulation with one lab experiment to confirm the simulation results at one magnetic field strength and one drive current level. Ribichini also published a more complete model/experiment with pure nickel.
- The magnetostriction approach is poorly understood. There is a model that derives the transduction parameters from magnetostriction data, but experimental results (Hirao 2003, Igarashi and Alers, 1997 & 1998) only confirms it at the higher magnetic field bias levels. There is an increased efficiency at the lower bias fields that can be used as an advantage, however the transduction efficiency does not increase linearly with bias field or coil drive current. For example, an increase in the drive current from 5 amps to 25 amps results in a 2.5 times increase in signal, not a 5 times increase.
- An interesting result from Igarashi and Alers (1997, 1998) was discovered that suggests the receiver should operate at the highest bias field while, as discussed earlier, there is a "sweet spot" for the transmitter at lower horizontal bias fields. Generally researchers quote reciprocity, that is, what is good for the transmitter is equally good for the receiver. However in this situation the receiver only has the receive current in the coil and reacts to variations in the horizontal bias field in a similar manner as the transmitter does for low drive currents. As a result, the sensor design will allow for different bias fields between the transmitter and receiver modules. The principle of reciprocity is valid only for linear systems. Magnetostriction is not a linear phenomenon and this non-linearity is likely the reason for this non-intuitive behavior.

- Work performed by Tuboscope (Aron 2005) and funded by DOE tried both approaches and selected the magnetostriction approach because both provided similar signal-to-noise ratios. However there were no specifics of the test provided. Magnetostriction was selected for ease of packaging.

A summary of the results are discussed in the Transducer Coil Modeling, Fabrication and Test section.

Guided Wave Design Tool

Signals obtained by a system that employs guided waves can often be very complex to analyze. This complexity, however, can be controlled at the stage where the guided wave is being generated in the structure. Transduction techniques to control this complexity are known as mode selection or control. EMAT based transduction is an example of such techniques. There are several competing factors such as material properties, pipe wall thickness, presence of coating, etc. that influence the output of an EMAT that in turn influences the design of the EMAT itself. Therefore it is necessary to develop a tool that can be used to, at the least, qualitatively visualize the impact of these factors in a unified manner. Further, gaps have been found in literature on the understanding of the role of different parameters.

The aim of the EMAT tool design software (ETDS) is to incorporate these requirements and to enable efficient design decision making and provide a tool that will allow better understanding of testing results.

Consider Figure 2a which shows color coded dispersion curves for SH guided waves in a plate of 8.4 mm. The color variation on the dispersion curves corresponds to the relative strength (blue=0, red=1) by which a guided wave mode might be excited due to a given set of EMAT parameters.

Conventional knowledge suggests that EMATs essentially enable selection of a guided wave mode(s) that coincides with intersection of straight-line slope determined from the EMAT physical characteristics and the dispersion curves. This straight line corresponds to the spatial period (or wavelength) or alternately the spatial frequency (the wavenumber) of the EMAT elements as demonstrated in Figure 2a.

Only an increase in total energy is suggested as the attribute affected by the number of turns of a meander coil or the number of PPM elements that typically form the transduction elements of the EMAT. Therefore, the presumption is that mode selection can be achieved merely by using very few elements and its purity can be improved merely by increasing the number of cycles in the electrical excitation which leads to a narrowing of frequency bandwidth, as demonstrated by the color weighted regions between the lines corresponding to f-bandwidth in Figure 2a and b.

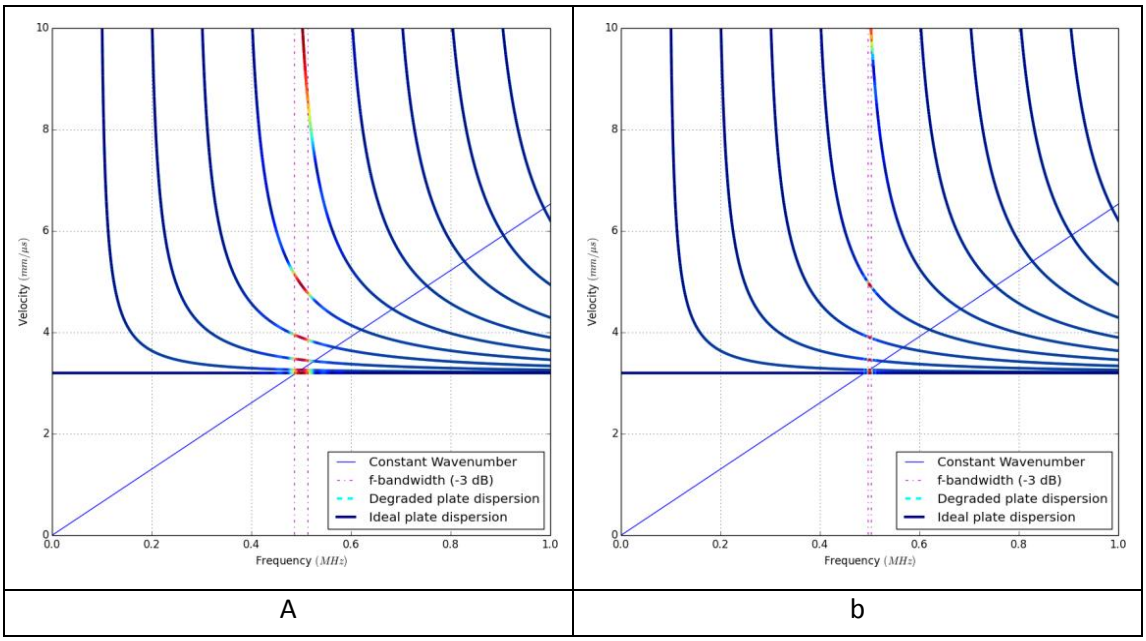

Figure 2. Traditional Understanding of EMAT Action in the SH Wave Dispersion Space

a) Broad frequency bandwidth for 16 cycle sinusoid pulse excitation
b) Narrow frequency bandwidth or 64 cycle sinusoid pulse excitation
Dispersion curves are for a steel plate of wall-thickness 16.8 mm
with a bulk shear wave velocity of 3.2 $mm/\mu s$

Recent advances in ultrasonic transduction theory that consider the transducer as a spatial-temporal filter suggest that all transducers have a wavenumber or wavelength bandwidth in addition to a frequency bandwidth. In the case of EMAT, the wavelength bandwidth is inversely proportional to the number of elements within the transducer. In the dispersion space, the wavenumber or wavelength bandwidth may be indicated in a manner similar to the frequency bandwidth. Figure 3 demonstrates an example of the wavenumber bandwidth distribution in the dispersion space for a meandering coil EMAT with 10 turns, 6.4 mm pitch and 1.6 mm trace width. Transducer designers must therefore consider the effect of both the wavenumber bandwidth and frequency bandwidth of their design.

An example of a case is shown in Figure 4 where the frequency bandwidth in Figure 2 is combined with the wavenumber bandwidth of Figure 3. Figure 4 predicts that all the modes corresponding to the region enclosed by the frequency bandwidth lines, as well as the wavenumber bandwidth lines, will be the predominant modes that will be generated in the plate. The design tool also provides for logarithm response weighting. This allows lower amplitude modes to be understood. This was particularly useful once the EMAT tool was fabricated, to understand specific responses as flaw signals can be quite small.

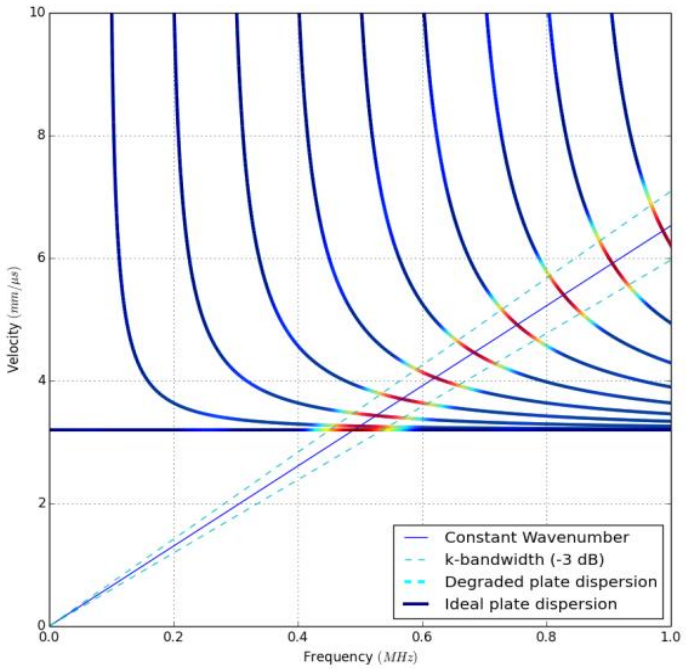

Figure 3. Demonstration of Wavenumber Bandwidth in the SH Wave Dispersion Space

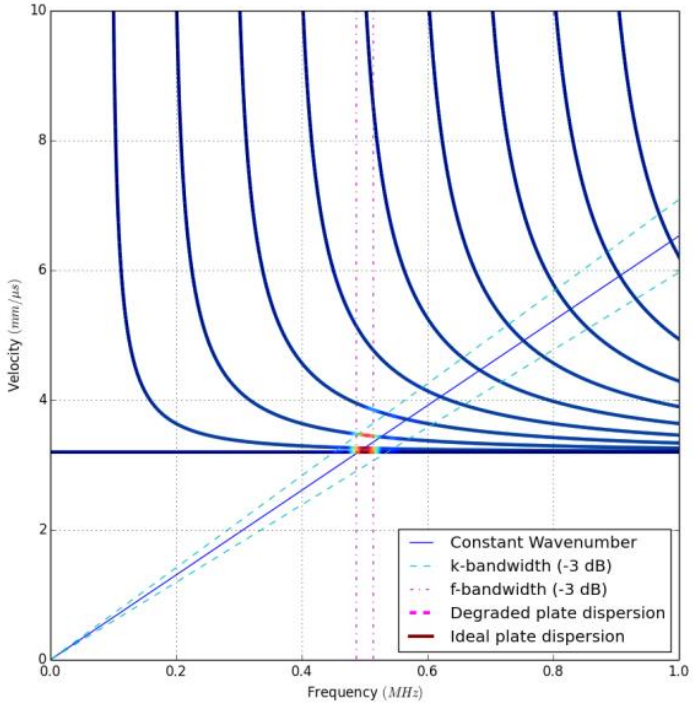

Figure 4. Combined Effect of Frequency and Wavenumber Bandwidth

Figure 5 is an ETDS screen capture of both the phase and group velocity dispersion curves on an epoxy coated plate. Note the difference in the phase velocity and group velocity curves between uncoated and coated. The group velocity curve has periodic dips due to the coating properties. The modal structure shows the particle velocity in both the steel and the epoxy.

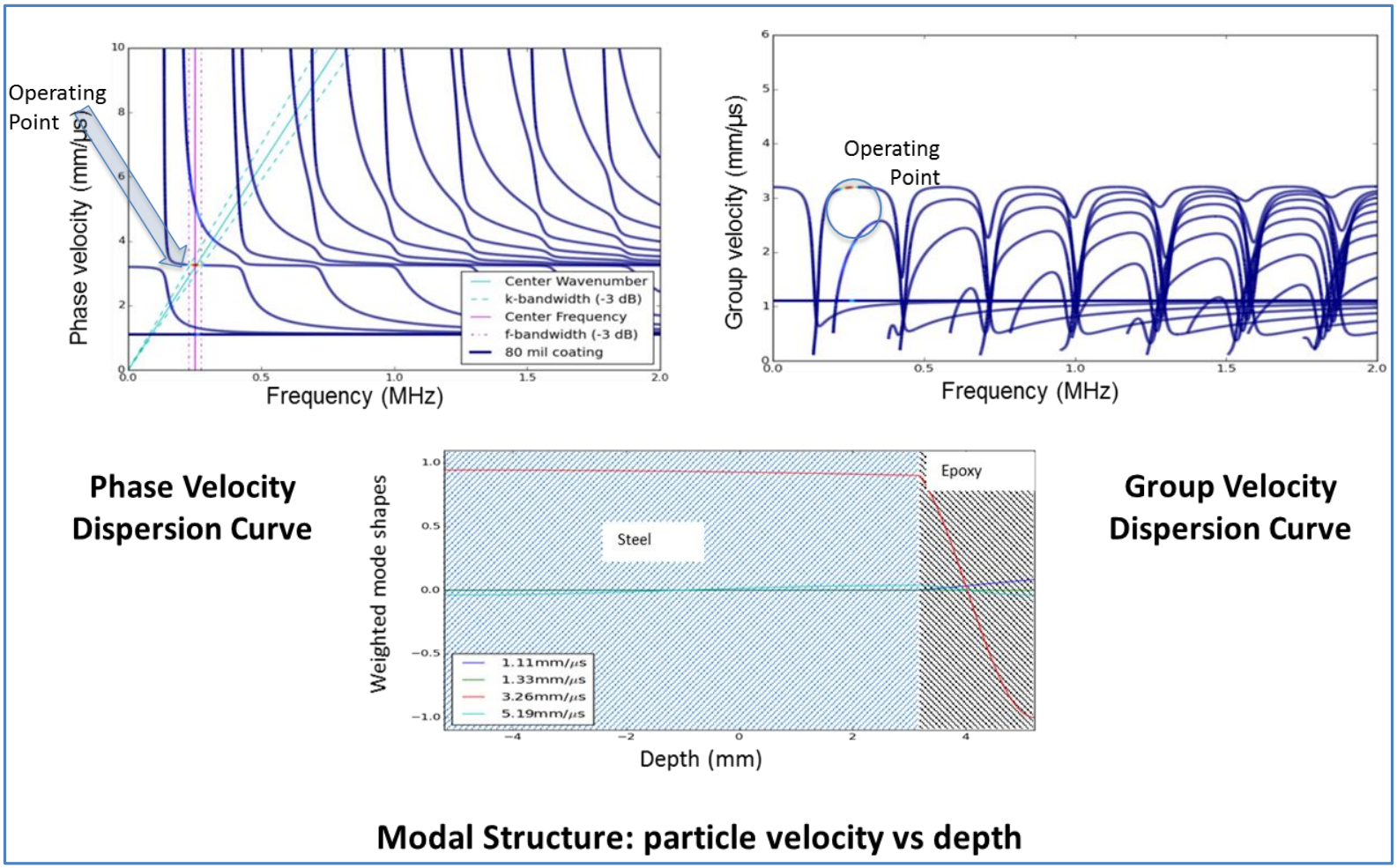

Figure 5. EDTS Sample Output for a Coated Plate with the Operating Point Identified

Transducer Coil Modeling, Fabrication and Test

An EMAT transducer utilizes a coil to generate or sense the dynamic portion of the magneto-acoustic fields while the magnet provides a fixed magnetic field bias. A necessary component of the sensor design is to determine the optimum transmit and receive coil geometry. In addition, because comparative sensitivity studies between the Lorentz and magnetostriction approaches do not exist, both types of transducers were included in this evaluation. The 0.5 inch operating point wavelength was chosen because commercially available coils optimized for the Lorentz approach could be purchased.

Both of the signal levels from two different wave modes, SH0 and SH1, and the noise levels were recorded for over 60 different transmit/receive combinations.

The sensor design section and the further work on the operating point described the drive frequencies and operation wavelength (or pitch), but what had not been determined was the number of turns in the transmitting and receiver coils. There are many subtle differences, such as trace spacing, trace width, and loops versus meander coils that could be evaluated. The lower inductance and resistance associated with a fewer number of turns will better match the lower voltage, but high current capability of battery powered devices. Higher magnetic fields at the surface can be obtained with more turns in the coil with less current, but requires higher voltages with some form of a transformer and electronics to convert the lower battery voltages to the necessary high voltage. The receiver coil optimization must be done in concert with the preamplifier.

Various combinations of impedance transformation methods are available and were evaluated, including transformers, L matching, and resonance. Fundamentally since one is dealing with an inductive/resistive sensor, the interaction between the sensor and front end capacitance/resistance define the design constraints. Ultimately it is about signal-to-noise ratio and the primary noise contributors are: externally coupled noise, the thermal noise generated by the coil, and the pre-amplifier noise. Theoretically the receiver could be a nominal number of turns with a low resistance and then through the use of a transformer, the signal will be stepped up to increase the voltage/impedance as, theoretically, the noise steps up in the same proportion. Again the limiting factor is the input capacitance of the preamp. The general approach is to maximize the wave coupling at the sensor to provide as much signal as possible, keeping within the constraint of the input impedance of the pre-amplifier, thus minimizing the effect of external noise pickup.

The tests described in this section are two-fold; to determine if there is some fundamental difference in transduction efficiency between Lorentz and magnetostriction as one researcher has indicated (but conflicts with others), obtain a general idea of the overall signal levels with a variety of coil combinations.

Table 2 provides a list of coils which were initially tested, and Table 3 tabulates the results. There were others evaluated but these provide a relevant cross-section. The meander coils are all configured as magnetostriction. The *Number of ½ Cycles* column indicates the number of meanders in the case of magnetostriction and the number of magnets along the direction of

propagation for the Lorentz. For a 0.5 inch pitch, the half cycle spacing along the direction of propagation is 0.25 inches.

The *Turns* column is the number of coil windings per half cycle, essentially the number of wires next to the surface available for inductive coupling. The *Weighted Turns* column is the product of the number of half cycles, fill factor and turns for a given coil. The *Weighted Turns* therefore provides an index which can be used to evaluate the dependence of coil performance on the number of turns. The *Inductance* column is the inductance of the coil (at 250 kHz) mounted on the steel sample using a vector network analyzer. It also produces the resistance at that frequency that was then used for circuit modeling purposes. Both the coil resistance and induction change as a function of frequency due to skin depth effects in both the steel and the windings.

Table 2. Subset of Coil Combination Tested

Coil #	Coil Description (all have a 0.5" pitch to match one of the operating points)	Number ½ Cycles	Fill Factor	Turns	Weighted Turns	Inductance over Steel @ 250kHz in µH
1	Lorentz with transmit coil on	5	0.5	72	180	10.8
2	Lorentz with 1/2 receiver coil	5	0.5	48	120	1.7
2a	Lorentz with full receiver coil	5	0.5	96	240	17.8
3	Multi strand meander coil (5 loop strands, series connected, for each 1/2 cycle). Magnetostriction	8	1	5	40	2.2
4	Series meander (4 Layer/loops overlaid)	8	1	4	32	0.9
5	Single layer meander	8	1	1	8	0.1
6	Parallel meander (4 Layers/loops overlaid)	8	1	1	8	0.062
18	Multi-strand meander, 2 layer	8	1	12	96	21

Each row in Table 3 represents a particular test combination. The *Inductance Product* is the product of the individual measured inductances. The *Tx and Rx Coil Turns Count* are the weighted turns count for each coil taken from Table 2. The *Combined Turns Count* is the product of the transmit and receive coil turns count. The *Signal pk-pk* columns are the peak to peak output voltages from the lab setup for each of the two frequencies, SH0 and SH1. The *Relative Sens/turn* columns are the peak to peak voltages divided by the combined turns count. The results are grouped by color by the transmit coil, with the highlighted color in each group showing the results when a Lorentz based receiver was used.

The Lorentz Coils 1, 2 and 2a use the same Lorentz magnet array with various coils.

Table 3. Coil Combination Testing Results, Grouped by Transmit Coil Type

Test #	TX Coil Type	RX Coil Type	Inductance Product uH^2	Tx Coil Turns Count	Rx Coil Turns Count	Combined Turns Count	Signal pk-pk 252kHz	Relative Sens/turn microvolts @ 252 kHz	Signal pk-pk 351kHz	Relative Sens/turn microvolts @ 351 kHz
1	1	3	23.76	180	40	7200	0.328	46	0.462	64
2	1	4	9.72	180	32	5760	0.252	44	0.354	61
3	1	5	1.08	180	8	1440	0.081	56	0.101	70
4	1	6	0.67	180	8	1440	0.077	53	0.1	69
5	**1**	**2a**	**192.24**	**180**	**240**	**43200**	**8.28**	**192**	**11.51**	**266**
6	1	18	86.40	180	40	7200	2.93	407	4.31	599
7	2a	3	39.16	240	40	9600	0.492	51	0.696	73
8	**3**	**1**	**23.76**	**40**	**180**	**7200**	**1.8**	**250**	**2.6**	**361**
9	**3**	**2**	**3.74**	**40**	**120**	**4800**	**0.408**	**85**	**0.502**	**105**
10	**3**	**2a**	**39.16**	**40**	**240**	**9600**	**2.63**	**274**	**4.2**	**438**
11	3	3	4.84	40	40	1600	0.125	78	0.145	91
12	3	4	1.98	40	32	1280	0.093	73	0.101	79
13	3	5	0.22	40	8	320	0.03	94	0.035	109
14	3	6	0.136	40	8	320	0.021	66	0.025	78
15	**4**	**2**	**1.53**	**32**	**120**	**3840**	**0.49**	**128**	**0.67**	**174**
16	**4**	**2a**	**16.02**	**32**	**240**	**7680**	**2.11**	**275**	**3.3**	**430**
17	4	3	1.98	32	40	1280	0.128	100	0.137	107
18	4	4	0.81	32	32	1024	0.119	116	0.145	142
19	4	5	0.09	32	8	256	0.038	148	0.046	180
20	4	6	0.056	32	8	256	0.032	125	0.044	172
21	**5**	**2**	**0.17**	**8**	**120**	**960**	**0.16**	**167**	**0.178**	**185**
22	5	3	0.22	8	40	320	0.038	119	0.039	122
23	5	4	0.09	8	32	256	0.028	109	0.03	117
24	5	5	0.01	8	8	64	---	---	---	---
25	5	6	0.0062	8	8	64	---	---	---	---
26	**6**	**2**	**0.105**	**8**	**120**	**960**	**0.13**	**135**	**0.157**	**164**
27	6	3	0.1364	8	40	320	0.032	100	0.035	109
28	6	4	0.0558	8	32	256	0.017	66	0.021	82
29	6	5	0.0062	8	8	64	---	---	---	---
30	6	6	0.0038	8	8	64	---	---	---	---
31	**18**	**2a**	**142.40**	**40**	**240**	**9600**	**6.81**	**709**	**10.43**	**1086**

It is important to point out that in all coil combinations, the current in the transmitting coil was kept constant at 26 amps peak to peak and the receiver gain was kept constant. High inductance transmit coils require a higher voltage drive. Also, with the higher inductance receive coils, testing was performed to assure that any peaking due to the resonance between the receiver sense coil, cable capacitance, and pre-amplifier input capacitance did not significantly impact the results. This is why many of the coils tested are not included in Table 3. There was 1 – 2 dB peaking for the higher inductance coils that slightly influenced relative amplitudes between the 250 and 350 kHz test frequencies. At lower inductances the resonance was well above frequencies of interest so it is not a factor.

Analytical Finite Element Modeling and Operating Point Selection

Overview

Guided waves offer an infinite number of operating points, so relying purely on finite element methods alone when testing these points is a never-ending task. Therefore, the analytical finite element modeling approach was adapted, which is essentially the use of analytical modeling of guided waves, selecting the operating points and then testing the operating points through the use of a finite element model(s). The EMAT tool design software (ETDS) described earlier forms the analytical part of this approach. While the ETDS was being developed, finite element scripts were also being developed and validated against results available in literature. Once the ETDS software was ready, the task of selecting the operating points was carried out, and subsequently the operating points were simulated and tested using the finite element method. It may be noted that neither the identification of operating points nor their subsequent finite element testing were trivial tasks. The effort and resources expended to perform these tasks successfully are outlined below.

Computing system configuration

A high-end computing system with 64 processors and 192 GB RAM with hot-swapping features was procured by QUEST just before the start of the project. Significant time was spent on configuring the Linux-based operating system software, finite element software and supporting software that was necessary for organizing the work and remote access. Remote access was required, because unlike a desktop computer, the workstation was very noisy which necessitated its seclusion from general office space. At the same time, the finite element programs which run for several days needed to be monitored. The system was configured to run as a torque Portable Batch System (PBS) and Secure Shell (SSH) server so that finite element programs could be executed not only without physical access but also without continuous network access. The PBS scripts were written in a fashion that allowed tracking of the numerous computational tasks.

Guided wave analysis and ETDS

Programs using Python language were written for generating dispersion curves and extracting other related output such as group velocity and wave structure. It may be noted that tracing dispersion curves for coated plates requires significant personal attention and iterations because of the complex shapes of these curves, despite the use of automated root searching algorithms. The ETDS, which was written using the PYQT extension, is useful only after the required dispersion curves are generated.

Operating point selection and FEM

Hundreds of dispersion curves were generated and compared in order to select the optimal operating points. The operating point selection involved the following criteria and/or constraints:

1. The number of necessary operating points must be minimized
2. The selected operating points must provide good mode purity
3. The operating points must be insensitive to small variations in pipe wall and coating thicknesses
4. The operating points must be sensitive to flaws

5. The operating points must not be prone to excessive viscous loss
6. The operating points should not be dispersive (preferably)

Figure 6 shows a comparison of dispersion curves for an 8.4 mm thick steel plate and about 50 different coating thicknesses. At first sight it appears that the operating points which satisfy the first two criteria listed above occur at the low frequency end. However, hardware capabilities and small pipe diameters meant that only frequencies above 100 kHz must be used. This ruled out use of a low frequency operating point for most of the coating thicknesses. Subsequently, several man-weeks were spent comparing and cycling through the dispersion curves and related output using the ETDS so that all the requirements listed above were met to a reasonable extent. As will be seen later, three sets of operating points were chosen, each for a particular range of coating thickness. These choices were further filtered using finite element analysis. The rejected choice meant that dispersion curve analysis needed to be repeated to find a new operating point that will cover the corresponding range of coating thickness. Equivalent effort was also required during the process of experimental sample design, given the constraints of coating thickness and functioning EMATs available in-house. Finite element scripts using the Python language extensions for these packages were written for bulk wave propagation on prior projects and were adapted to the current project. However, modeling guided waves required significant debugging effort and cross-checking for convergence, which was performed in parallel to the tasks comprising the development of the ETDS and the operating point selection. It may be noted that the mode purity criterion was relaxed for changing plate thickness as such modes do not decrease the flaw sensitivity and can in most cases be filtered in the frequency domain.

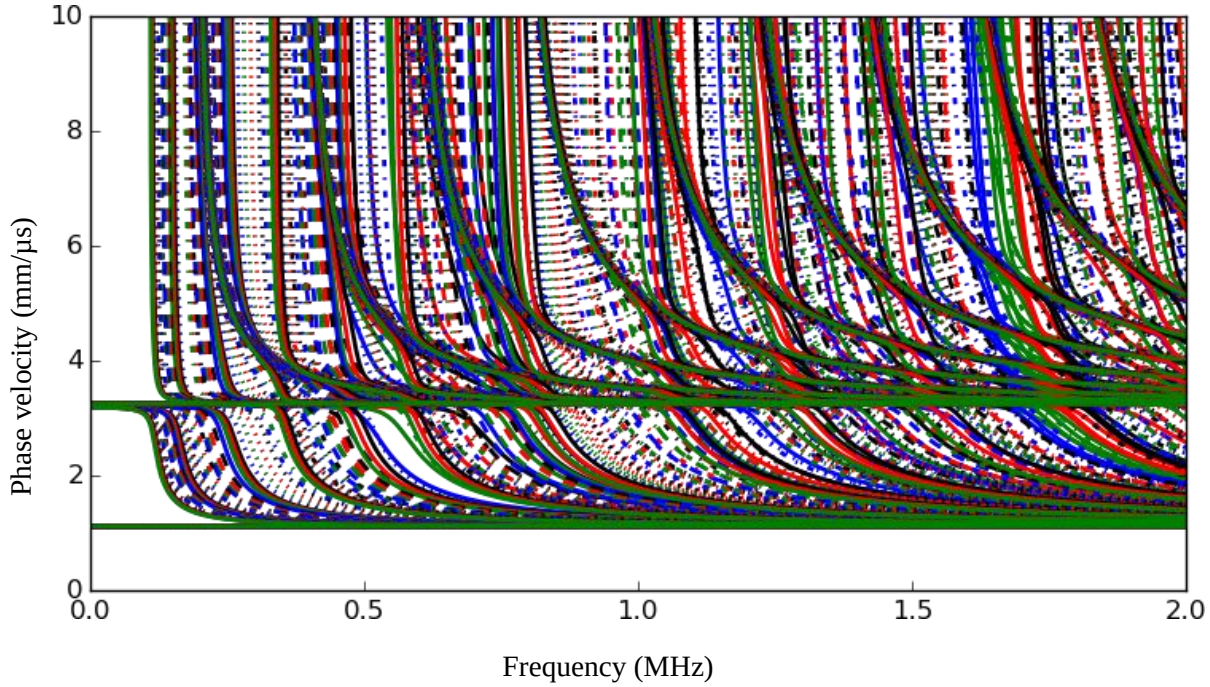

Figure 6. Comparison of Dispersion Curves for Different Coating Thicknesses Starting from 2 mils to 100 mils in Steps of 2

Detailed description of FEM

Programs were written for performing parametric finite element analyses using the Python language extension of the open source GETFEM++ finite element library. The geometrical aspects were modeled using the open source Pyformex library. The programs were designed to perform parametric analyses for several combinations of parameters such as crack depths, crack locations and coating thickness as shown schematically in Figure 7. In addition, Python scripts were written to extract sensitivity results from the simulation data. The primary purpose of the analytical finite element modeling was to verify flaw depth results from literature and also to verify if the selected operating points derived from the analytical results or ETDS offered similar sensitivity.

The parametric analyses were performed using a 2D model that solves for a Helmholtz equation of a single variable:

$$\nabla^2 u_z = \frac{1}{c_2^2}\frac{\partial^2 u_z}{\partial t^2} \qquad 1$$

where, u_z is the particle displacement along a direction that is orthogonal to the cross-section of the plate. The 3D model solves a more general elastodynamic problem and was used initially to confirm if the guided wave signals generated by the 2D model is a valid simplification for the analyses. The 3D model was not used for parametric analyses because of very large computational costs.

Using the EMAT tool design software, the operating points relative to coating thicknesses were first identified. The candidate operating points originally selected using the EMAT tool design software are shown in Table 4. Of these, the first operating point was dropped because the Advanced Finite Element Method (AFEM) analyses indicated unacceptably low sensitivities as shown in Figure 8 a-b. The modified operating points are shown in Table 5. Relatively higher flaw depth sensitivity was observed for bare plates simulations performed at the 0.25 MHz operating point. Hence, analyses were performed for the same operating point and coating thickness combination. In addition, analyses were performed to confirm if the location of the flaw – whether on the bare side or on the coated side – affected the flaw sensitivity. The corresponding results for both bare and coated plates are shown in Figures 9-12. Clearly, the sensitivity is affected by the presence of coating. For both cases the location of the flaw also impacts the sensitivity.

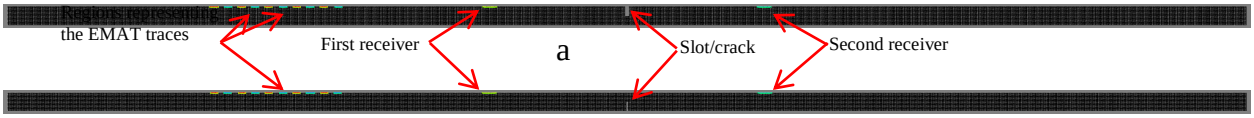

b

Figure 7. Two-dimensional Finite Element Model Details

Table 4. Preliminary Operating Points

Design No.	Coating thickness Range(mm)		EMAT		Electrical Pulse	
		Wavelength (mm)	Trace Width(mm)	No. of Traces	Frequency (MHz)	No. of Cycles
1	0-1	25.4	6.35	4	0.125	>1
2	1-1.8 mm	8	2	14	0.4	>4
3	1.8-2.8 mm	12.71	3.17	8	0.25	>5

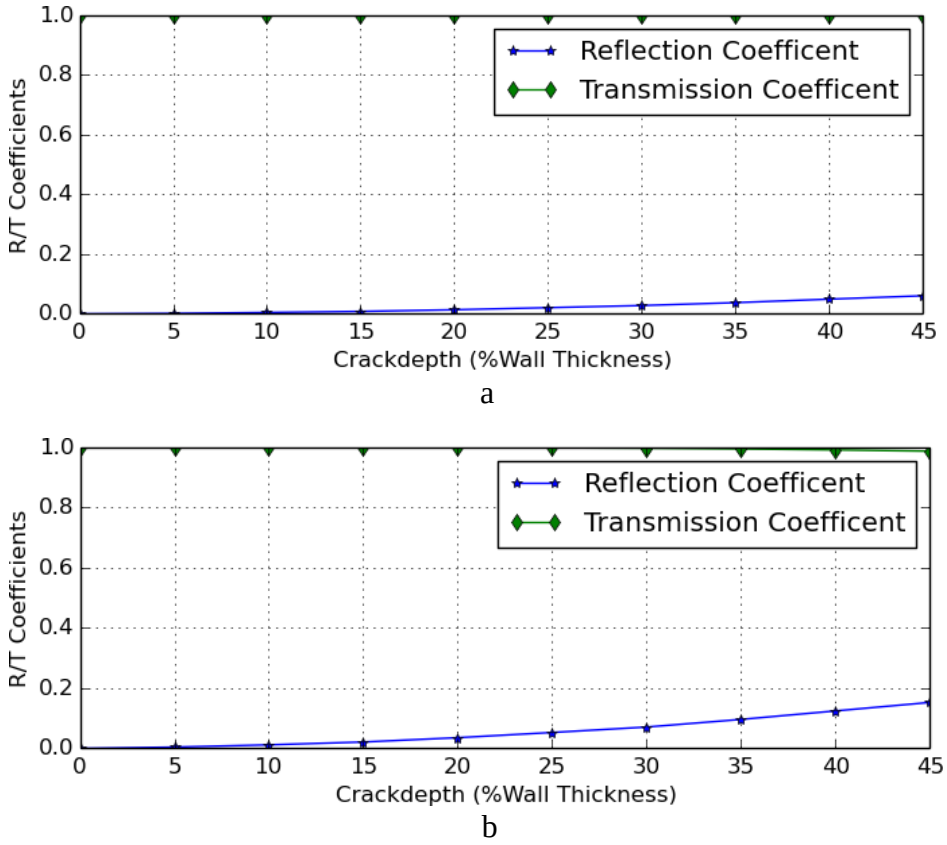

Figure 8. RC/TC vs Crack Depth for Operating Frequencies

(a) 0.125 MHz and (b) 0.4 MHz; crack width was held constant at 0.52 mm in the presence of a 0.25 mm coating on a 8.4 mm plate

Table 5. Modified Operating Points vs Coating Thickness

Coil Design Wavelength (mm)	Operating Frequency (MHz)	Group Velocity Range (kmps)	coating thickness range (mm)
12.71	0.25	3.15-3.25	0-0.5
			1.8-2.54
8	0.4	3.14-3.17	1-1.8
			2.54-2.8
	0.72 (higher order mode, SH3)	~1.8	0.5-1.0

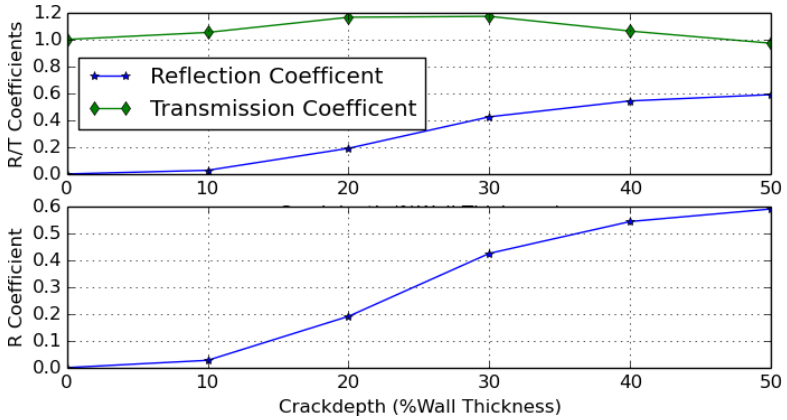

Figure 9. Reflection and Transmission Coefficients for Bare Plate with Crack on Bottom (and EMAT on the top side)

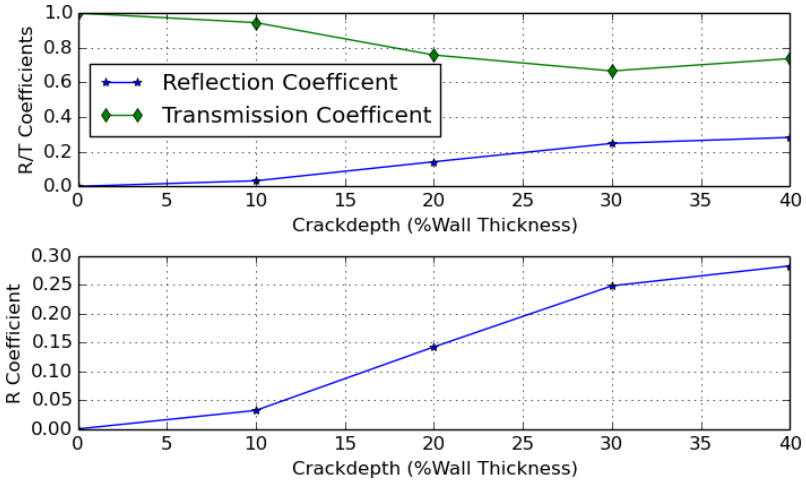

Figure 10. Reflection and Transmission Coefficients for Bare Plate with Crack on the Top (and EMAT on the top side)

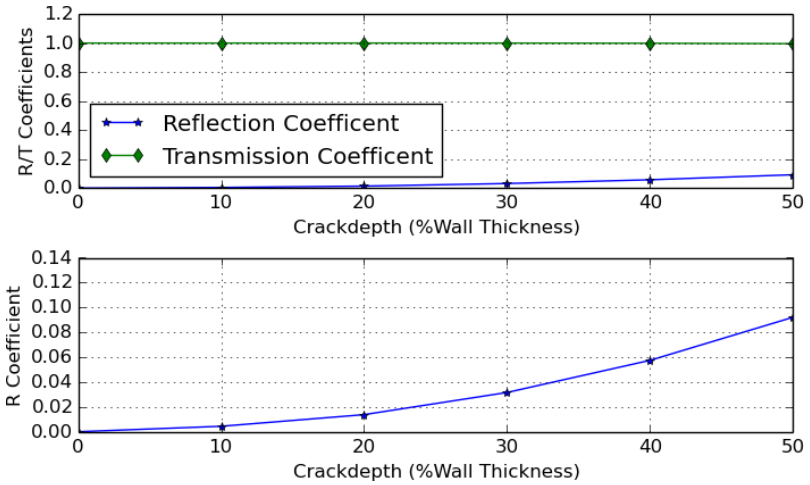

Figure 11. Reflection and Transmission Coefficients for Coated Plate with Crack on the Bottom

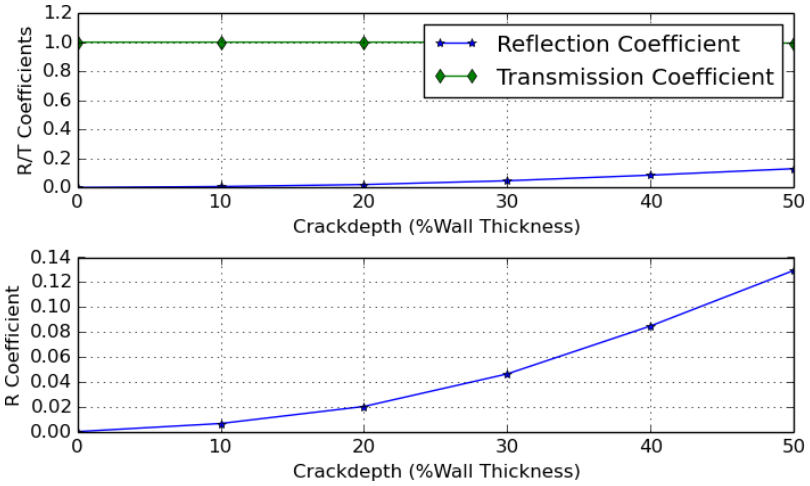

Figure 12. Reflection and Transmission Coefficients when the crack growth is from the EMAT side of the steel plate

Magnet Geometry and Electromagnetic Modeling

Yoke Geometry

When developing a Lorentz-based EMAT sensor, the relationship between magnet strength and signal level is straightforward: the designer wants the bias magnetic field to be as strong as the other system constraints will permit. However with a magnetostrictive sensor, the relationship is much more complex and depends on the magnetostrictive coefficients of a particular material. For steel, there will be a particular magnetic field strength at which the signal-to-noise ratio is maximum. Researchers have used the magnetostriction curve shown in Figure 13 to derive transduction coefficients. Two different coefficients are derived based on the orientation of the induced current relative to the biasing magnetic field; one is derived from the slope of the magnetostriction curve and the other is based on the absolute field values. Assumptions are made regarding the relative amplitudes of the dynamic versus static field levels.

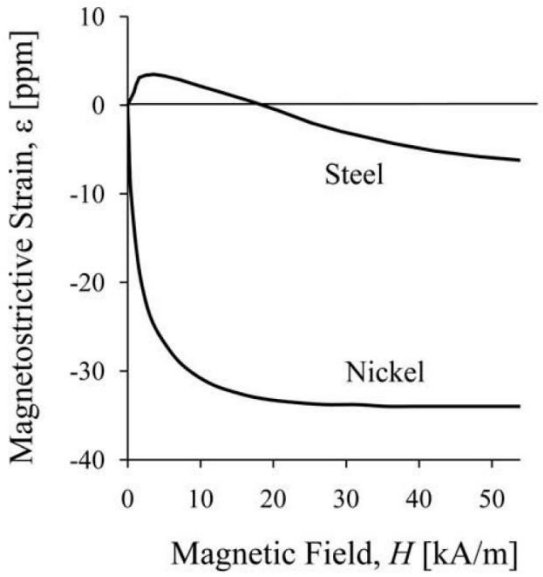

Figure 13. Variation in Magnetostrictive Strain with Bias Field (Ribichini 2011)

To determine the desired bias field strength, the literature was surveyed to determine what was used by other researchers in their experimental setups. Excluding Lorentz-based experiments, very few researchers provided this information in a usable form. There was special interest in identifying the bias field strengths at which magnetostriction or Signal/Noise (S/N) would be at their peak. These are summarized in Table 6. Note that numbers are approximate as in many cases they were obtained from a plot.

Table 6. Reported Magnetic Bias at Peak Magnetostriction

Source	Reported Field Strength at peak Magnetostriction or S/N	How Measured	Notes
Aron 2005	4000 G (note that this is not a peak; it is what was achieved with permanent magnets)	Measured in air gap under pole of bias magnet	Would imply H-field values of ~370 A/m (according to Maxwell)
Thompson 1979	300 Oe	Not specified	Would imply H-field values of 24,000 A/m
Igarashi 1998	800 A/m	Measured in air and assumed to be the same in material surface	
Ribichini 2011	3800 A/m	Measured in air and assumed to be the same in material surface	Very thin steel plate (0.5mm). Maxwell predicts actual H ~= 15,000 A/m

As can be seen from the figures in Table 6, the reported field strengths span a large range. Thompson, Igarashi, and Ribichini achieved these high field strengths by testing with very short, thin plates placed between two magnets or electromagnets (Figure 14).

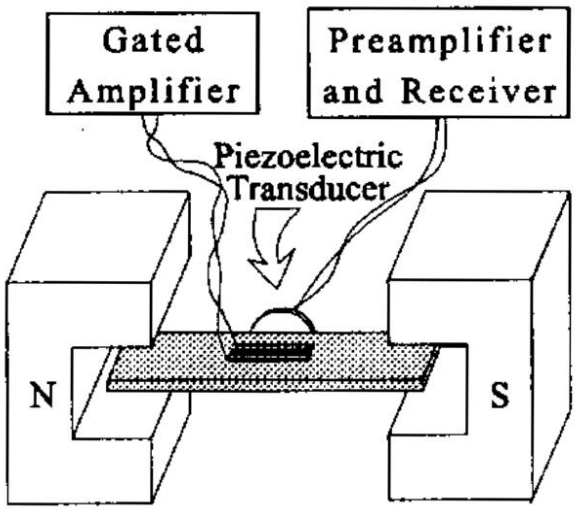

Figure 14. Typical Lab Setup for Measuring Signal Strength vs. Induced Field (Igarashi 1997)

The geometry of this arrangement is such that the magnetic field between the two magnets is fairly uniform without leakage of the fields back on each other. Also in some cases electromagnets were used to generate arbitrarily large fields, even to the point of saturating the steel.

Fields of the highest magnitude shown in Table 6 are not attainable in a battery-powered, fieldable tool. This simply means that a fieldable tool will be operating below the peak. However as shown by Aron, good results are still possible.

The maximum allowable envelope for the magnetic yoke is determined by the pipe geometry (i.e., the ability to go around a 1.5D bend). This yields an approximate volume of 2.5" wide by 6" long by 1" high. Reducing the height allows the width to be increased somewhat.

Working within this volume, Maxwell 3D was used to arrive at a magnet/yoke geometry that would yield H field strengths within the pipe that are comparable to those used by Aron, but would still allow for some increase in field strength if this should prove necessary (Figure 15). The assembly was widened somewhat to achieve good uniformity of the bias field in the vicinity of the coil, and to allow the use of 3" magnets which are available off the shelf. The final configuration makes use of Grade N42 magnets that are 3" wide x 1/4" tall x 1/2" long. They are connected by a steel back-bar that is 3" wide, 1/4" tall, and 6" long.

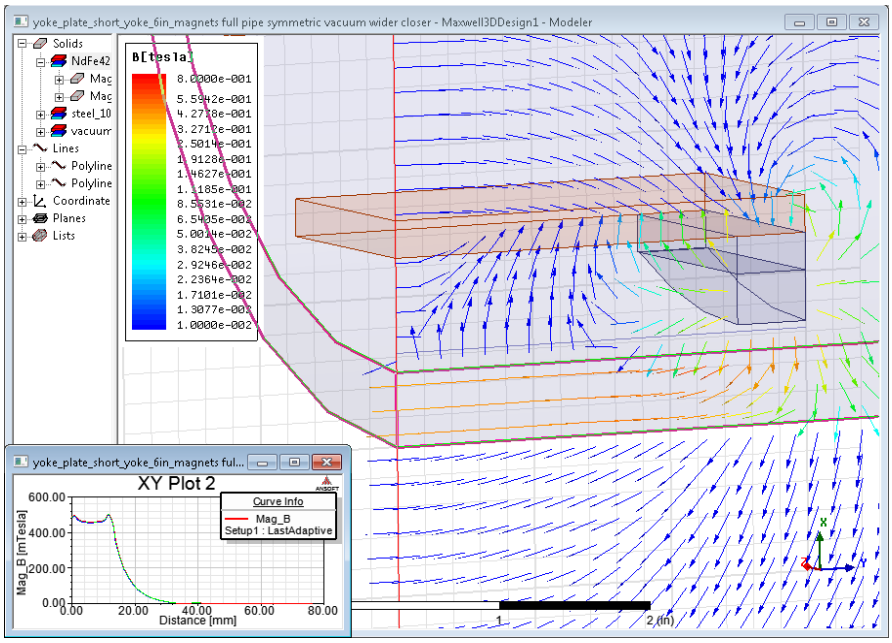

Figure 15. Yoke Cross-Section with B-Field

Within a circular pipe, the air gap would vary considerably under a flat magnet. Therefore it was decided to utilize hemispherical steel or iron pole pieces under the magnets to achieve a uniform air gap (Figure 16). A planned air gap of 0.2" to 0.25" will result in H-fields of the desired intensity.

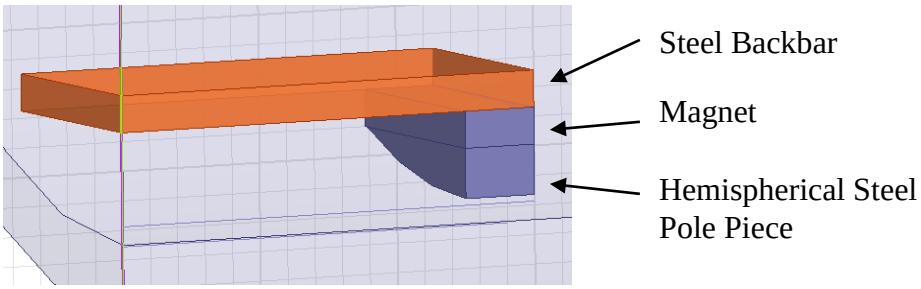

Figure 16. Yoke Cross Section

This configuration yields H field strengths in a half-inch pipe wall of approximately 550 A/m. By increasing the size of the magnets, thickening the backbar, shortening the backbar, and/or reducing the liftoff, the amplitude of the field strength can be increased. There are also higher grade Neodymium magnets available in some sizes. Maxwell indicates that the maximum achievable field strength is approximately 800 A/m. The disadvantage of making these changes would include increased weight and increased magnetic attraction to the pipe wall, making the tool more difficult to handle. Liftoff can be adjusted by replacing the glides. Ultimately replaceable transducer heads will allow optimal magnetic biasing for a given wall thickness, if necessary.

Figure 17 shows a 4-transducer layout inside a pipe. It was important to determine if adjacent yokes interacted in any way as well as get an estimate of the magnetic force between the magnets and the pipe wall. The magnetostriction transducers are 2.5" wide by 6" long by 1/2" high, not including the arc-shaped pole pieces. The image on the left shows a Maxwell 3D simulation of the induced H field in the inner surface of the pipe. The arrows show the circulation of magnetic flux in the pipe. The field is very uniform between the poles. With the magnet, yoke, and liftoff given, the attractive force between pipe wall and a transducer is approximately 18 lbs. The attraction of the transducers to the pipe wall is a factor in the ability of technicians to handle the device safely and without specialized equipment.

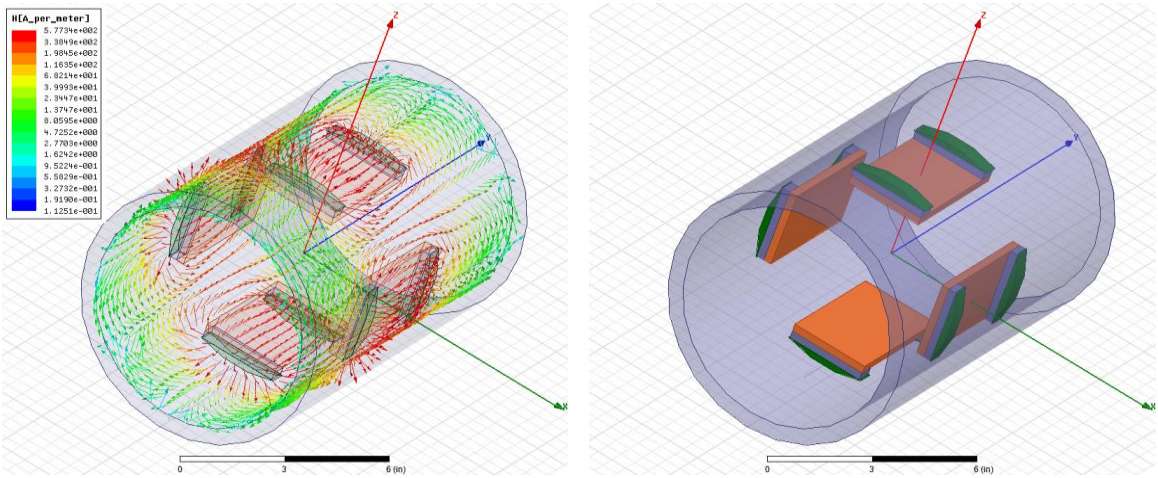

Figure 17. Pipe with 4 Yokes, Showing Induced H-Field

Analysis of the Maxwell 3D data determined that the interaction or crosstalk between the yokes is limited, and it is anticipated that these types of variations will be dealt with by normalization. Because a transmitted signal travels in two directions, 180 degrees apart, it will be intercepted by two receivers. A signal affected by a defect can therefore be normalized by its 180 degree counterpart which has not been affected by the defect (Aron 2005). This allows for real-time compensation for changes in material properties, wall thickness, etc.

Wall Thickness

Maxwell 3D simulations were also used to evaluate the effect of wall thickness on tool signals. Changes in wall thickness have minimal impact on the high frequency pulse train in the coil. Because the skin depth is so short in steel at high frequency, coil-generated signals are confined to a very narrow region near the inner wall of the pipe. The bias field produced by the yoke is a different matter. Figure 18 illustrates the dependence of bias field strength vs. pipe wall thickness. This is a well-known problem for magnetic flux leakage tools that requires the pipe wall to be near saturation. Fortunately for this application it does not require saturation.

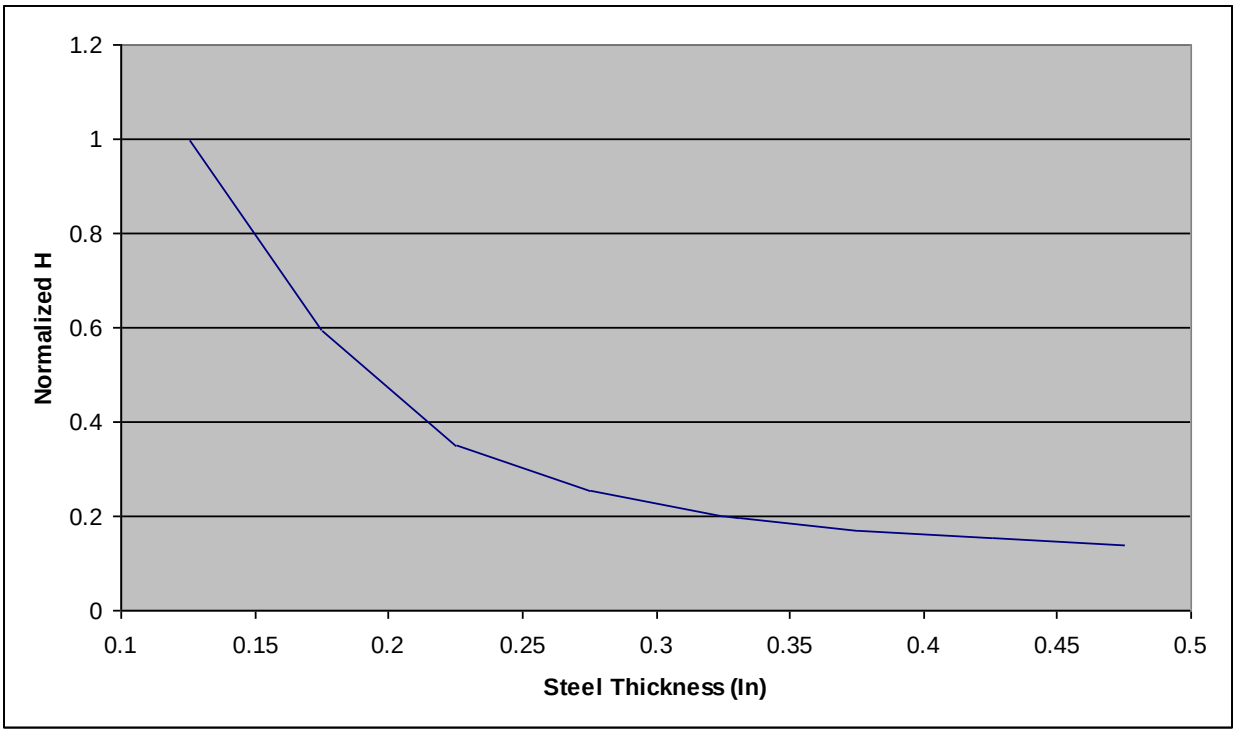

Figure 18. Induced H vs. Steel Thickness

The plot shows a couple of general trends:

- the thinner the pipe wall, the greater the induced H
- The thinner the pipe wall, the more induced H varies with a given change in thickness

According to this data, at a thickness of 0.5", the change in induced H varies almost directly proportionally with a change in thickness. In other words, a change in wall thickness of 0.01" (or 2%) will result in a change in signal level of 2%. One can use a normalization procedure to deal with these types of changes. The configuration was sized to induce H field levels comparable to Aron's at intermediate pipe wall thicknesses. For pipes of the highest thickness, a yoke was installed to optimize for maximum bias field levels. The wall thickness for a given gas pipeline inspection does not change during a given inspection run.

Coil Geometry

The meander coil is positioned under the center of the yoke for the magnetostriction sensor. Unlike the yoke, the coil must be as close as possible to the pipe wall for maximum signal-to-noise ratio. The liftoff cannot be zero, because a wear surface is necessary to protect the coil. Maxwell 3D was used to evaluate the effect of different liftoffs on induced H (Figure 19). Note the roughly exponential relationship. This is consistent with other researchers, however Maxwell provides the absolute relationship.

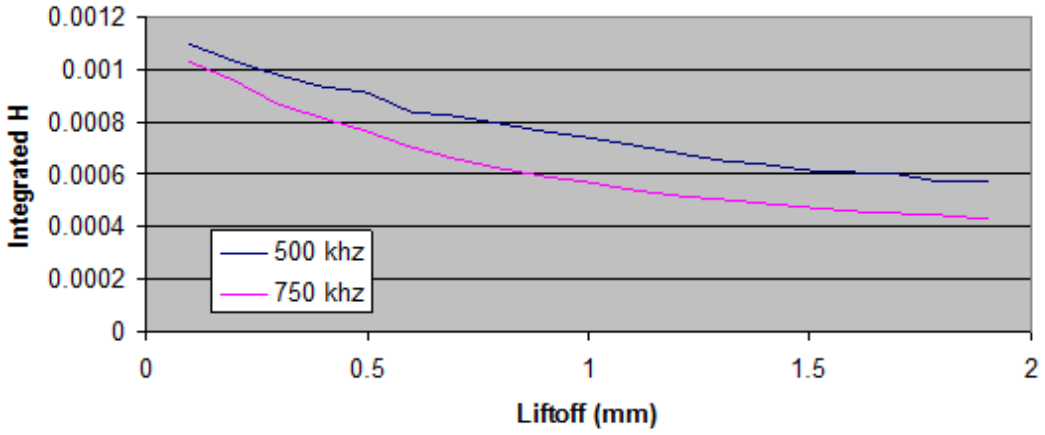

Figure 19. Liftoff vs. Induced H

As the plot demonstrates, the signal degrades with both increasing frequency and liftoff. This degradation is partially offset by the fact that at higher wavenumbers more meander coil turns will fit within a given area. It is important to note that because of the exponential relationship and because the coil is nominally operated at a lift-off of 0.5 mm, the change in sensitivity with changes in lift off is reduced.

The nominal yoke configuration allows for an overall sensor (coil) footprint of 2" x 2". This allows a wave front that is about 2" wide, which provides adequate axial defect resolution while at the same time allowing room for several cycles to narrow the wavenumber bandwidth and minimize the amplitude of the non-useful wave modes. As discussed in the guided wave design tool section, a coil with several cycles performs a spatial filtering function which improves S/N. The desired acoustic wavelength determines the trace pitch. The width of each trace is something that was investigated through review of other researchers' work and through Maxwell 3D simulations. As reported by others (Shujuan 2010) narrower trace widths are more efficient, for a given resistance. However the frequency content of the induced wave also experiences

more distortion with narrower traces as shown in Figure 20. More distortion directs some of the energy into higher wavenumbers, which influences the amplitudes of the modes induced in the pipe wall.

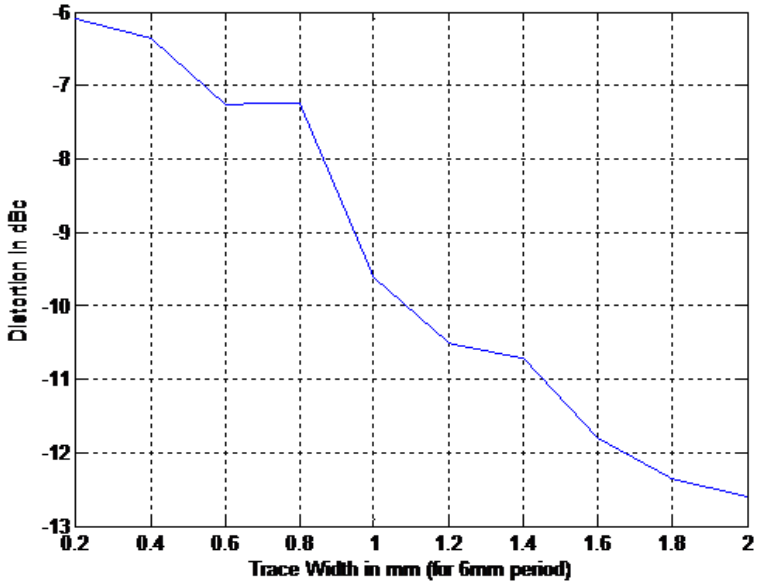

Figure 20. Harmonic Distortion (in Decibels) vs Trace Width

References

Ribichini R., Cegla F., Nagy P., and Cawley P. *Quantitative Modeling of the Transduction of Electromagnetic Acoustic Transducers Operating on Ferromagnetic Media.* IEEE Transactions on Ultrasonics, Ferroelectrics, and Frequency Control, vol. 57, no. 12, Dec. 2010, pp. 2808-2817

Hirao M., Ogi H., *EMATS for Science and Industry Non-contacting Ultrasonic Measurements,* Kluwer Academic Publishers, 2003.

Igarashi B., Alers G., and Purtscher P. *An Ultrasonic Measurement of Magnetostriction,* IEEE Ultrasonics Symposium, 1997.

Igarashi B. and Alers G. *Excitation of Bulk Shear Waves in Steel by Magnetostrictive Coupling.* National Institute of Standards and Technology, Materials Reliabillity Division, 1998 IEEE Ultrasonics Symposium, pp. 893-896.

Igarashi B., Alers G., and Purtscher P. Magnetostrictive EMAT Efficiency as a Materials Characterization Tool, Review of Progress in Nondestructive Evaluation, Vol. 17, New York: Plenum Press, 1998.

Aron J., Jia J., Vance B., Chang W., Pohler R., Gore J., Eaton S., Bowles A., and Jarman T. *Development of an EMAT In-Line Inspection System for Detection, Discrimination, and Grading of Stress Corrosion Cracking in Pipeline.* Final Report (Phase I). DOE award number DE-FC26-01NT41154, Tuboscope Pipeline Services and QinetiQ. February 2005.

Shujuan W., Penghao X., Lei K., and Guofo Z. *Research on Influence of Lorentz Force Mechanism on EMAT's Transduction Efficiency in Steel Plate.* 5th IEEE Conference on Industrial Electronics and Applications, 2010.

3. Sensor Design

This section summarizes the overall EMAT sensor design.

The primary mechanical design requirements for the small diameter EMAT sensor is that it must be incorporated into a towable pig for inspecting small diameter (8") pipe. At this time the individual EMAT sensor is the primary focus. However to ensure future integration, the sensor needs to be incorporated into the previously outlined concept of the pig design. As such, the sensor must be sized to fit within the required physical space, while providing room for the complete pig. The sensor must also provide reliable operation while inspecting the pipe. To meet this goal, the sensor design combines small size with good common practices for pig design. These include design elements that make use of wear- and impact-resistant materials combined with configurations for negotiating pipe bends, traversing openings in the pipe wall and collapsing to navigate past intrusions.

The basic pig concept uses four sensors arrayed about the pipe diameter. To ensure good sensing performance, the sensor must remain in intimate contact with the pipe wall. This goal is met by each sensor being independently suspended from the pig body. Additionally the sensors are composed of two components, a magnet assembly and a coil assembly. The SolidWorks 3D model in Figure 21 illustrates the sensor arrangement in the overall pig concept.

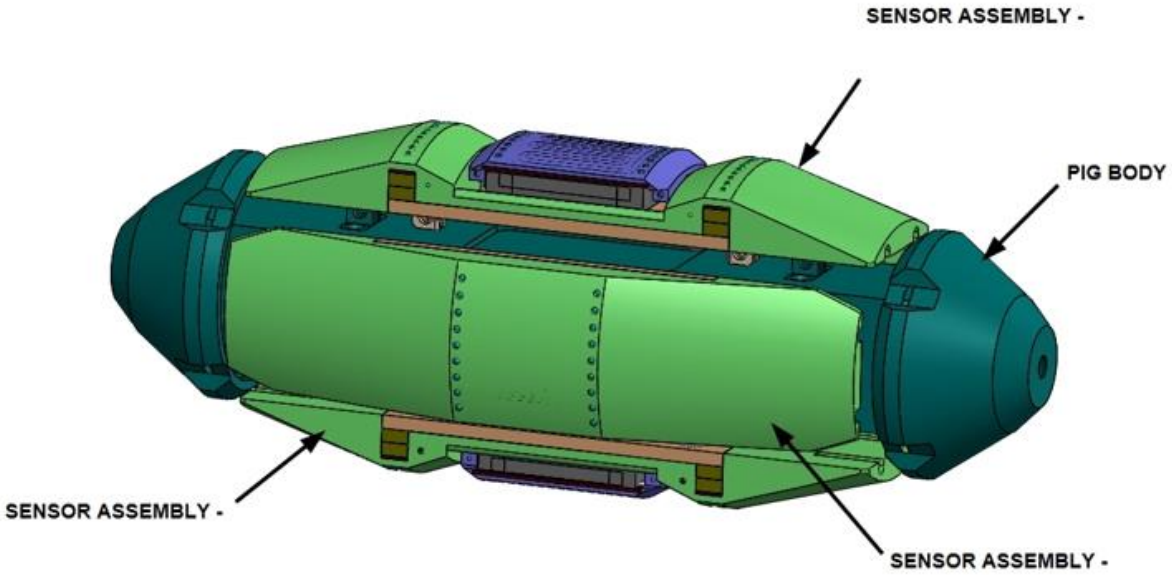

Figure 21. Sensor Assembly & Pig Concept

Sensor Mechanical Requirements

The basic mechanical design requirements for the EMAT pig were presented in the Requirements section.

Basic Design Considerations

To meet the stated requirements, the sensor design incorporates design elements in keeping with the stated values. The following outlines how the requirements are met:

- The temperature range is modest and the sensor uses materials commonly found in pig designs.
- The independent suspension of the sensors to the pig body provides space in between the sensors for product to flow past the sensors. Additionally it is anticipated that there will be space between the sensors and the pig body that will offer additional product bypass.
- The sensor does not have any sealed cavities. This allows the surrounding pressure to act hydrostatically on all of the sensor elements. Where porous materials such as foam are used, open cell types are utilized to prevent pressure collapse.
- To ensure the operating speed can be met, wear resistant materials are used at contact pressures below the pressure-velocity (PV) limits for the material.
- The sensor is designed to fit within the specified pipe size at the minimum diameter determined from the tolerance limits.
- Wall thickness tolerances are also used at the limits for determining sensor fit.
- Good pig design practice goes beyond the stated 85% collapse factor to 80%. For this design an 80% collapse factor is used.
- The sensor is configured to fit through a 1.5 OD pipe bend at the minimum pipe diameter.
- The sensor is symmetrically configured. This provides the capability to move along the pipe equally in either direction ensuring bi-directional operation.
- The sensor incorporates features to guide it over a greater than 0.125” protrusion.

In addition to the above requirements, the sensor design follows good pig design practices. This includes the capability of traversing openings in the pipe wall. Piping specifications typically call for openings being barred if they exceed 50% of the nominal pipe OD. However good pig design practice uses an opening traverse of 60% nominal pipe OD. The sensor is designed to the 60% opening.

Sizing the sensor requires determining the minimum pipe ID and the smallest bend radius it must pass through. The sizing requirements were presented in the Requirements section. These requirements remain the same for the Lorentz sensor at a 7.16” diameter design constraint.

Sensor Configuration

Figure 22 illustrates the sensor design. This consists of a magnet assembly surrounded by a coil fabricated from flexible printed circuit board material. The sensing portion of the coil is accurately positioned relative to the magnet poles and sandwiched between the magnet poles facing the pipe ID wall and the protective glide. The magnet assembly and coil are mounted in a pocket within the glide. The glides are supported by a backplate which mounts at two suspension points for connecting the sensor to a pig body when incorporated into a complete EMAT tool.

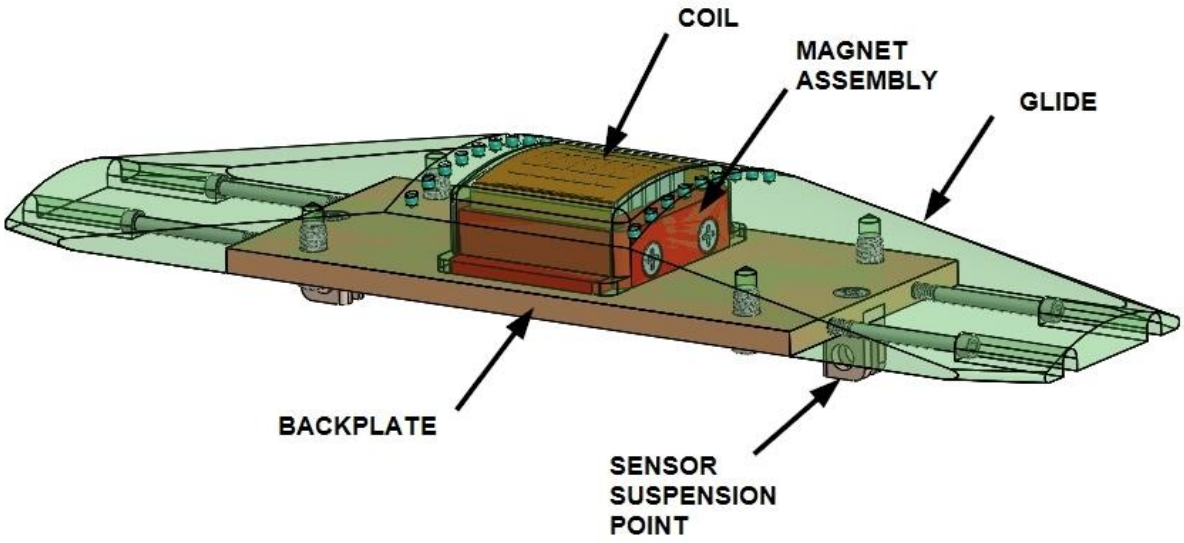

Figure 22. EMAT Sensor Design

The magnet glides are configured to fit within the design diameter stated above and negotiate the minimum bend radius. The glides are also configured to pass over a 0.125 inch (3.2 mm) weld protrusion and traverse a 60% opening at the maximum pipe ID. Figure 23 illustrates the sensors along with a possible pig body inside the minimum pipe bend at the minimum pipe diameter. Figure 24 illustrates the sensors with a pig body inside the minimum design diameter. Figure 25 illustrates the sensors at an 80% collapse diameter. Figure 26 illustrates the sensor traversing a 60% pipe opening.

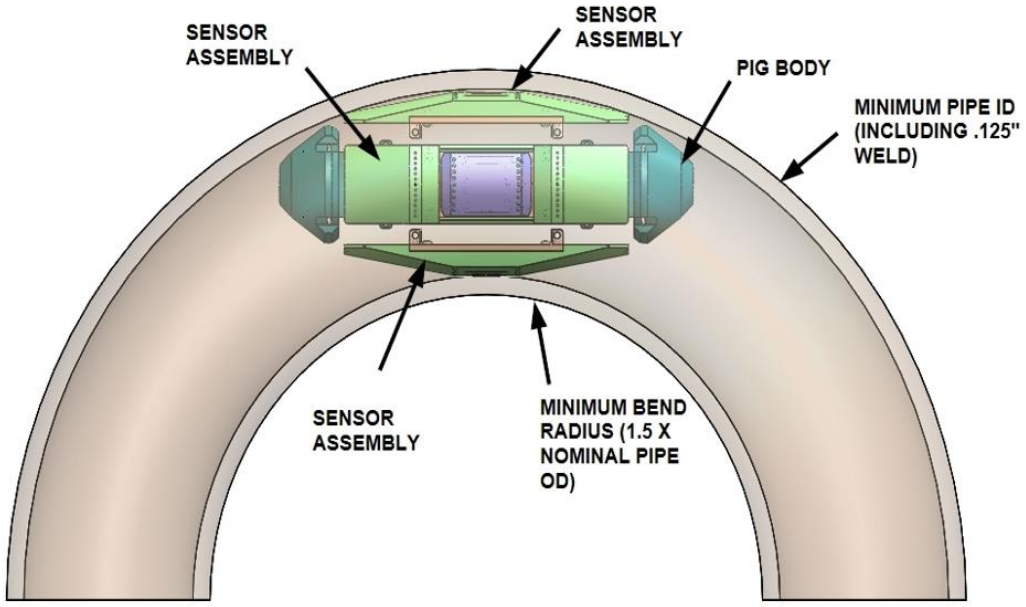

Figure 23. Sensor Inside a Minimum Pipe Bend

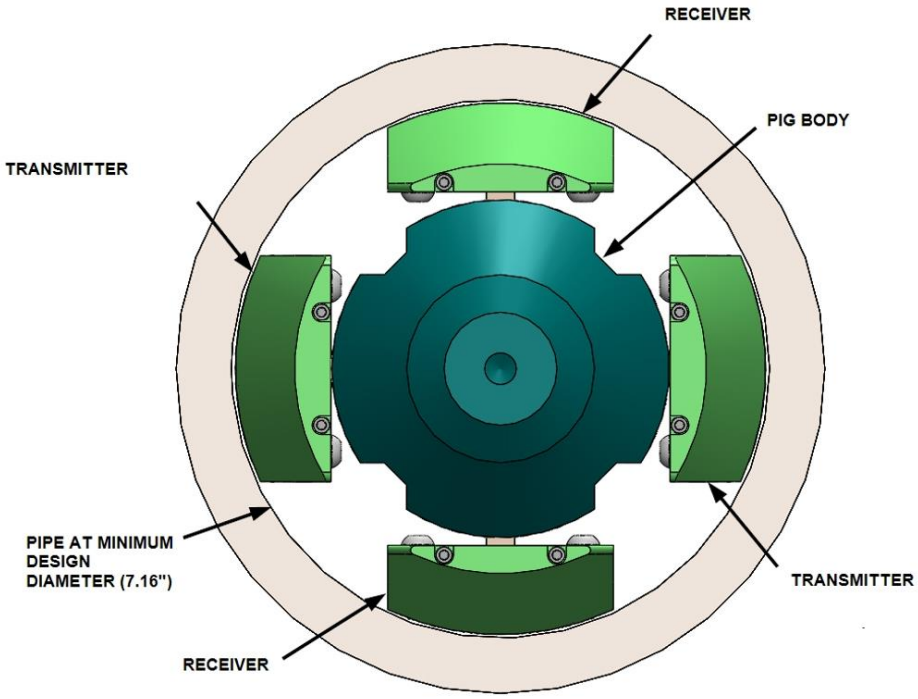

Figure 24. EMAT Sensors at Minimum Design Diameter

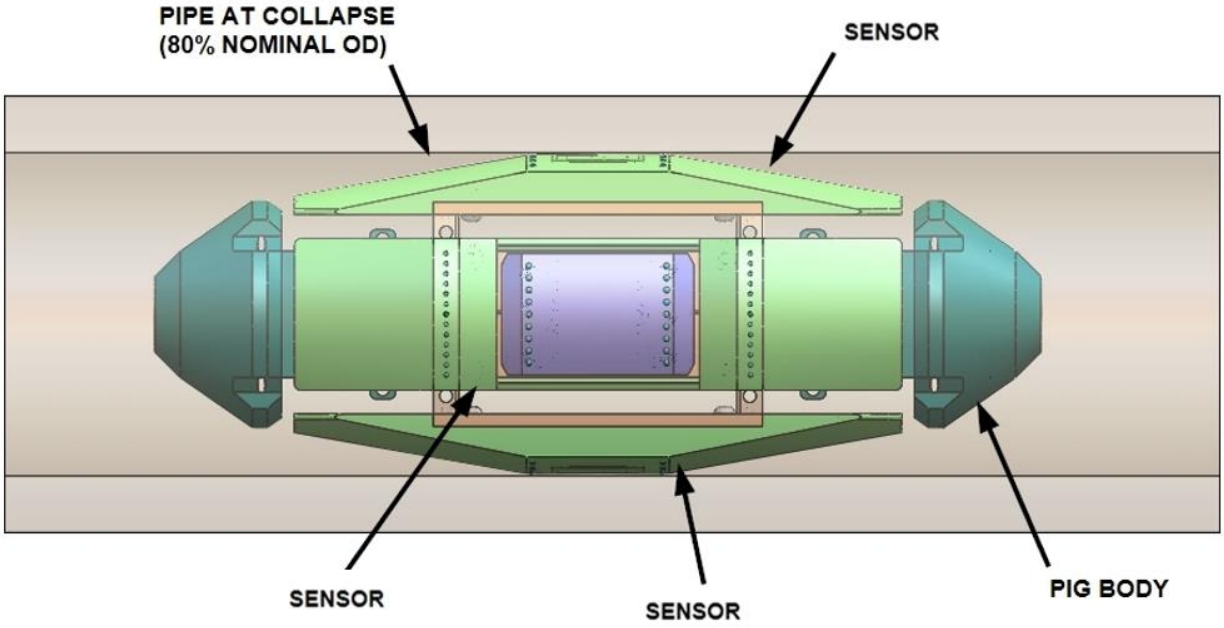

Figure 25. EMAT Sensors at 80% Collapse

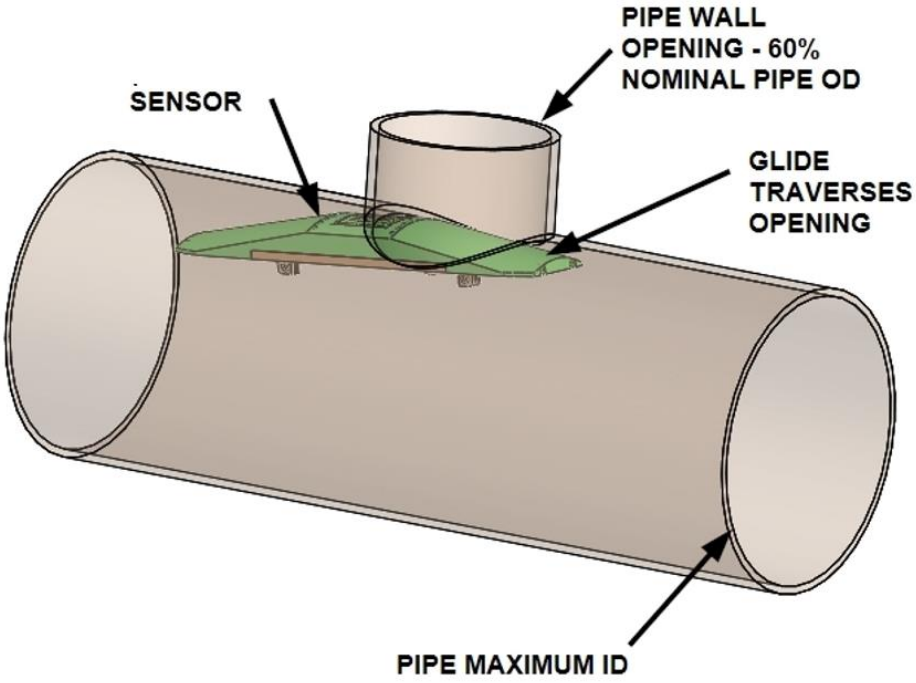

Figure 26. Sensor Traversing a 60% Opening

Glide Assembly

The glide assembly is illustrated in Figure 27. This assembly consists of the glide supported by a backplate. On the side opposite the glide, the backplate has features for suspending it from the pig body.

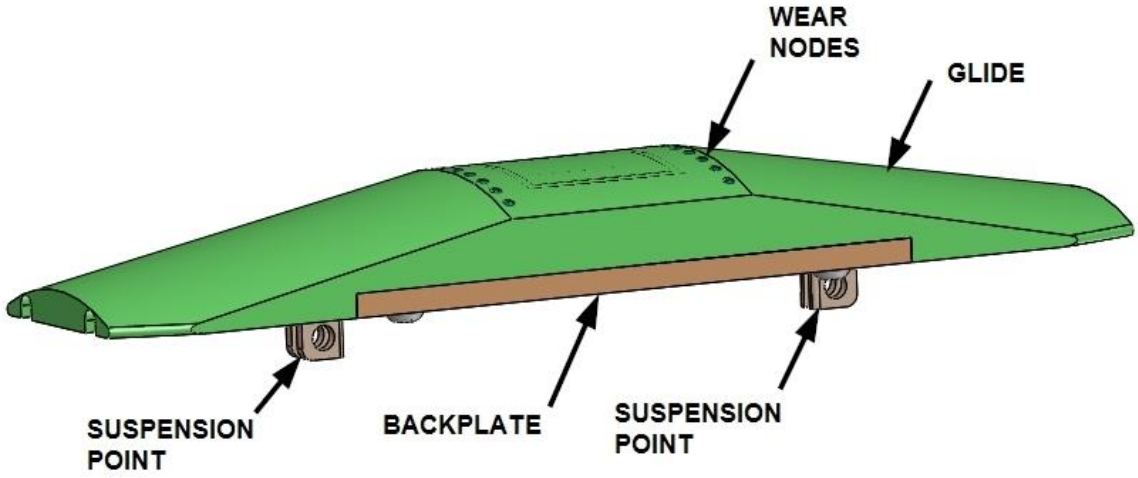

Figure 27. Glide Assembly

The key to the mechanical operation of the receiver assembly is the glide. These are made of highly wear-, abrasion-, and impact-resistant materials. This ensures long reliable life while sliding against the pipe wall. The glides are also configured to guide the receiver over protrusions, around pipe bends and across openings as previously discussed. To guide the assembly over protrusions, the glide has a leading taper on both ends. Thus as a protrusion is encountered it slides along the taper lifting the glide and its end of the magnet assembly over the obstacle. Leading tapers are required on both ends (inner and outer) of the glide to provide the capability for the glide to slide over protrusions when traveling in either direction.

To ensure long reliable life the glide is designed to resist wear, abrasion, and impact. The body of the guide is constructed of Ultra High Molecular Weight Polyethylene (UHMW). UHMW is a thermo plastic that has excellent wear characteristics. Thermo plastics are an excellent choice for this application as they typically present better wear characteristics than thermoset plastics. UHMW has some of the best wear characteristics as it is self-lubricating with a very low coefficient of friction. In addition it has the highest impact strength of any thermo plastics. Further it is highly abrasion resistant, being 15 times more abrasion resistant than carbon steel. UHMW has such a low coefficient of friction and is so abrasion and tear resistant it has been used as a replacement for ice in skating rinks where ambient temperatures make it impractical to maintain ice. Finally UHMW has extremely low water absorption (commonly <0.01%) and excellent chemical resistance. This ensures that the glides can operate in a wide variety of pipe products without absorbing the product.

The wear, abrasion, and impact resistance of UHMW can be further aided by adding other materials to it when it is manufactured. One such additive is glass or hardened ceramic. UHMW mixed with these additives has been developed for use in slides and chutes for moving bulk abrasive materials such as gravel, rock, slag, etc. Due to this extensive wear and abrasion resistance, the glass-filled version of UHMW will be used in manufacturing the glides.
One parameter to ensure long wear life in polymers such as UHMW is to keep the pressure times velocity (PV) value below a given limit. UHMW has very high PV limits. Typically this is a minimum of about 3000 psi-ft/min. For glass filled UHMW this increases to 5800 psi-ft/min. For the receiver, the force pressing it against the pipe is expected to be a maximum of 63 lbs. The rubbed area for each glide is 8.5 sq. in. giving a pressure of 7.4 psi. At a speed of 1 ft/sec this is a PV of 444 psi-ft/min. This is well below the 5800 limit indicating the glides should have very long life.

To further increase the wear and impact resistance of the glides, wear nodes are inserted along the rubbed face. These wear nodes consist of silicon nitride spheres imbedded in the UHMW. Silicon nitride is a very hard impact resistant material. These wear nodes will aid the glides in resisting impacts, particularly when traveling over protrusions such as girth welds. The glides are attached to the backplate by screws. This provides the capability to easily change the glides when they wear out.

Sensor Assembly Suspension

For incorporation into the complete tool, the receiver will be suspended from the pig body. The design of the suspension will be dependent on the pig design that incorporates an attachment mechanism (for towing/pushing) which is a future effort. This could possibly take the form of a foam cleaning pig with suspended sensors and an electronics enclosure. At this time a working concept for suspension is required to ensure that the sensor assemblies can be incorporated into a feasible pig with sufficient collapse factor. The current design concept for sensor suspension employs a suspension cable at each end of the sensor that runs to the pig body. These serve to transmit the towing forces from the pig body to each sensor. They also act to limit the extension of the sensor away from the body. The sensor suspension system also incorporates a foam spring. While the magnets provide some force to hold the sensor against the pipe wall, the spring applies additional force. This ensures that the sensor rides on the wall and rapidly returns to contact with the pipe wall after passing over a protrusion. Figure 28 presents the sensor suspension.

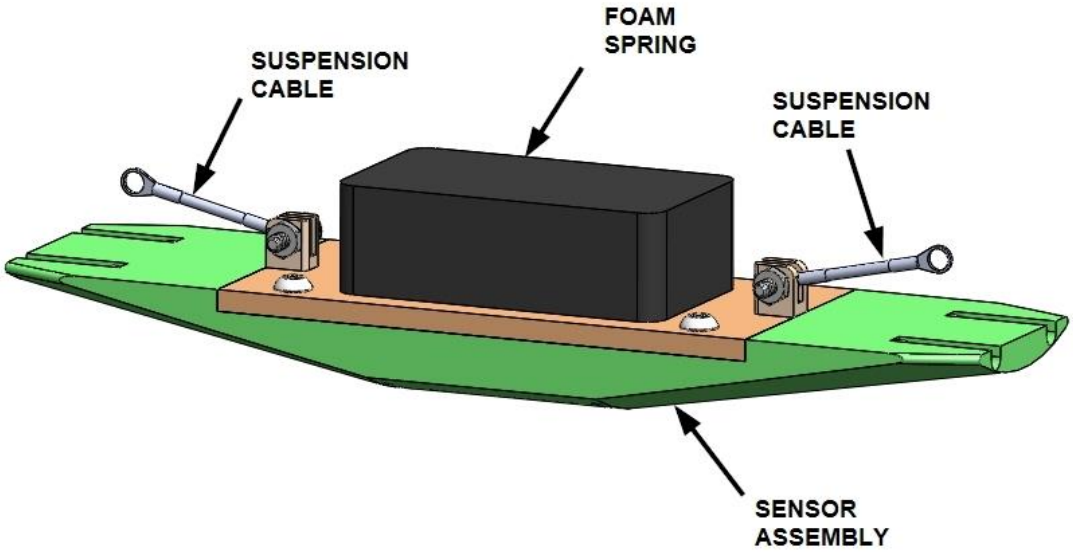

Figure 28. Sensor Suspension

4. Sensor Mounting Design

This section provides further details for the sensor suspension and mounting design.

The EMAT Sensor Design Section presented a design for the sensor portion of an EMAT tool. The tool is intended to be used for scanning 8" pipe with regard to crack detection. In that section, a concept for suspending the sensor assemblies to a pig body to make an ILI tool was also presented.

The suspension was designed to meet the primary physical requirements that would be imposed on the desired ILI tool. Primarily these included use in an 8" diameter pipe, provide better than 85% collapse factor, and negotiate 1.5 D bend. The design must also provide means to keep the sensors in contact with the pipe wall during the inspection process.

The following presents the design details for the suspension mount.

Mechanical Design

Sensor Mechanical Design Overview

The primary mechanical design requirements for the small diameter EMAT sensor is that it must be incorporated into a towable pig for inspecting small diameter (8") pipe. For this section, mounting the sensors as they would be used in a pig is the primary focus. The mounting system must allow the sensor to move inward and outward from the pig body over a significant range of motion. This range extends from a minimum to meet the designed collapse factor to a maximum that occurs in a pipe with a minimum wall thickness. Additionally, the mounting system must provide a force to ensure the sensors remain in contact with the pipe wall. To meet these goals the mounting system design combines a cable suspension together with a foam spring. The cables are arranged to provide the required motion while attaching the sensors to the pig body, while the spring provides the force to press the sensor against the pipe wall.

The complete EMAT ILI tool concept uses four sensors arrayed about the pipe diameter. Two of the sensors act as transmitters and two act as receivers. The physical configuration of the two types of sensors is slightly different, however the mounting is the same, resulting in only one type of required mount design. The SolidWorks, 3D model in Figure 29 illustrates the sensor arrangement in the overall pig concept.

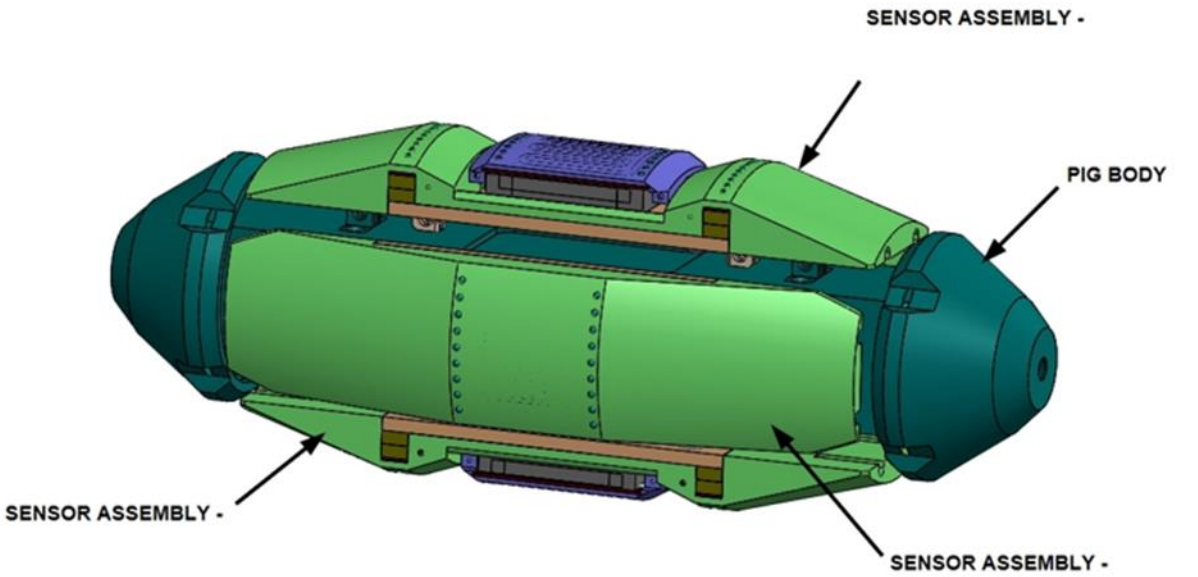

Figure 29. Sensor Assemblies & Pig Concept

Sensor Mounting Mechanical Requirements

Table 7 presents the basic mechanical design requirements for the sensor mounting system.

Table 7. Mechanical Requirements

Requirement	Value
Temperature Range	40F – 90F (4.4 – 32.2C)
Operating Pressure	Maximum 1000 psig (6.89 MPa)
Pipe Size	8” nominal OD
Pipe Wall Thickness	0.25 - 0.50 inch (6.4 – 12.7 mm), (schedule 20 – 80)
Collapse Factor	85% or better (percent nominal OD)
Minimum Bend Radius	1.5 x nominal OD
Bi-directionality	Yes
Weld Protrusion	0.125 inch (3.2 mm)

Basic Design Considerations

To meet the stated requirements the sensor mount design incorporates design elements in keeping with the stated values. The following outlines how the requirements are met:

- The temperature range is modest and the mount system uses materials that operate within this range. The materials are also commonly found in pig designs.
- The mount does not have any sealed cavities. This allows the surrounding pressure to act hydrostatically on all components. The foam spring is a porous material. To prevent pressure induced collapse of the foam, open cell foam is used.
- The mount system is designed to allow the sensors to move inward and outward from the pig body to meet the range of pipe schedules, fit around pipe bends, and move inward sufficiently to meet the collapse factor.
- Wall thickness tolerances are also used at the limits for determining the range of sensor motion.
- Good pig design practice goes beyond the stated 85% collapse factor to 80%. For this design the mount system provides a range of inward motion to meet an 80% collapse factor.
- The mount system provides sensor motion to fit through a 1.5 OD pipe bend at the minimum pipe diameter.
- The mount system is symmetrically configured. This provides the capability for the sensors to be towed along the pipe in either direction ensuring bi-directional operation.
- The mount system provides the capability for the sensor to move through a rotational angle allowing it to navigate over a greater than 0.125” protrusion.

Sensor Mount System Configuration

Figure 30 illustrates the sensor mount system design while Figure 31 illustrates the sensor suspension system. This consists of clevis type mount points attached to both the sensor and the pig body. The mount points are located towards each end of the sensor and each end of the pig body. A cable lanyard runs from a mount point on the pig body to the adjacent mount point on the sensor. The lanyard is attached to each mount point by a pin (shoulder screw) that passes through the clevis of the mount point. This allows the lanyard to rotate about an axis, through the clevis oriented parallel to the surface of the pig body and the sensor, and perpendicular to the direction of pig motion. This arrangement allows the sensor to float through a range of motion toward and away from the pig body.

The magnets produce force that pulls the sensor against the pipe wall. This force is on the order of 20 lbs and is centralized under the magnets. To ensure consistent force between the sensor and the pipe wall a foam spring is utilized. The spring is located between the pig body and the sensor. This exerts an outward force pushing the sensor away from the body. The spring is sized so that it produces force on the sensor even at the maximum range of motion.

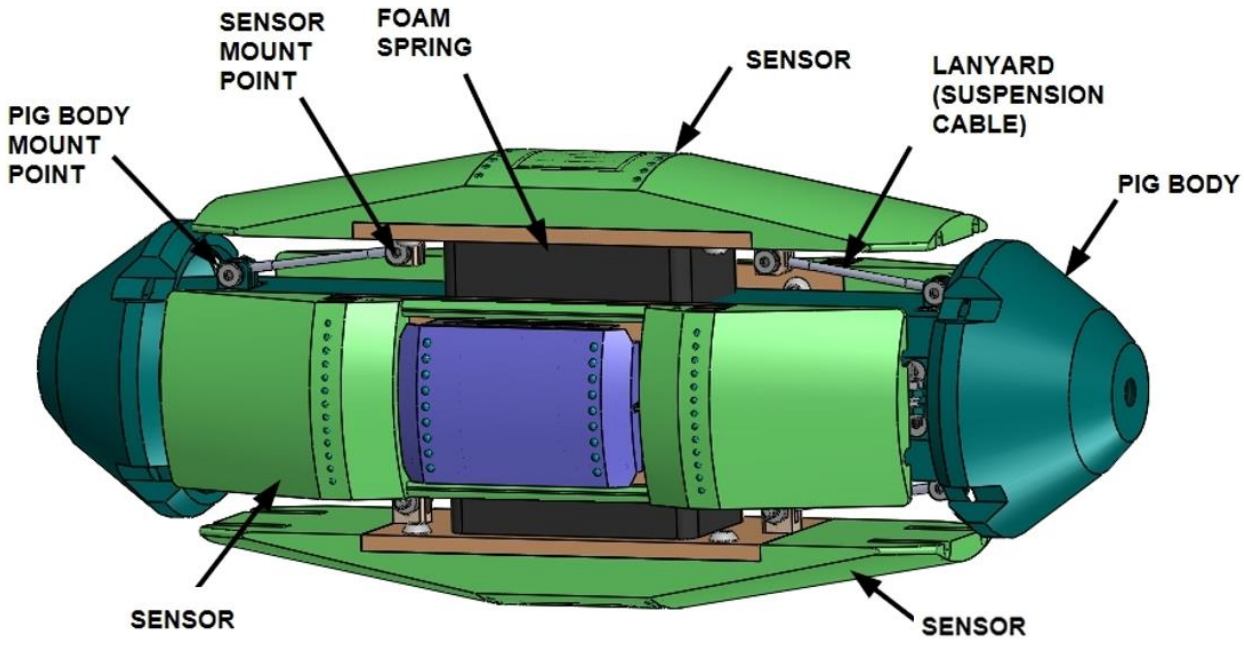

Figure 30. Sensor Mount System

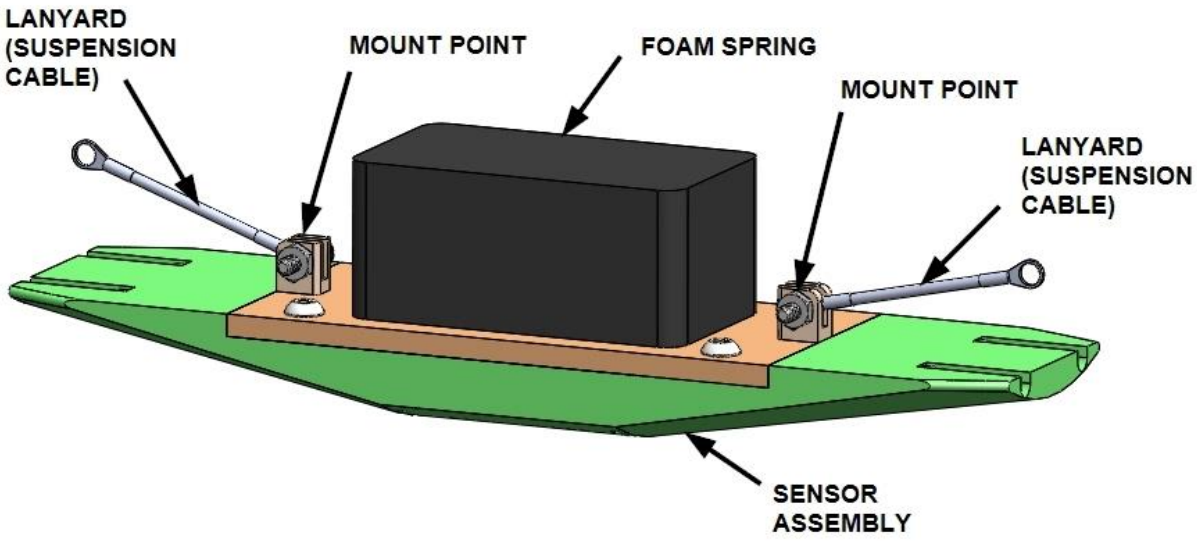

Figure 31. Sensor Suspension

Lanyard Design

There are three primary considerations in the design of the lanyards. These consist of length of the lanyard, location of the mount points, and strength of the lanyard. The lanyards must be

sized to allow the sensors to move outward to meet a pipe with a maximum inner diameter (thinnest wall). As the sensor moves inward toward the pig body some slack will develop in the lanyards. This will allow the sensor to move along the pig body. This motion can be minimized by minimizing the angle formed between the lanyard and the pig body. The angle is minimized by maximizing the length of the lanyard. To meet this goal, the mount points are located a maximum distance along the pig body. In this design the angle ranges from 2.7 degrees at full collapse to 20.6 degrees at maximum extension. This results in a small movement of 0.185" of the sensor along the pig body from maximum extension to full collapse.

As slack develops in the lanyard it is possible for the sensor to rotate with respect to the pig body. To minimize possible rotation, advantage is taken of the friction force between the pipe and the sensor. The mount points are located in the center of the width of the sensor. This puts the towing force generated by the lanyard in the center of the sensor. Friction forces generated by the sensor sliding on the pipe wall are spread across the width of the sensor. As the pulling force is in the center of the sensor while the drag forces are towards the edges, a moment is generated that always drives the sensor to be in line with the towing force. This causes the sensor to remain centered across the width of the pig body.

The final consideration is the strength of the lanyard. The maximum force generated by the magnets plus the foam spring is less than 65 lbs. With a 0.1 coefficient of friction, the maximum drag force on the lanyard is less than 6.5 lbs., however this could increase when encountering an obstacle such as a weld bead. The lanyard is made of braided stainless steel cable. The cable has a working strength of 94 lbs. This provides a factor of safety of over 14. If an obstacle increased the drag force by a factor of 2 the factor of safety would still be over 7.

Spring Design

The spring is required to provide force to press the sensors against the pipe wall and to maintain sensor orientation with the central pig axis. The force to press the sensors against the pipe wall is a simple force vector acting outward away from the pig body. This can be obtained by a single point force. However the forces to maintain sensor orientation are not simple forces. As the sensor rotates about its axis and with respect to the pig axis, it increases the distance from the body to the sensor on one side while reducing the distance on the other side. Returning the sensor to an even orientation (both distances equal) requires an increase of force on the short distance and reduction of force on the other. This essentially produces a moment (force acting at distance about a point of rotation) on the sensor. The restorative moment could be obtained either by using multiple springs, or by using a single spring that acts across the sensor width from one side to the other. The latter is a simpler approach and was used for this design.

Elastomeric foam is used extensively in the pigging industry. These uses range from components used in pigs to entire pigs being made strictly of foam. The virtue of foam is that it acts as a spring over a large area. Additionally it has very high compression capability. This allows highly collapsible components or entire pigs to be made that will spring back to their uncollapsed state as soon as constraint is removed. High chemical resistance polyurethane foam is typically used. This is available as either open cell or closed cell. For this application, open cell foam was chosen. This allows any materials flowing in the pipeline to pass through the pig. Foam will develop varying pressures with regard to the amount it is compressed. Table 8 presents the pressure vs. compression percent for 5 lbs/cu ft polyurethane foam.

Table 8. Foam Compression

% Compression	Pressure
10	2.5
20	2.9
30	3.2
40	3.6
50	4.3
60	5.9
70	10.6

Compression in the current design ranges from about 12% at full extension to about 65% at full compression. Using an 8 square inch piece of foam provides about 12 lbs. load at full extension and about 41 lbs. at full compression. Combined with the magnetic forces, this provides about 34 lbs. pressing the sensor to the pipe wall at full extension and about 63 lbs. at full compression. This range provides significant force to keep the sensor against the pipe wall while preventing excessive load at full compression.

Range of Motion

The presented design allows the sensors full motion to cover the entire specified operating range. This extends from full collapse at 80% nominal pipe diameter (6.4") to full extension (8.125"). Figure 32 shows the sensors at full extension while Figure 33 shows the sensors at full compression.

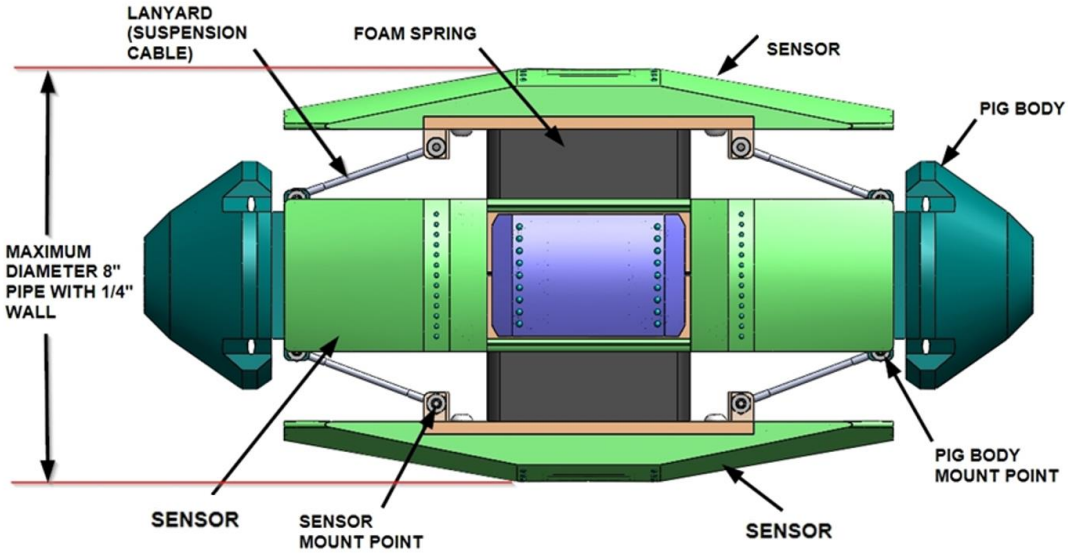

Figure 32. Sensors at Full Extension

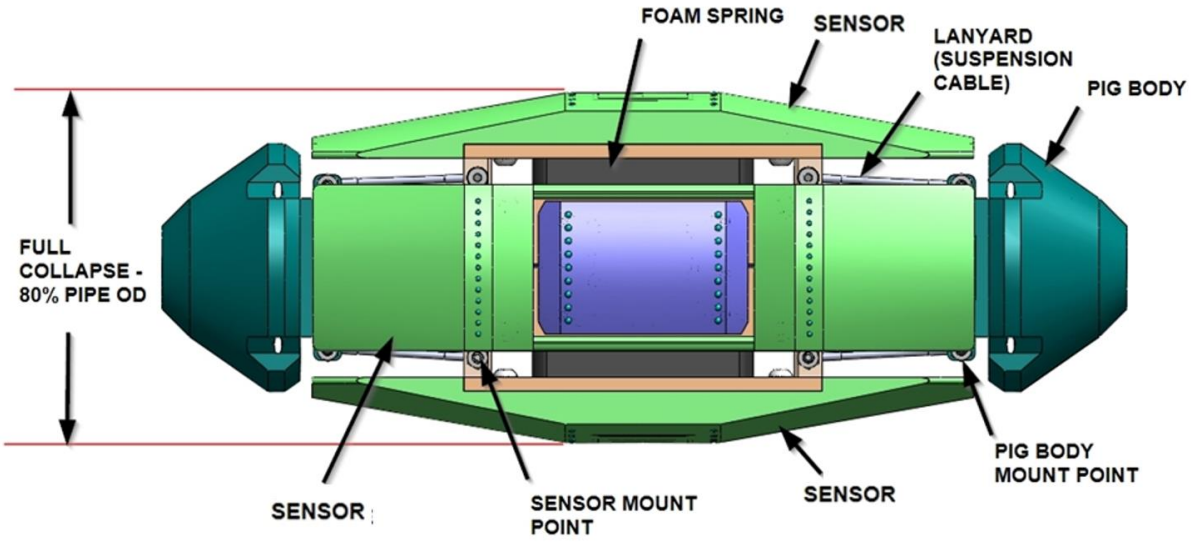

Figure 33. Sensors at Full Compression

5. Sensor Prototype Production

This section provides the details of the prototype and test fixture production.

The Sensor Design Section and the Sensor Mounting Design Section presented a design for the sensor portion of an EMAT tool along with a design for mounting the sensors to a pig body. The tool is intended to be used for scanning 8" pipe with regard to crack detection. The designs presented in these sections can be combined with a pig body to make a complete inspection tool. These designs have been manufactured to produce a bench scale prototype tool for test purposes.

In addition to the prototype tool, a fixture was designed and manufactured for attaching the prototype to a translation stage. This provides the capability of dynamically testing the prototype.

Mechanical Design

Prototype Design

The prototype design is based on the sensor designs presented in the Sensor Design section and the Sensor Mounting Design section. To make a complete pig, two transmitters and two receivers are used. The pig is configured so that the transmitters and receivers are at 90 degrees with the two transmitters are opposite each other as are the receivers. The SolidWorks 3D model in Figure 34 illustrates the sensor arrangement in the overall pig

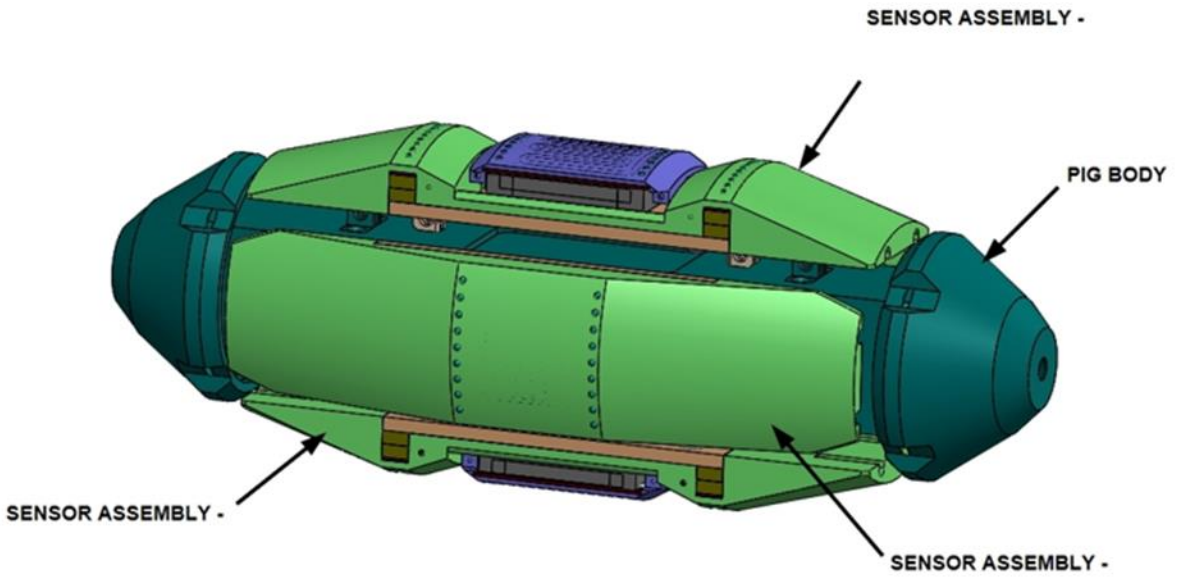

Figure 34. Sensor Assemblies & Pig

For the prototype, not all four sensors were used. However to function in a pipe and properly activate the mount system, four devices are required surrounding the pig body. For this purpose two dummy units were designed. One was physically configured to match the transmitter and the other was configured to match the receiver. The mounting system for the dummies is the same as that for the sensors. The dummies together with a live transmitter and receiver were used to make a complete pig. Figure 35 illustrates the sensor 1 dummy while Figure 36 illustrates the sensor 2 dummy.

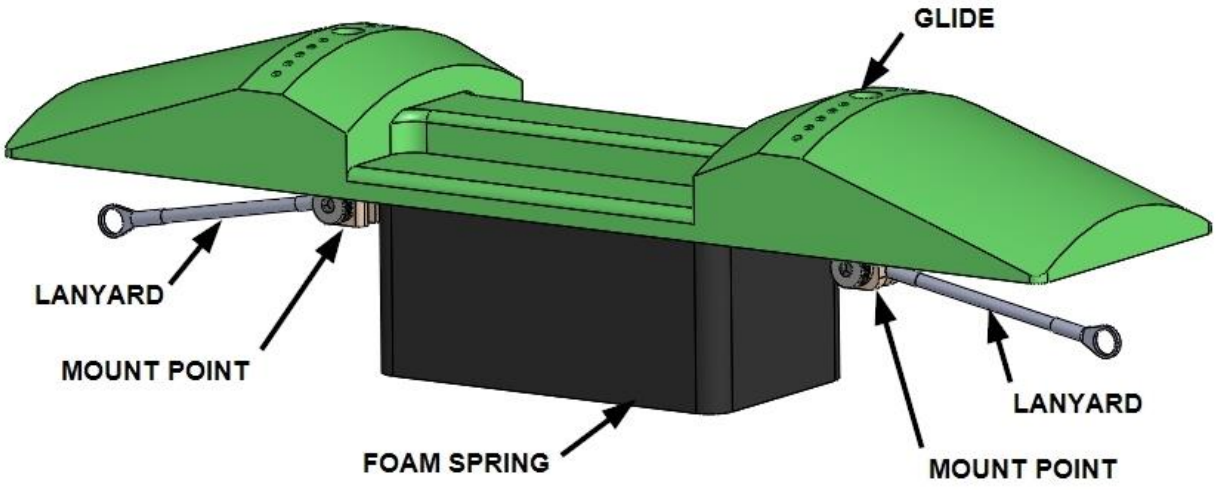

Figure 35. Sensor 1 Dummy

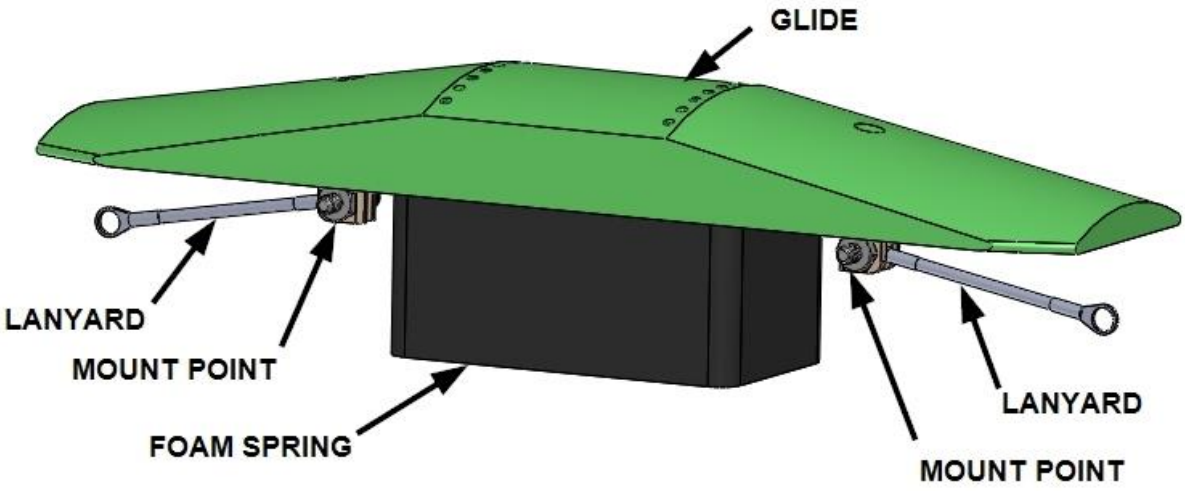

Figure 36. Sensor 2 Dummy

Materials to produce the dummies were the same as those used for the active components. The lanyards are made of the same cable as those used for the transmitter and receiver. As the configuration and materials of the dummies match that of the active components, the dummies

will act inside a pipe exactly the same as the active components. This will provide the capability of testing with a single transmitter and receiver while obtaining the same motion and wear characteristics as a complete pig.

The pig body varies from that of a complete pig. This is to provide the capability of attaching the pig with dummies to the test equipment. One end of the body is configured to directly match up with a coupling on the test fixture. The pig body is only an approximation of what an actual pig might incorporate. This is due to the current effort being directed at designing the sensors and not a complete pig. Actual pig body design will take place at a later date.

Test Fixture Design

The purpose of the prototype pig is to conduct operational tests. In order to perform these tests the pig will be traversed back and forth inside a pipe. To provide this capability a test fixture was designed. This fixture consists of the prototype pig mounted to a fixture that attaches to a motorized linear stage. A pipe is placed around the pig. The stage is capable of operating over a 28" stroke. Velocity capability exceeds the 1 ft/sec for pig operation. The fixture includes a support roller at the end of the linear stage. This roller acts to support the forces that act perpendicular to the stage induced while moving the pig inside a pipe. Figure 37 illustrates the test fixture.

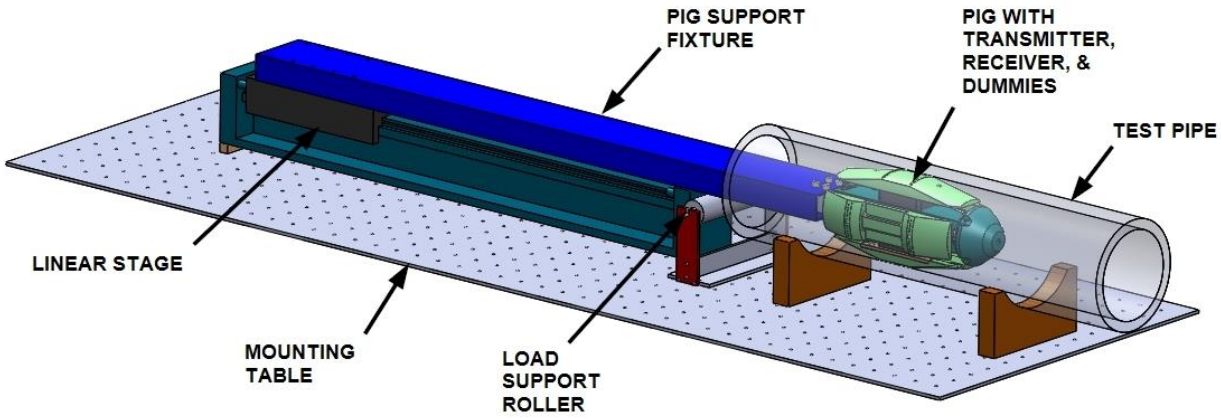

Figure 37. Test Fixture

Prototype Manufacture

To develop the prototype, the sensors, dummies and a pig body were manufactured. This was performed by creating a complete mechanical drawing package of all manufactured components. These drawings were then sent to machine shops to fabricate the parts. Most of the components were produced by conventional machining processes, with some produced in-house and others produced by outside machine shops.

Prototype Fabrication Overview

To complete the prototype, the unit was fabricated from the manufactured components along with vendor supplied components. The fabrication was performed by assembling the components into sensor 1 and sensor 2, and dummy assemblies. These were then assembled together with a pig body to make the complete unit. Each assembly was electrically wired as it was assembled.

Sensor 1 Fabrication

Figure 38 presents components of the sensor 1 assembly. These components were assembled together in three phases. First the coil assembly was completed and then the magnet and yoke assembly were completed. These were then attached to the glide.

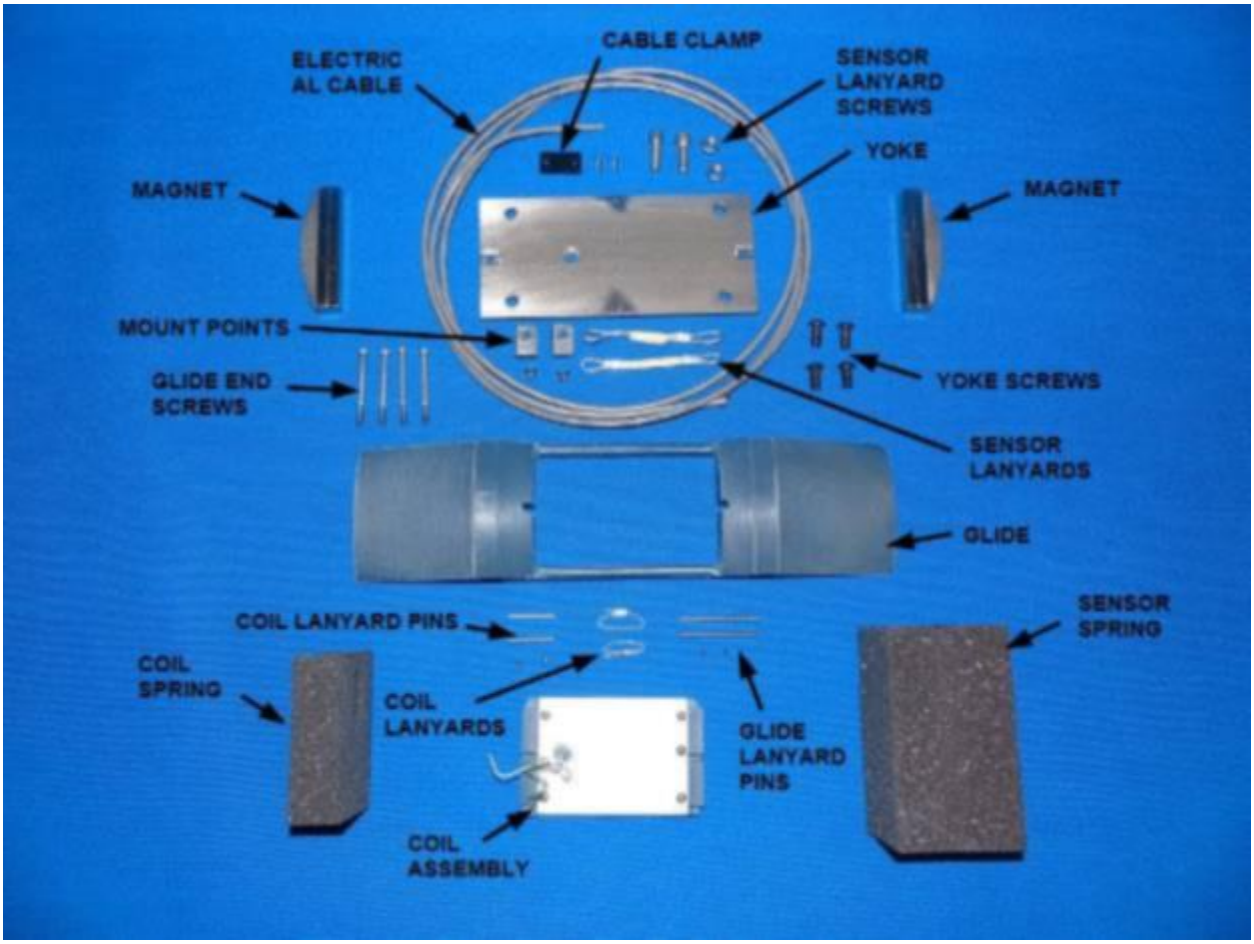

Figure 38. Sensor 1 Components

The coil assembly consists of a body, a coil, an insert and a back plate. The coil is inserted into the body as shown in Figure 39. This is followed by installing the spacer as shown in Figure 40. Finally the back plate is placed onto the body and retained by screws as shown in Figure 41. Wires lead from the coil and route through a hole in the back plate. The wires are potted in place as shown in Figure 42.

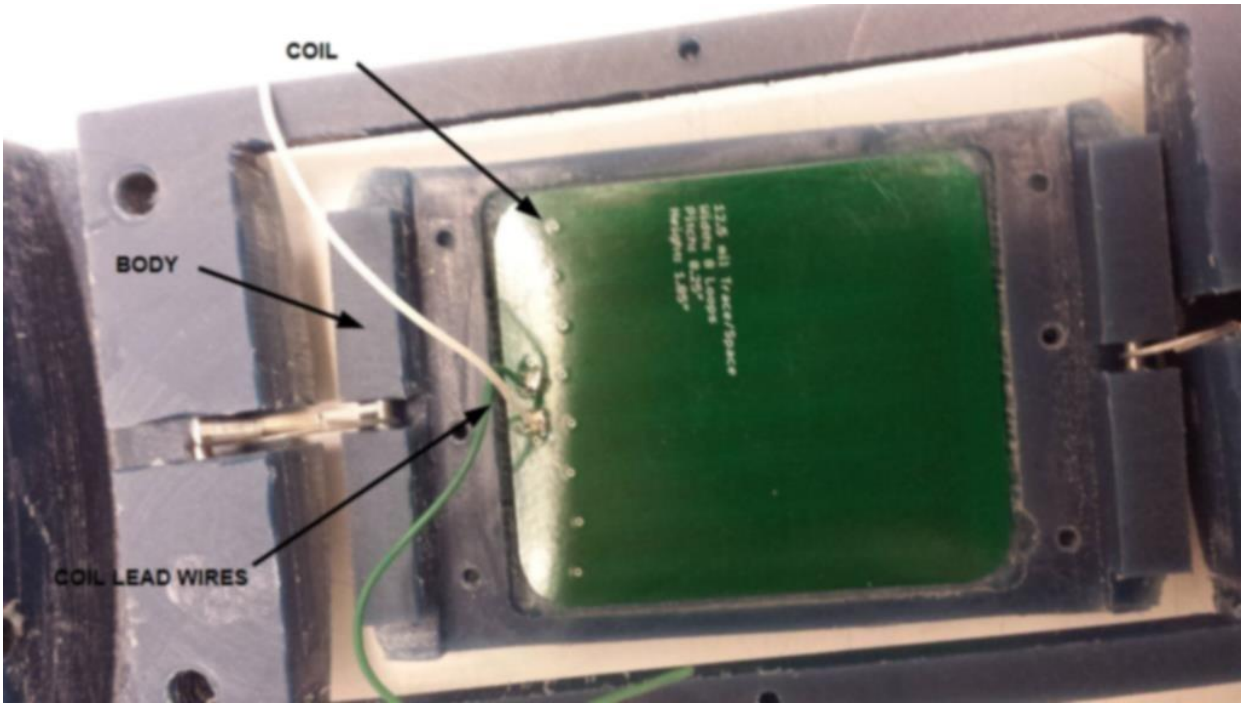

Figure 39. Coil Inserted Into Body

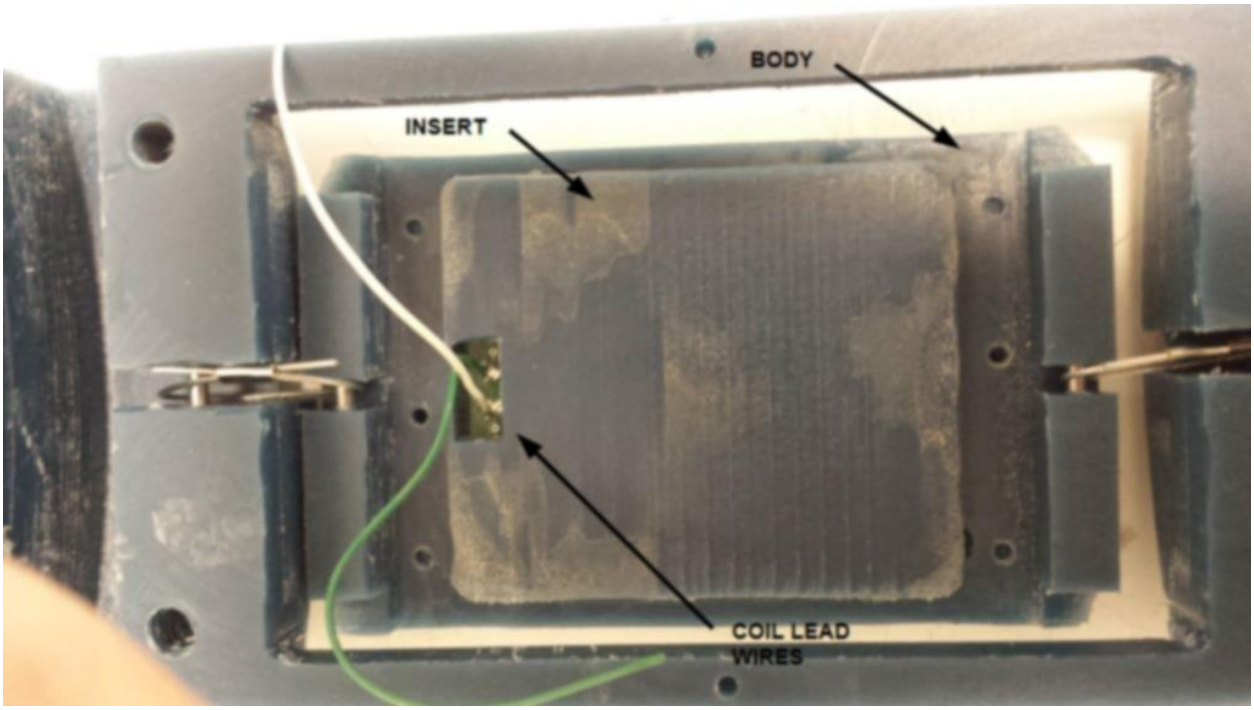

Figure 40. Spacer Inserted Into Body

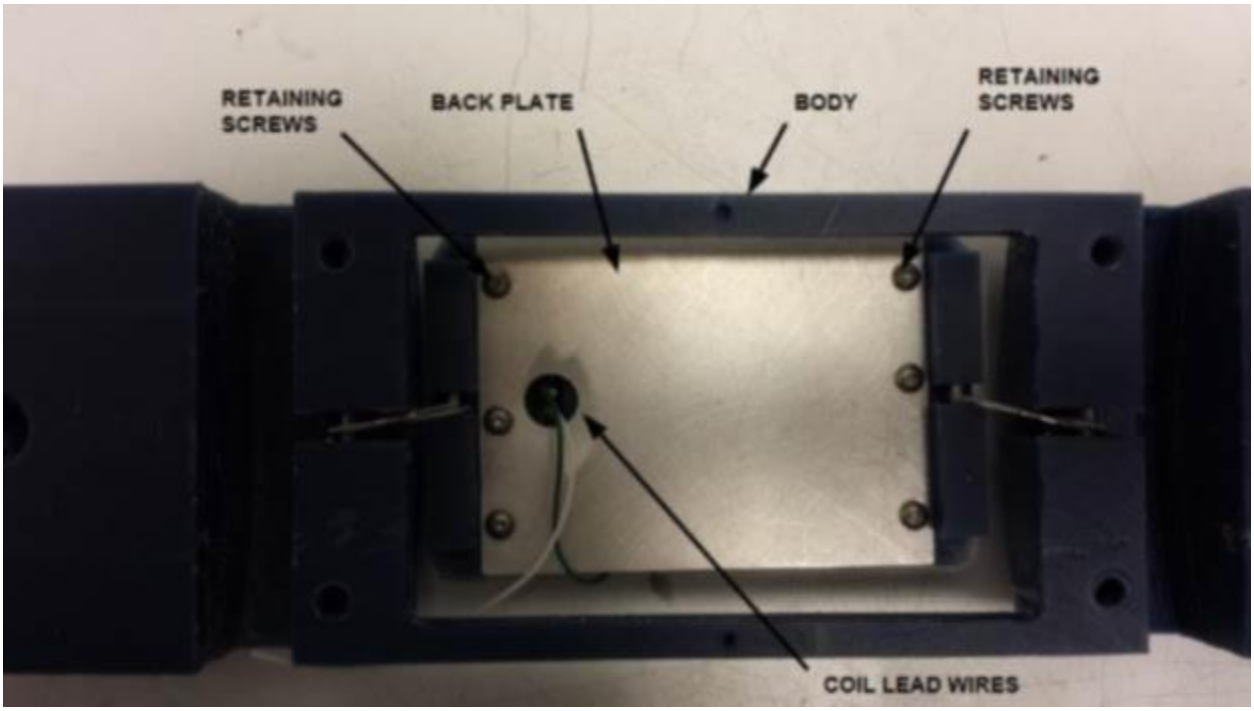

Figure 41. Back Plate Inserted Onto Body by Retaining Screws

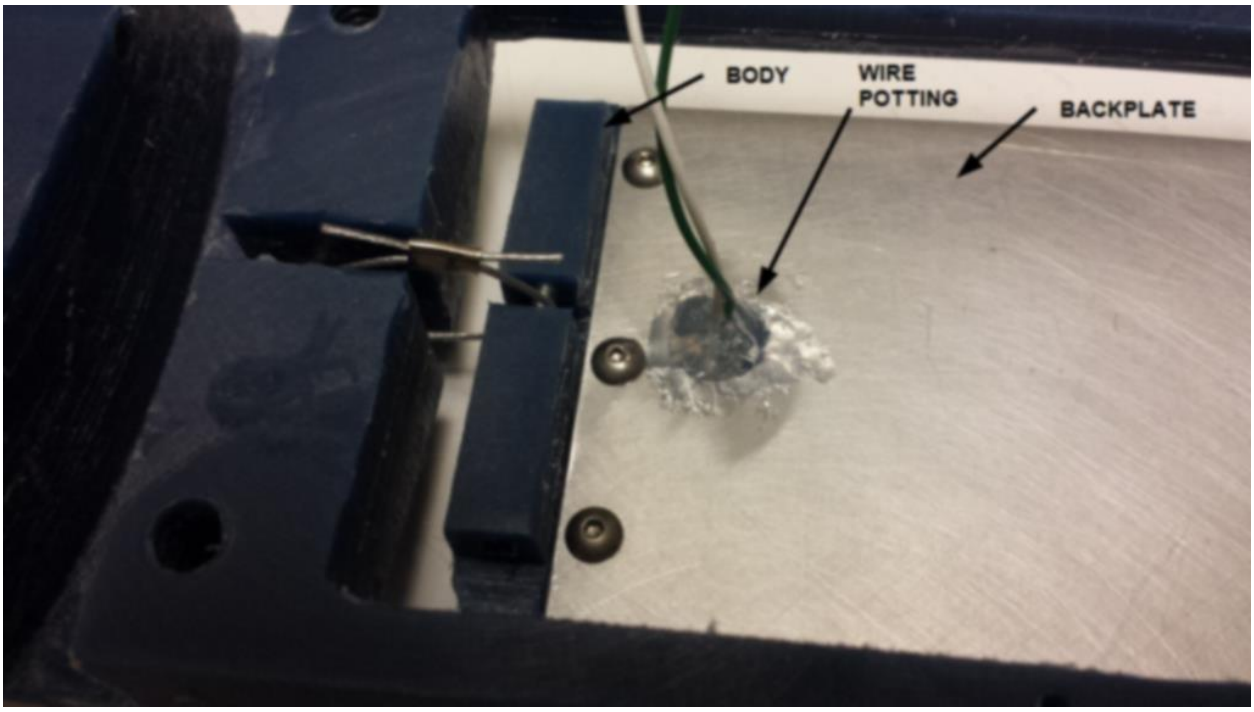

Figure 42. Wire Potting

The magnet and yoke assembly consists of two magnets with shaped pole pieces, a yoke, two mount points, a lead wire, and two lanyards. Figure 43 presents the yoke assembly components. Assembly is accomplished by attaching the mount points to the yoke by retaining screws. The magnets are then placed on the yoke. The lead wire is attached to the yoke by a wire clamp and retaining screws. The lanyards are placed into slots in the mount points and retained by screws passing through the holes in the mount points.

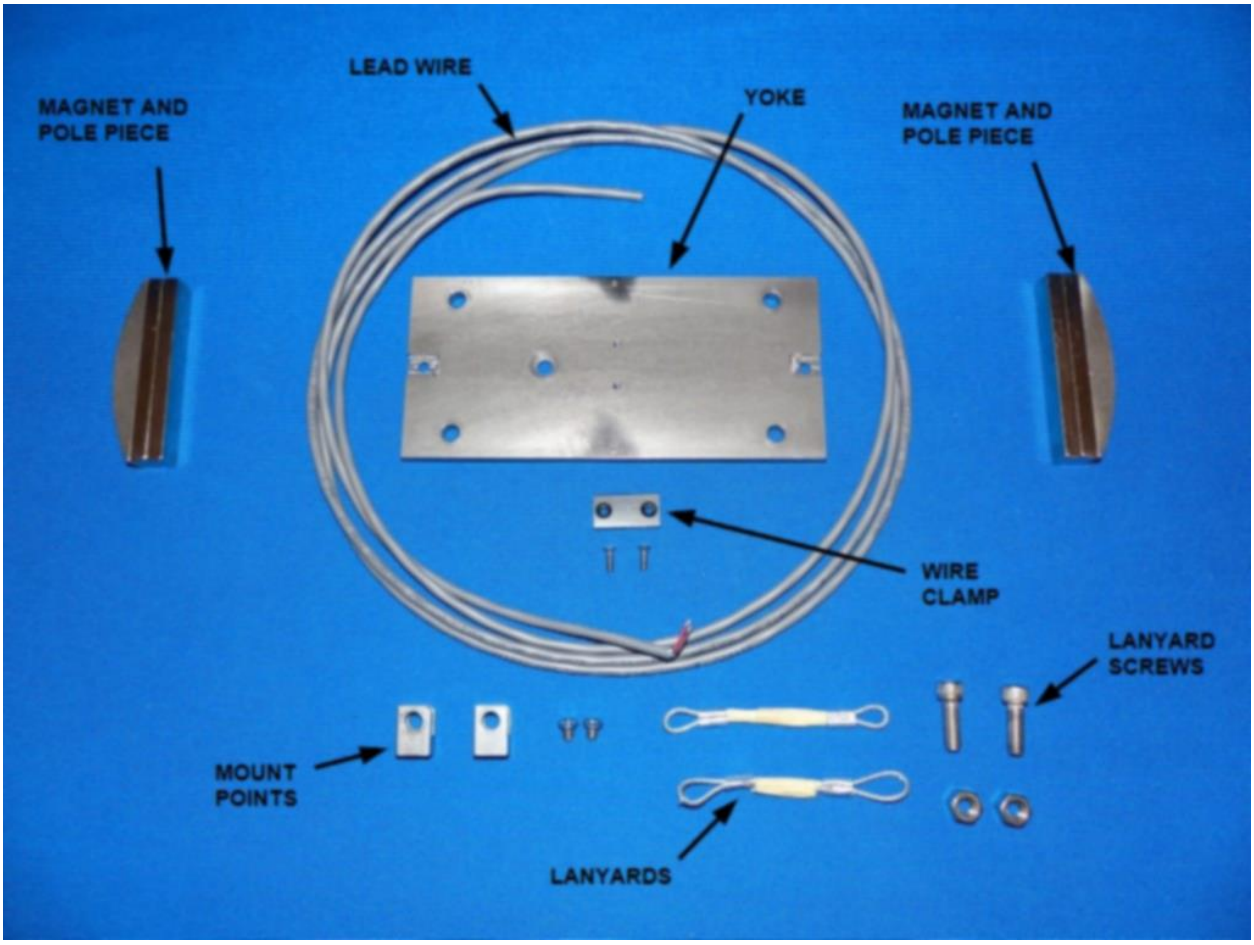

Figure 43. Yoke Assembly Components

The yoke is attached to the glide by retaining screws on the back of the yoke and in the ends to the glide. Figure 44 shows the yoke and glide components. Figure 45 shows the yoke assembled to the glide.

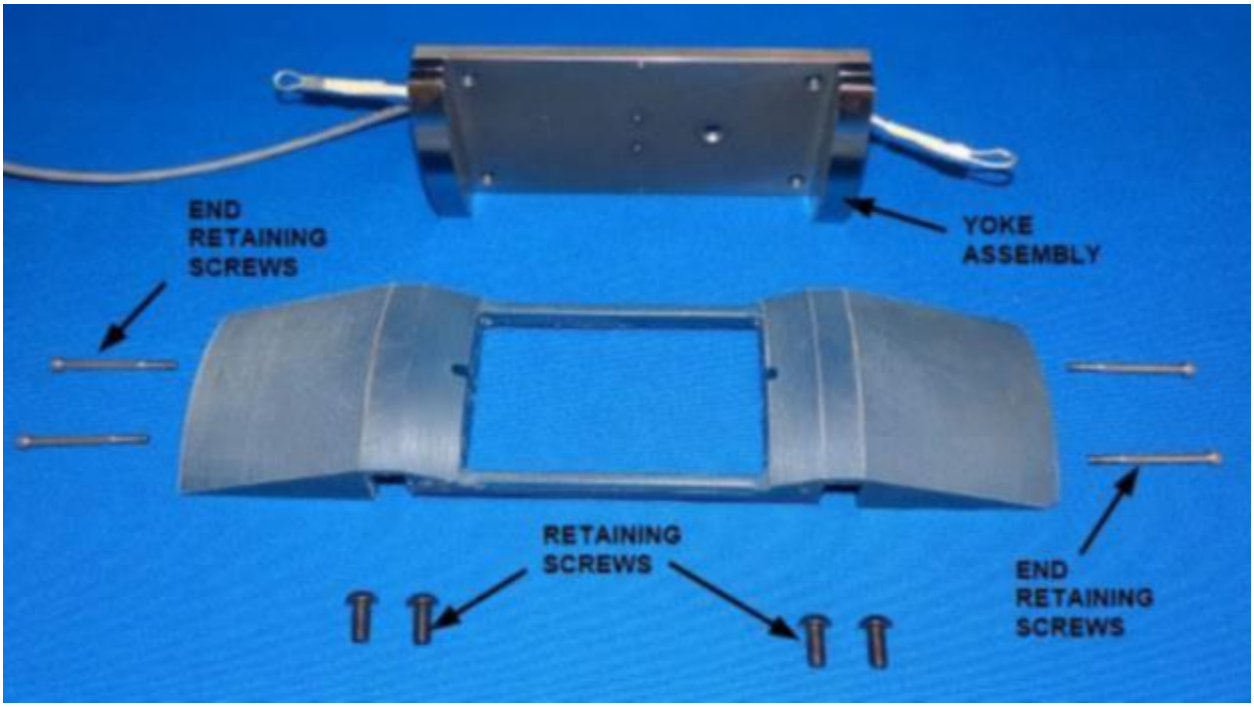

Figure 44. Yoke & Glide Components

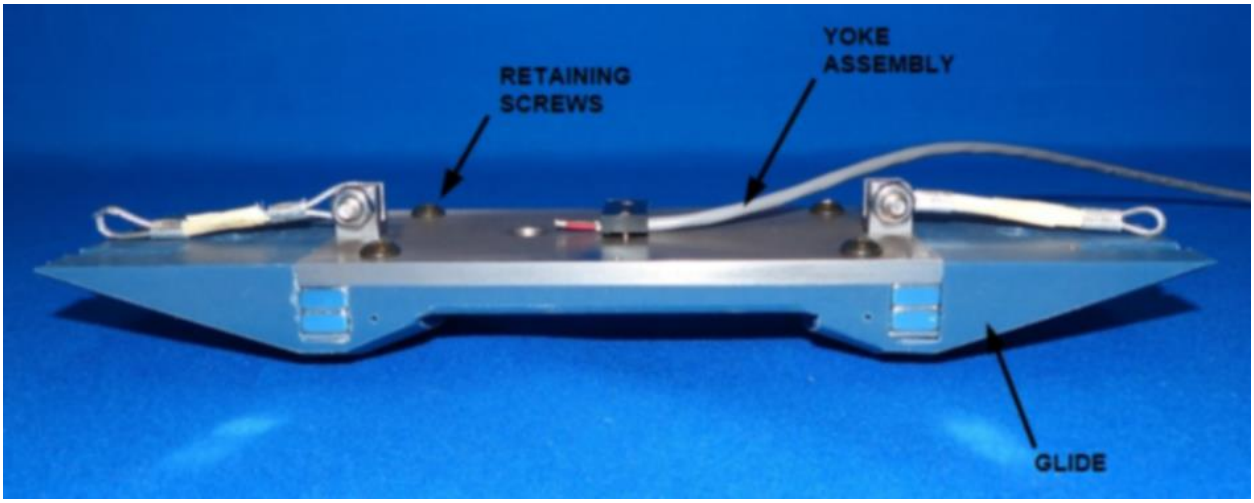

Figure 45. Yoke Assembled In Glide

The coil assembly is attached to the glide by lanyards. The lanyards are attached to the coil assembly and glide by pins. This is assembled by placing the lanyards in slots in the coil assembly and glide followed by pressing the pins into holes in the coil assembly. The pin passes through the loop in the lanyard. A set screw is then screwed into the pin hole retaining the pin in the coil assembly. Figure 46 shows the coil assembly and lanyard components. The same pin and set screw arrangement is also used for attaching the lanyard to the glide. Additionally a foam spring is placed between the coil assembly and the yoke assembly. The lead wires on the coil assembly are attached to the electrical cable on the yoke assembly. Figure 47 shows the coil and glide assembly components. Figure 48 presents the completed sensor together with a foam spring that goes between the sensor and the pig body.

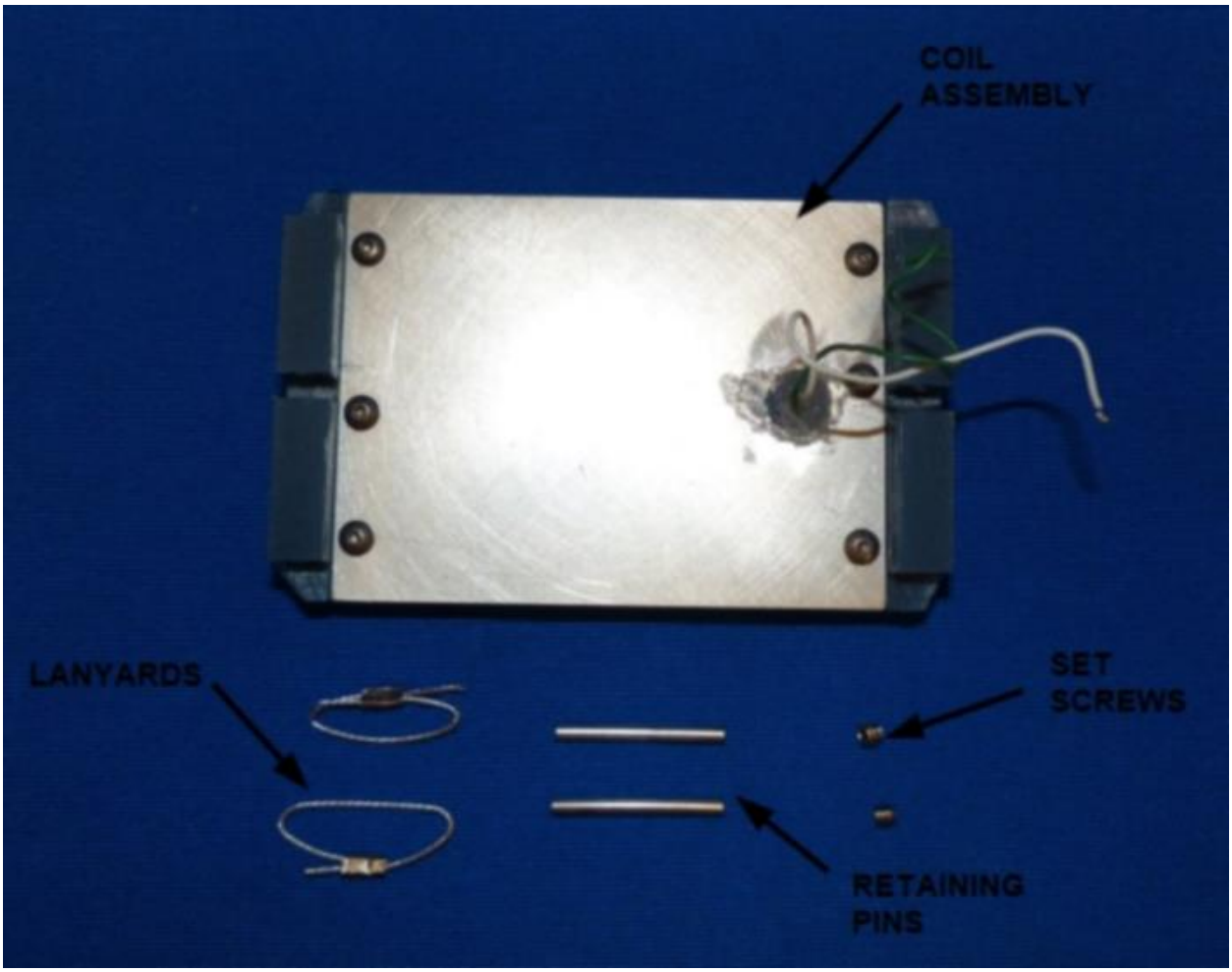

Figure 46. Coil Assembly & Lanyard Components

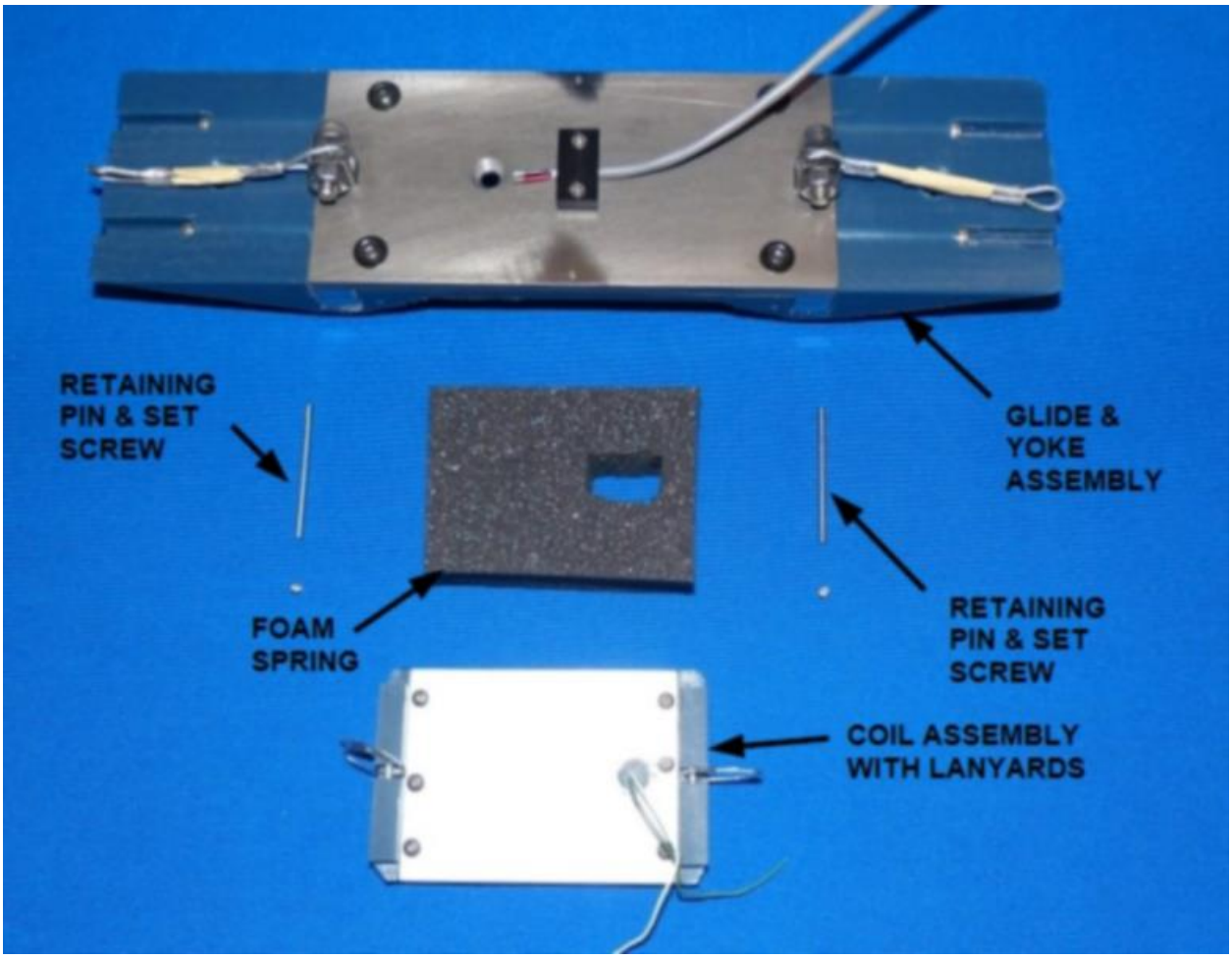

Figure 47. Coil & Glide Components

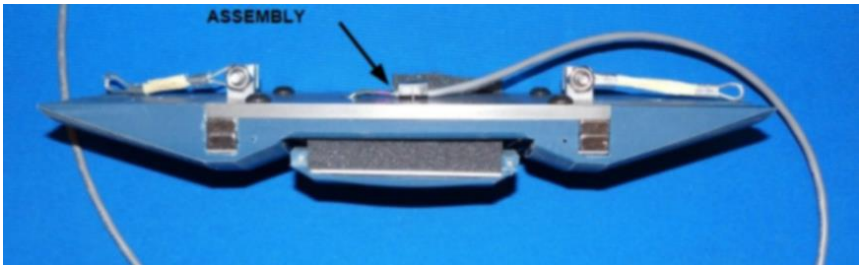

Figure 48. Completed Sensor

Sensor 2 Fabrication

Figure 49 shows the components for sensor 2. These components are assembled in three phases. First the magnet assembly is completed. Then the back plate and components are assembled. The sensor is then completed by placing the magnet assembly into the glide and attaching the back plate over the magnet assembly. The back plate is attached to the glide by retaining screws on the back of the back plate and end retaining screws in the ends of the glide.

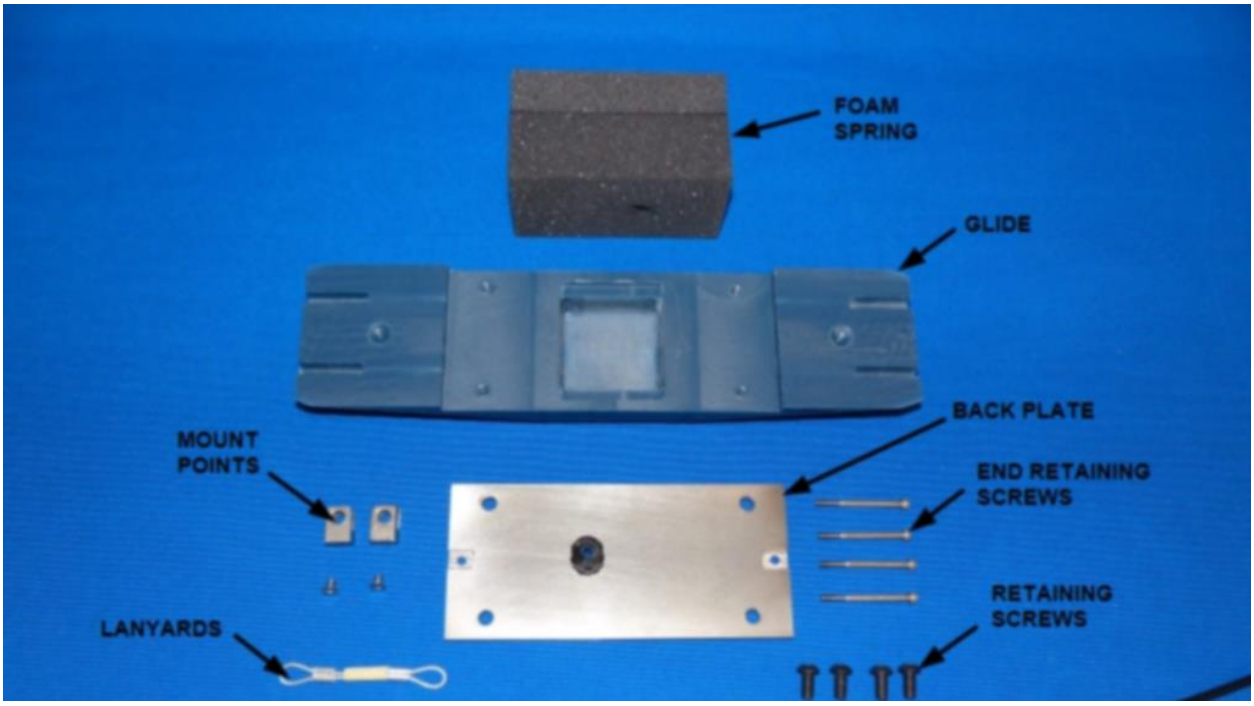

Figure 49. Sensor 2 Components

Dummy Fabrication

Figure 50 shows the components for the sensor 1 dummy assembly while Figure 51 shows the components for the sensor 2 dummy assembly. Both dummies are assembled in the same manner. The mount points are attached to the glides with retaining screws. The lanyards are then placed into slots in the mount points. The lanyard retaining screws are then inserted through the holes in the mount points and loops in the lanyards. The foam springs will be located between the dummies and the pig body. Figure 52 presents the completed sensor 1 dummy and Figure 53 presents the completed sensor 2 dummy.

Figure 50. Sensor 1 Dummy Components

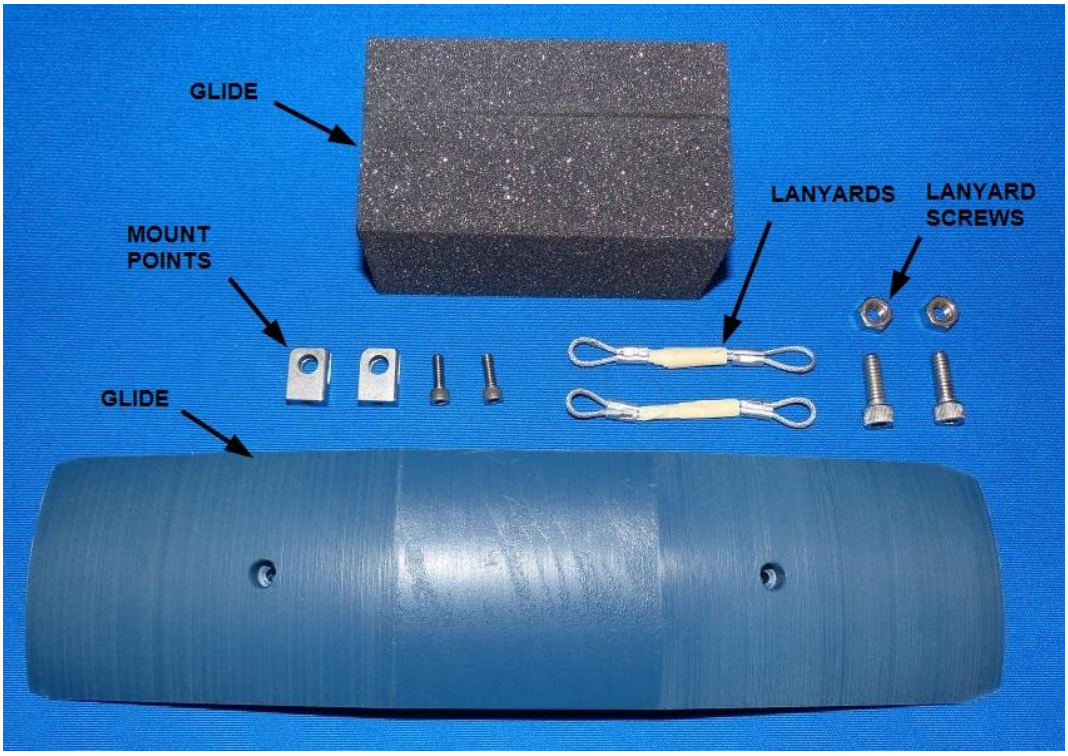

Figure 51. Sensor 2 Dummy Components

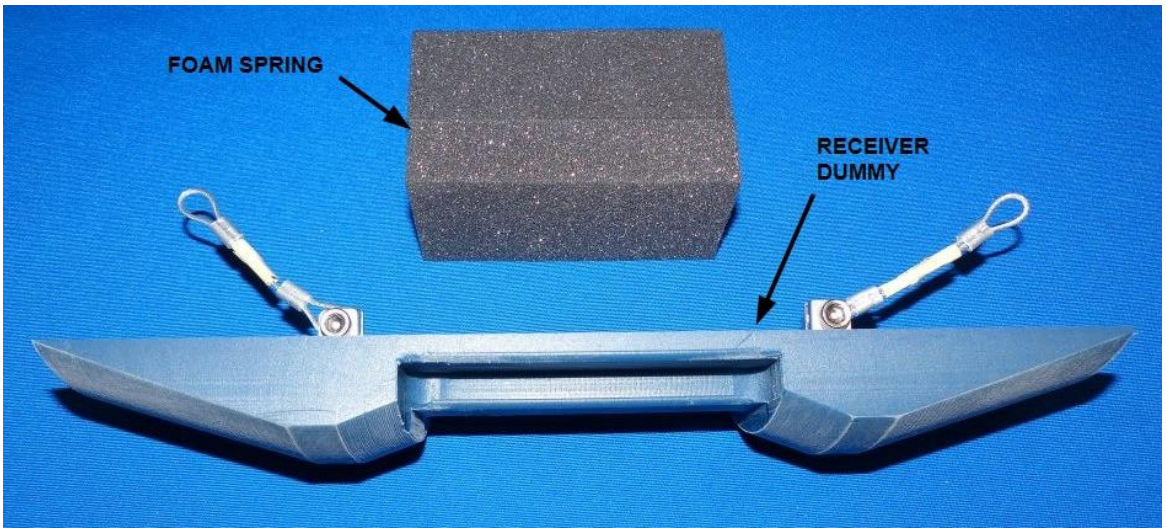

Figure 52. Completed Sensor 1 Dummy

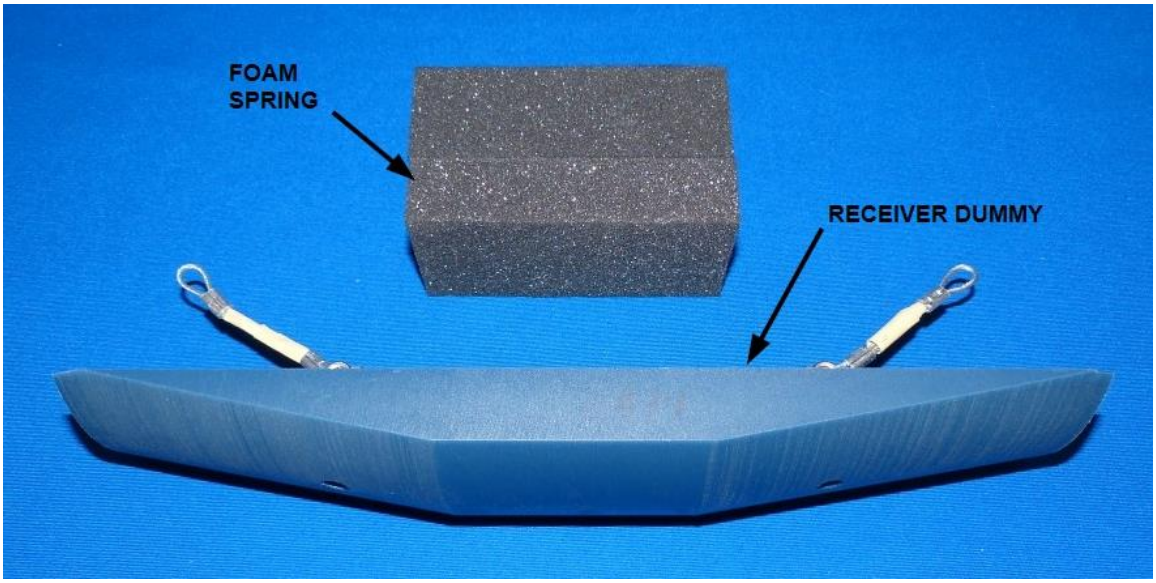

Figure 53. Completed Sensor 2 Dummy

Pig Fabrication

The completed sensors and dummies were assembled together with a pig body to make a complete pig. Figure 54 shows components for the pig body. There are eight mount points located two to each side of the body. These are retained to the body with screws. A test fixture mount is located in one end of the body. This is retained by eight retaining screws. Figure 55 shows the pig body together with a nose cone guide. The guide inserts into one end of the body. Figure 56 shows the complete pig body.

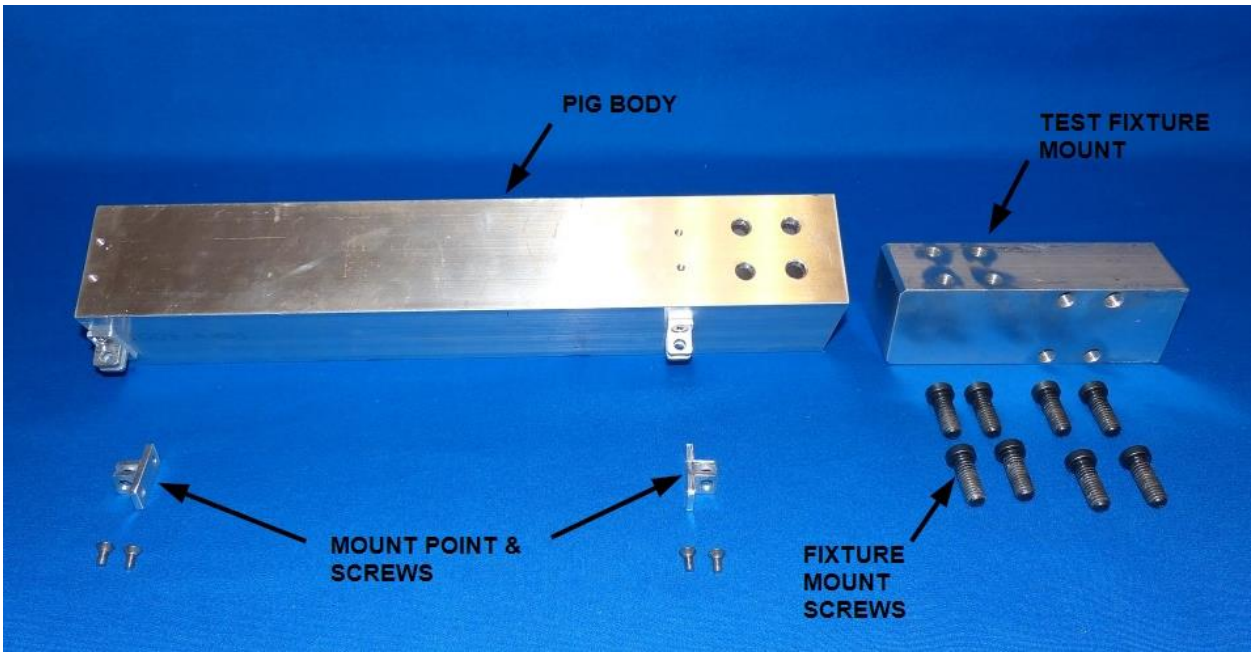

Figure 54. Pig Body Components

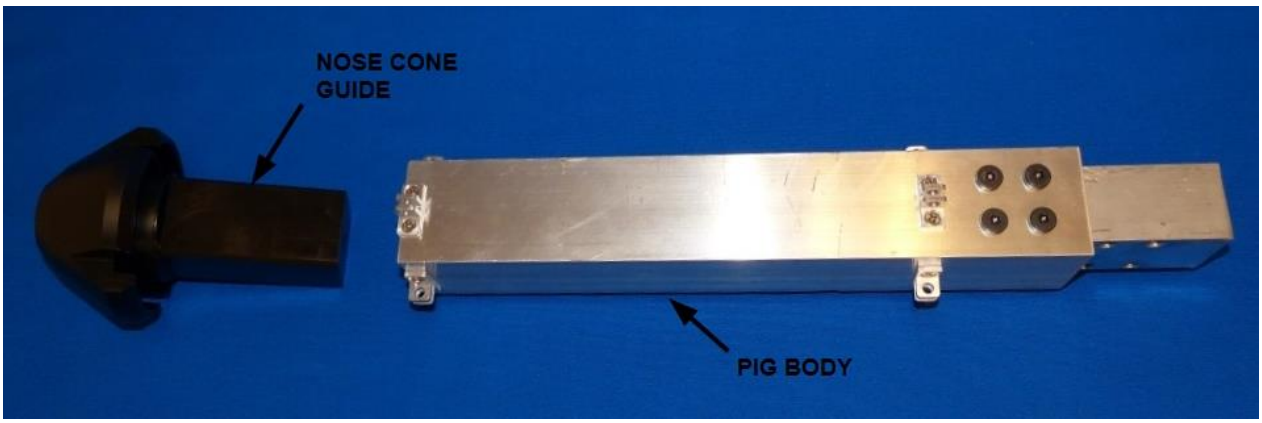

Figure 55. Pig Body & Nose Cone

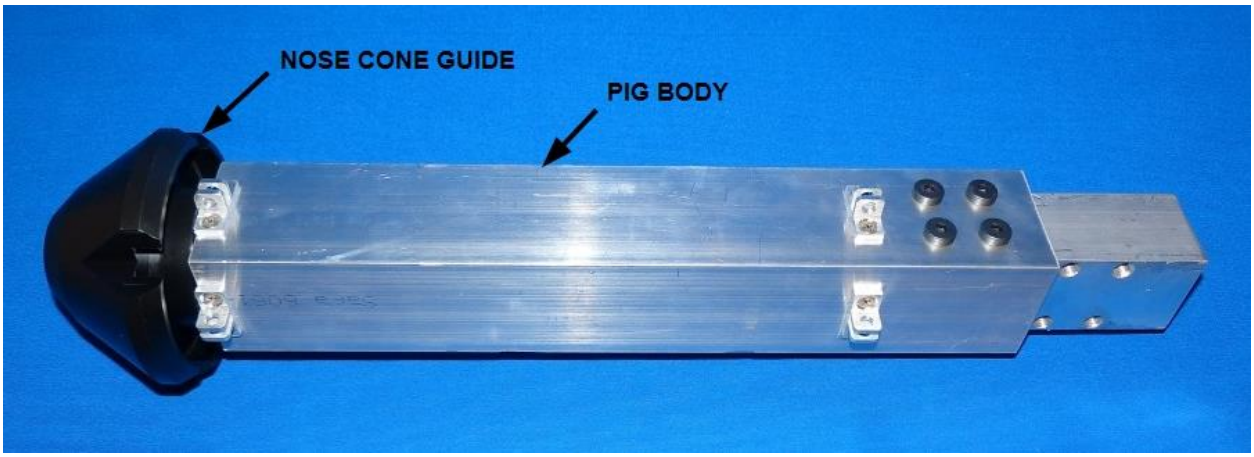

Figure 56. Assembled Body & Nose Cone

Figure 57 presents the completed pig assembly.

Figure 57. Completed Pig Assembly

To conduct testing the pig assembly is mounted to a test fixture. The fixture mount on the pig body engages a receptacle on the fixture. Retaining screws are then inserted to hold the mount to the fixture. Figure 58 presents the pig mounted to the fixture and Figure 59 shows the pig engaged in a clear pipe.

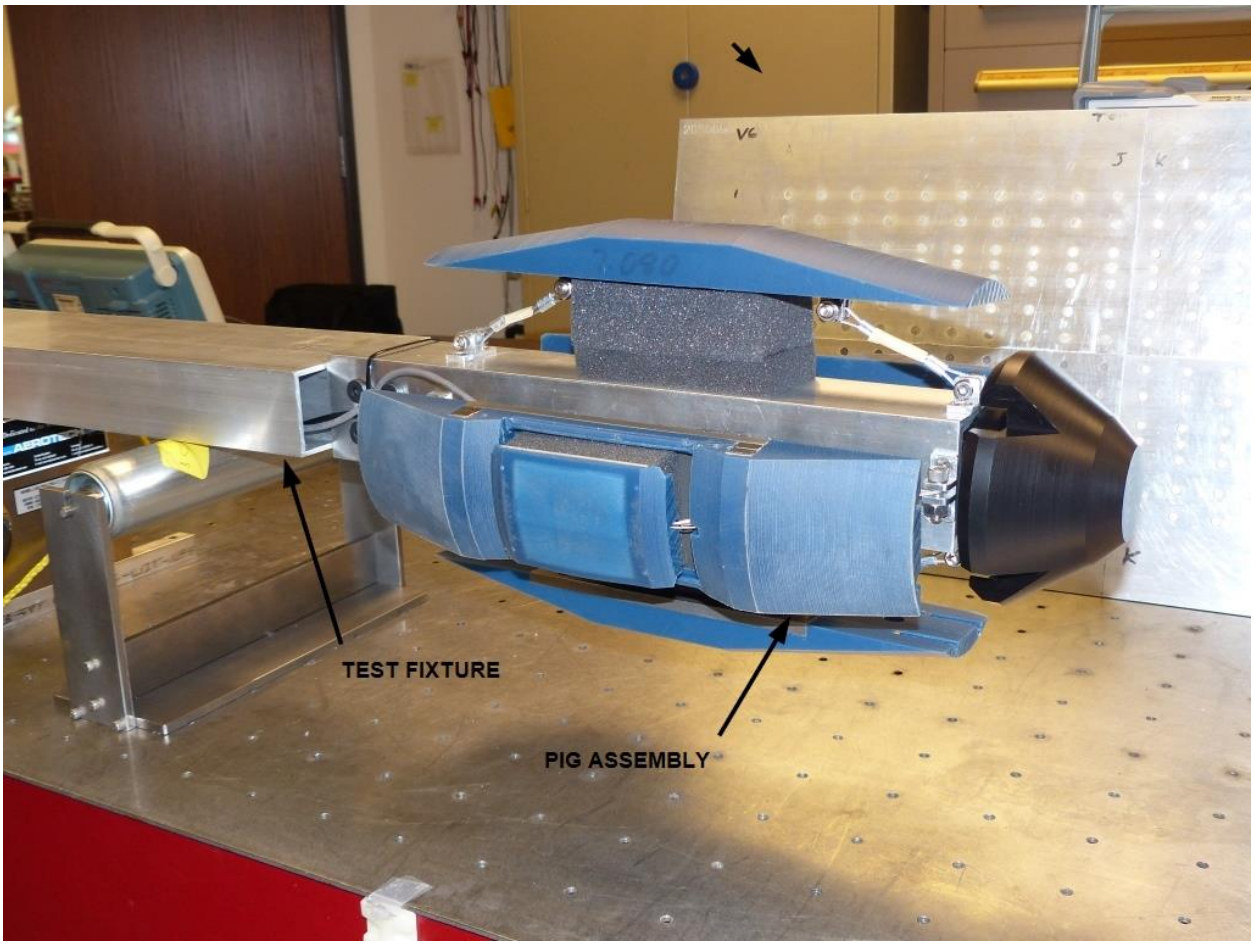

Figure 58. Pig Assembly on Test Fixture

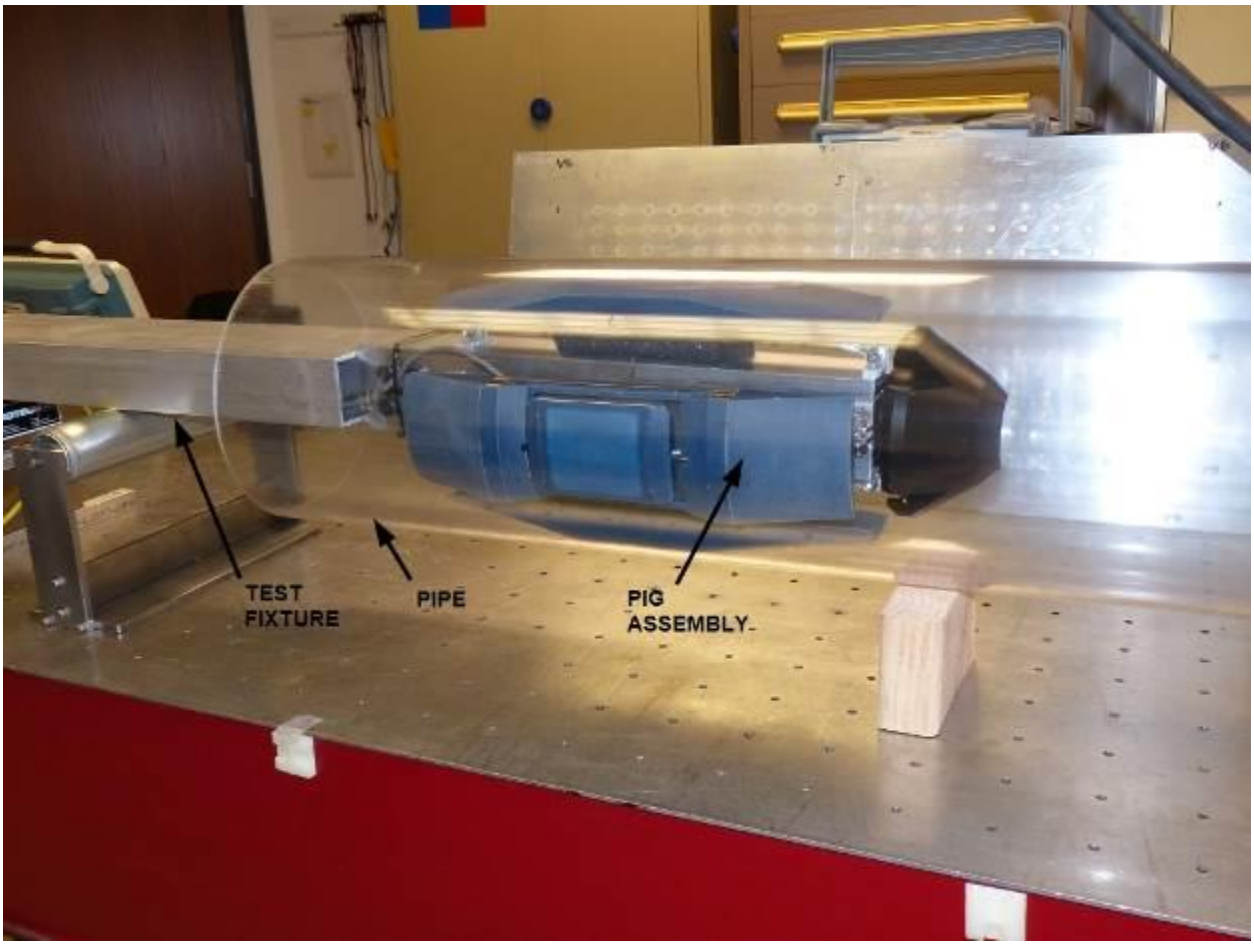

Figure 59. Pig

6. Prototype Testing

This section summarizes the laboratory testing results of the bench-scale EMAT sensor.

The first portion of the section describes the test setup that was constructed for the testing. The next portion describes the initial testing results to demonstrate basic sensitivity and signal-to-noise ratio. This is followed by a piece that describes testing and processing modifications to demonstrate crack depth sizing capability. The final piece discusses the wear testing results.

Overview of Test Set Up

The laboratory test setup shown in Figure 60 was configured using an existing QUEST linear motion stage and commercially available Ritec power amplifier and ultrasonic receiver. The Ritec gated power amplifier will deliver up to 5kw into a 50 ohm load. The Ritec receiver provides adjustable gain up to 64 dB and has adjustable high and low pass filters which are used to limit the frequency response for specific applications. The adjustability of the filters in the Ritec are limited, so a custom bandpass filter module was designed and built for the specific range of frequencies required for this project. A commercially available preamplifier with gain setting of 20, 30, and 40 dB was purchased. It was later found to be too noisy for this application, so a low-noise preamp was designed and built.

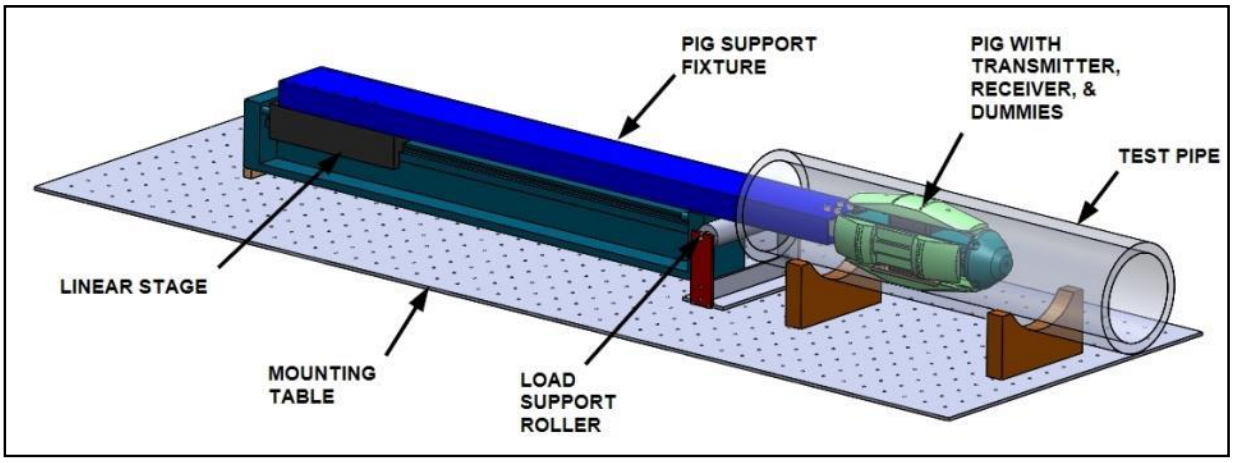

Figure 60. Laboratory Test Setup with the Bench Scale Prototype Attached

To assist with data acquisition and wear testing, a linear motor stage was integrated with the sensing module. The linear stage has a 28 inch stroke and has enough translation force to push and pull the sensor module at sufficient speeds. MATLAB/LabVIEW software was developed to synchronize motion control, data acquisition, processing, display, and data storage; as well as integrate a digital oscilloscope to digitize data from the Ritec receiver via a USB port.

In addition to the bench scale prototype for 8 inch pipe, an additional EMAT transmitter and receiver was designed and fabricated to test on flat and slightly curved plates such as large radii pipe samples.

Figure 61 shows the laboratory test setup with the prototype inserted in one of the test pipes. Figure 62 shows the flat plate sensor attached. This setup was used to generate test scans over the various flaws for further data analysis.

The custom MATLAB software also includes the capability to replay a sequence, and generate video clips of the processed results computer display. This provides a very effective method to visualize the flaws and the various acoustic propagation modes. The videos were presented during the September project review meeting for viewing by the group; they could not be embedded in this report.

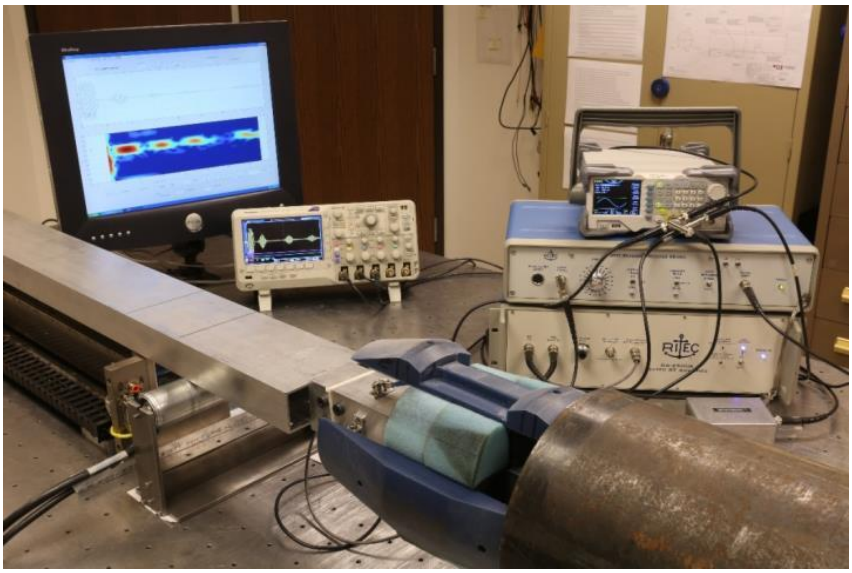

Figure 61. Laboratory Setup with the Bench Scale Prototype Inserted in a Pipe Sample

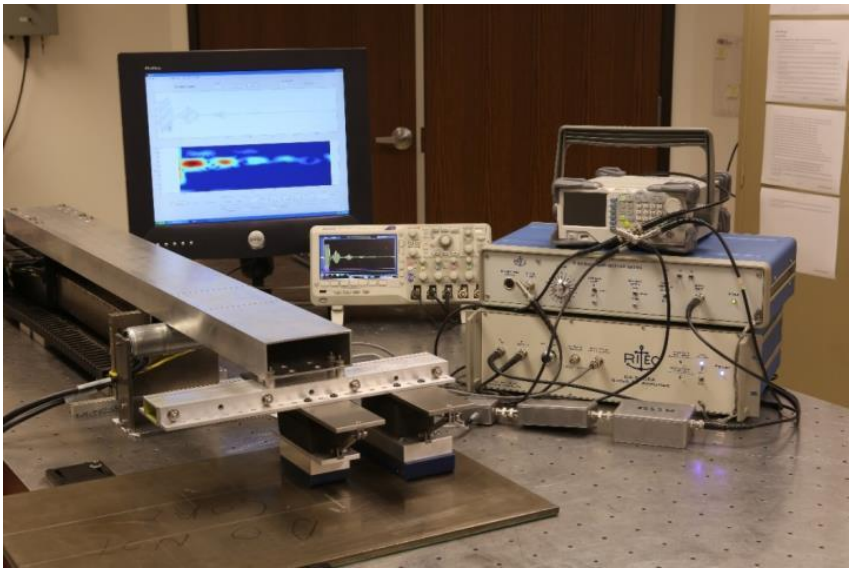

Figure 62. Laboratory Setup with the Flat Plate Sensors Mounted

Sensitivity Testing and Demonstration

Sample preparation

Six, 9.0 mm thick flat plate samples were ordered. This thickness was chosen because it is near the nominal pipe wall thickness. The edges of the samples were machined flat so that acoustic reflections (which would not be present in the pipe) from the edges had minimal distortion and presented the least confusing results. The samples were sized so the distances between the machined flaws and sensors would be similar to those found in 8 inch pipe.

The plates were sent to a vendor and 2 inch long EDM notches were machined in the samples. Three of the plates had 0.5 mm and 2.0 mm deep notches and 3 of the plates had 2.5, 4.0 and 4.5 mm deep notches. The specification on the notch depth was better than +/- 0.1 mm. We were also told that it is difficult to get the notch depth incorrect, however after much testing we decided that the responses didn't look correct so we performed some crude measurements using brass shims and pins. The results are shown in Table 9. It should be noted that we could not measure the notch depths on the two plates that had coating over the notches.

Table 9. As-built EDM Notch Depths in Millimeters for the Plate Samples

	Bare Plates		Coated Plates (ID side)
As specified	Measured using shim	Measured using pin	Measured using pin
0.51	0.48	0.38	0.64
2.01	1.37	1.27	2.13
2.49	1.45	1.40	2.51
3.99	2.29	2.39	3.23
4.52	2.87	2.84	4.32

The depth estimates obtained for bare plates between using shims and pins were pretty consistent so only pin measurements were made on the two coated plate samples. For the bare plates, all of the flaws are undersized. Ideally these would need to get sent out for phased array testing as a confirmation and possibly a gauge house to perform an independent measurement. This emphasizes that on the next phase, more time and money needs to be allocated to sample preparation and independent testing.

A number of vendors were contacted to determine who could properly deposit a 0.5 mm fusion bonded epoxy (FBE) coating on the surface. None were found locally so the plates had to be shipped. To represent both ID cracks and OD cracks, one plate pair was coated on the opposite side of the EDM notches and one plate pair was coated on the EDM notched side. The third pair was left uncoated. As later testing will demonstrate, the coating process was very poor, both in the quality of the deposition and thickness variation. Because of concerns regarding the coating, a thickness gauge was borrowed and each plate was scanned using a 2x2 inch grid pattern. The actual coating across all plates varied from 0.94 to 1.83 mm, almost a 1 mm variation. Within a given plate, the thickness varied as much as 0.7 mm. All of the readings were thicker than the 0.5 mm requested. In retrospect, this is not too surprising since the only available method is hand spraying. We had discussed with the vendor the need for uniformity and they did the best

they could. Attempting to obtain manually coated pipe samples was out of the question as hand coated pipe samples would have been even worse. This points to the need for coating samples that represent what would be provided by the pipeline coating vendors. Since these are automatically applied, the coating should be much more uniform in thickness and quality. Others have noted that it is likely within +/-10%. Coated samples from the pipe suppliers would be much more difficult and time-consuming to obtain as the samples would likely only be available during specific production runs. This would have to be done during the next phase.

In addition to the plates, two pairs of pipe samples were fabricated. One set was seamless and the other set had a weld. Two inch long EDM notches were machined, one pipe had 0.5, 1.0, and 2.0 mm deep notches and the other had 2.5, 4.0 and 4.5 mm notches machined. The IDs of the pipes were slightly different. The seamless samples matched the design ID for the sensor and the seamed samples had a different ID which means the radii didn't match. Because of the apparent EDM notch depth errors noted with the flat plates, brass shims were used to estimate the notch depths. This is more difficult because the EDM notches were near the center of the pipe samples. Table 10 provides a comparison of the specified and as-built for the seamed and seamless pipe samples. These were measured by inserting a thin brass shim and bending it. This is crude, but the results were consistent with the pins when the flat plates were measured. Pins were not possible because of the notch locations within the pipe ID.

Table 10. As-built EDM Notch Depths in Millimeters for the Pipe Samples Measured Using Brass Shims

As specified	Seamed pipe	Seamless pipe
0.51	1.47	0.72
1.02	1.65	1.45
2.01	2.39	2.84
2.49	3.12	3.47
3.99	4.13	4.84
4.52	4.42	5.78

QUEST had a stress corrosion cracked (SCC) pipe sample which was scanned as well. Although an area of slight corrosion can be seen in the OD surface, the tight cracks are not visible. QUEST develops and produces an eddy current imaging system that is based on magneto-optic imaging (MOI) technology. This equipment was used to detect the extent of the cracking. The MOI doesn't measure the depth but is a very convenient method to detect the location of the SCC.

Sensitivity results

The following sections provide the results of the sensitivity testing for the coated/uncoated plates, the pipe sections and the natural flaw sample. The results clearly show the ability to detect 0.5 mm notches in the presence of interfering modes in uncoated samples as well as samples where the notches are opposite the coating, and under the coating. Only selected images are shown. Videos of the samples were generated by scanning across the plates or through the pipe samples and show both the time domain response stacked with the computed short time

Fourier transform results. The videos, which were shown at the design review meeting, provide a much better flaw response visualization as the EMAT sensors scan across the flaws. Unfortunately the videos cannot be practically embedded into this report, so static images are provided. The flat plate scanning geometry is illustrated in Figure 63.

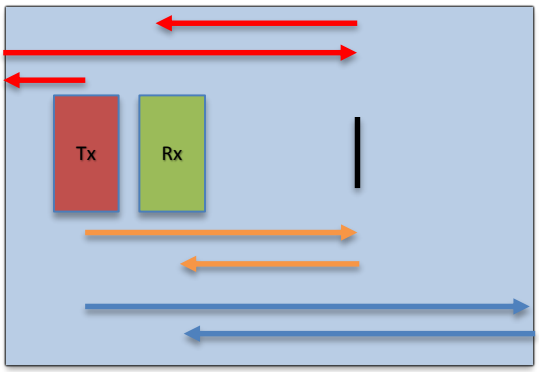

Figure 63. Flat Plate Scanning Geometry

To understand the resulting plots, the plate scanning geometry must be described:

- The blue field in Figure 63 represents a horizontal slice of the test plate.
- The box labeled Tx represents the EMAT transmitter and the box labeled Rx represents the EMAT receiver.
- The transmitter emits a beam of energy horizontally in both directions, approximately 2 inches in vertical width under the transmitter and subsequently under the receiver.
- The red arrows show the energy traveling to the left that reflects from edge of the plate back under the receiver, reflecting from the crack and back to the receiver.
- The orange arrows show the energy travelling to the right, going directly under the receiver, a portion of which reflects off of the crack and then back to the receiver.
- The blue arrows represent that portion of energy transmitted to the right that goes past the crack, reflects off of the right edge of the plate and back to the receiver. Those components can all be seen in the plots that follow.
- The videos were constructed by collecting data as the linear motion stage moves the transmitter and receiver as a pair across the plate orthogonal to the acoustic beam direction.

Figure 64 shows the typical display output. The time domain response is shown on the bottom, and the short time Fourier transform (STFT) response is on top. The identity of the larger time domain signals are also shown.

The STFT plot has time on the horizontal axis and frequency in the vertical axis and is used to show the mode content. Different modes propagate at different velocities so they will not stay in the same relative time positions. The “clouds” of information are labeled with the specific guided wave propagation modes that were determined from the dispersion curves.

This process was discussed during the project review meeting. This particular plot was generated earlier in the testing phase with the excitation signal operating at the SH1 frequency. Note the variety of modes excited. The modes of interest in this case are the two encircled areas and labeled flaw. The one on the left is the 0.5 mm flaw reflection from the directly transmitted signal (the orange arrows in Figure 63) and the one on the right is the flaw reflection from the signal transmitted to the left and reflected off the edge of the plate (the red arrows in Figure 63). Note the interfering mode, SH2, which occurs almost directly over the left side flaw response. Frequency filtering separates the useful flaw signal from the slower SH2 signal.

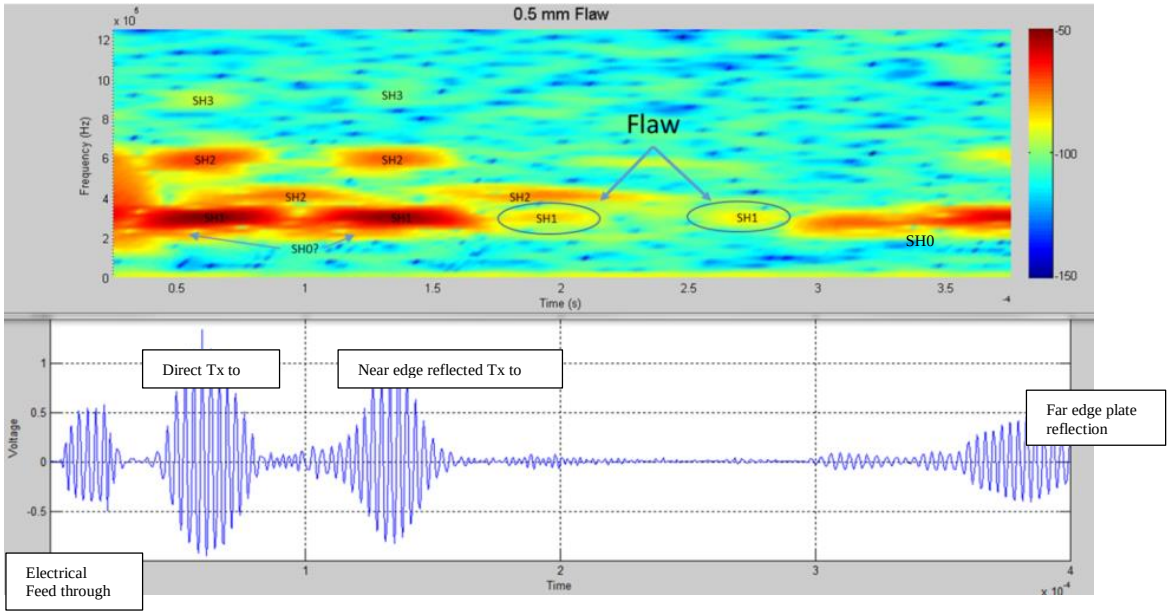

Figure 64. MATLAB Software Output Display Example Showing the Short Time Fourier Transform Response Stacked on Top of the Time Domain Response

Figure 65 to Figure 67 are uncoated flat plate responses from scans taken from the videos for 0.5, 2.0 and 4.0 mm deep EDM notches. The left side of the figures are screen shots when the scan is over a clear area of the plate, and the scans on the right side of the image are when the scan is over the notched section. The upper pair is when the notch is on the same side as the sensors (ID like flaw) and the lower pair is when the notch is on the opposite side as the sensor (OD like flaw). Red boxes show the area of interest. Note that for Figure 8 (4.0 mm notches) there is some residual energy in the "no flaw" scan. Due to the construction of the plates, the areas with no flaws are quite close to flaws, so there is some side lobe energy from the transmitter striking the flaw.

Figure 68 to Figure 70 are essentially the same but with the coating as described earlier in this report. For all of the figures, the responses have not been normalized. Normalization is the process where the flaw signal amplitude is divided by the signal directly received from the transmitter. This will be discussed in detail in the Flaw Depth Testing section of this report.

Selected flat plate uncoated:

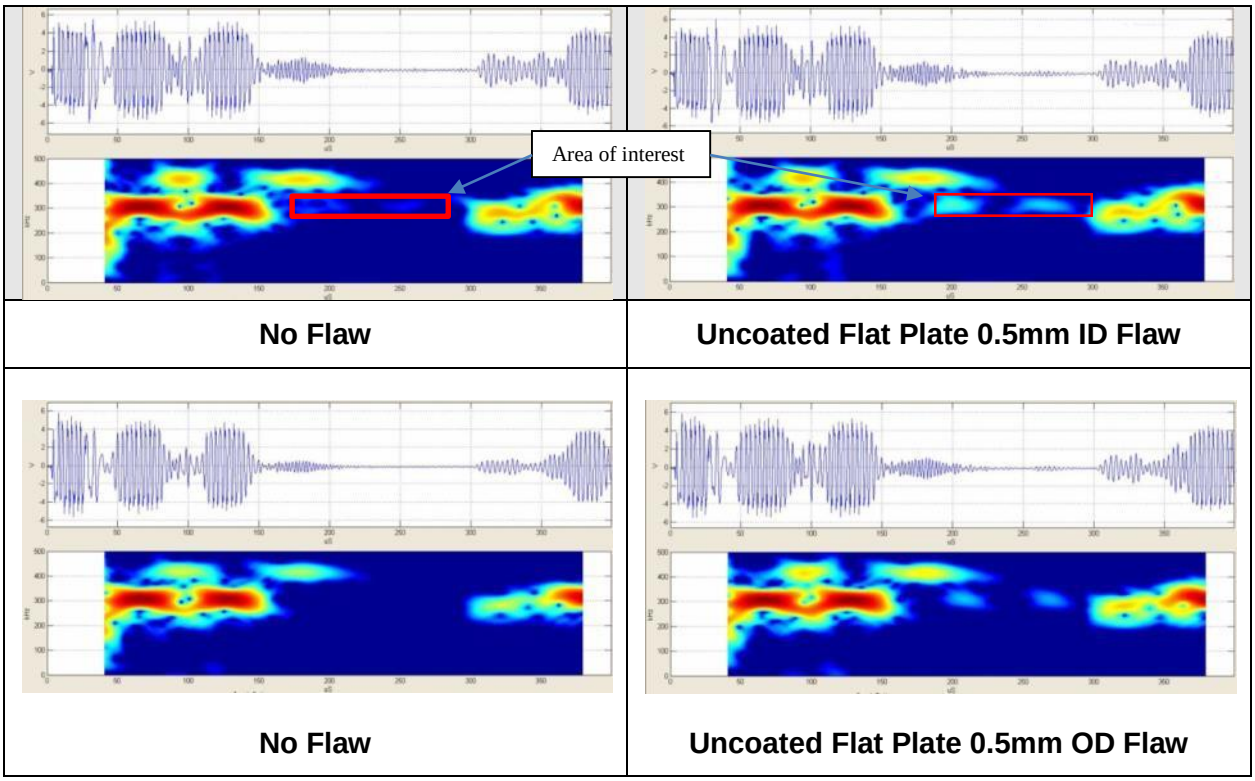

Figure 65. Flaw/No Flaw Comparison for Uncoated 0.5 mm Deep Flaws

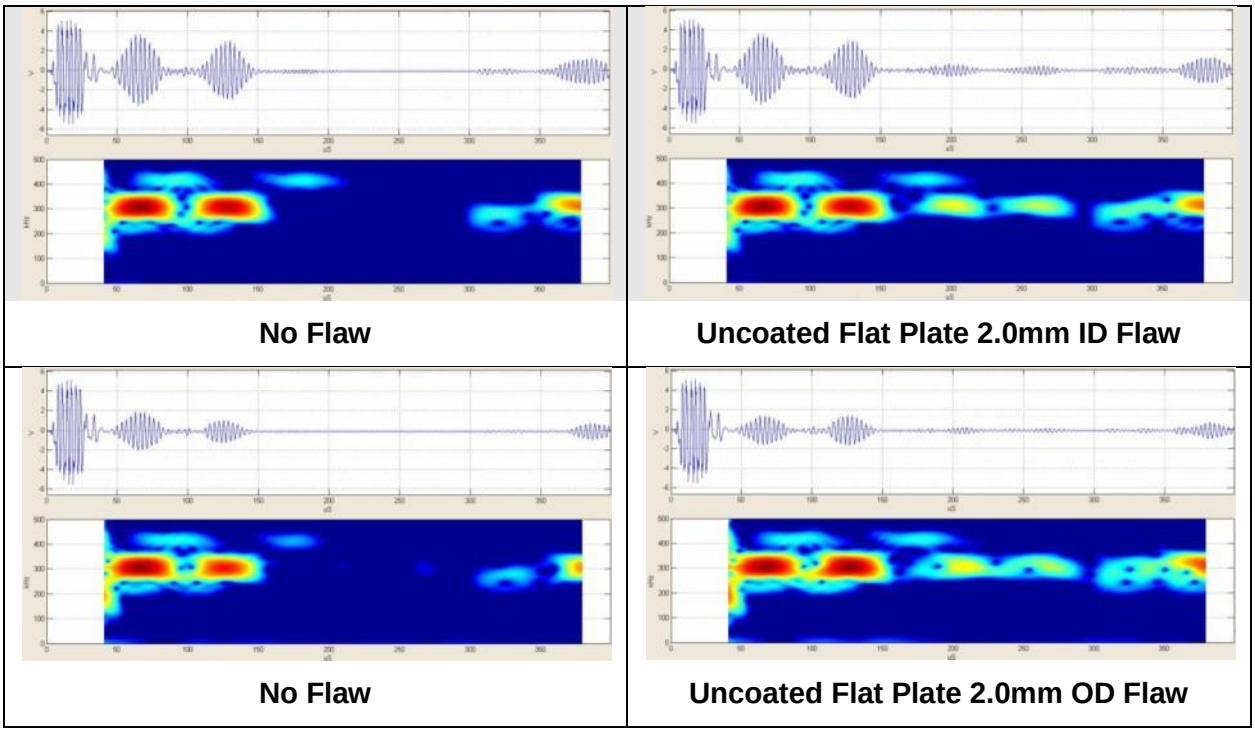

Figure 66. Flaw/No Flaw Comparison for Uncoated 2.0 mm Deep Flaws

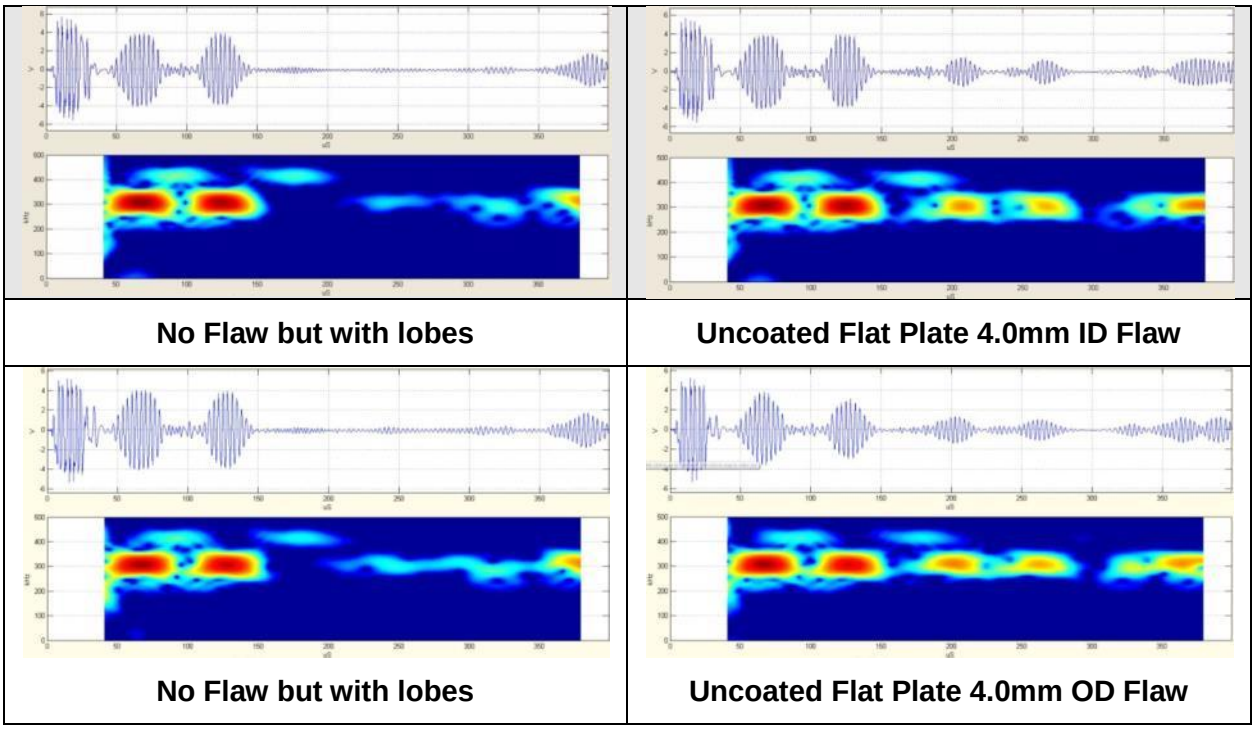

No Flaw but with lobes	Uncoated Flat Plate 4.0mm ID Flaw
No Flaw but with lobes	Uncoated Flat Plate 4.0mm OD Flaw

Figure 67. Flaw/No Flaw Comparison for Uncoated 4.0 mm Deep Flaws

Selected flat plate coated

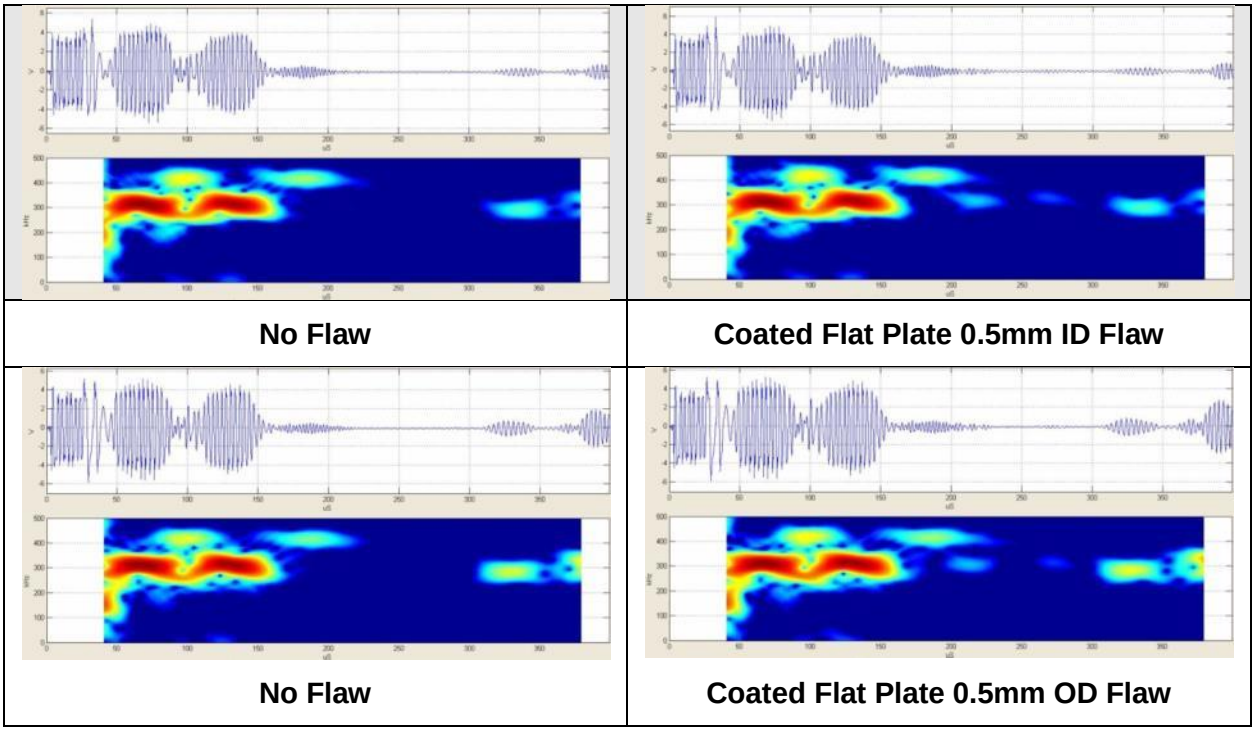

No Flaw	Coated Flat Plate 0.5mm ID Flaw
No Flaw	Coated Flat Plate 0.5mm OD Flaw

Figure 68. Flaw/No Flaw Comparison for Coated 0.5 mm Deep Flaws

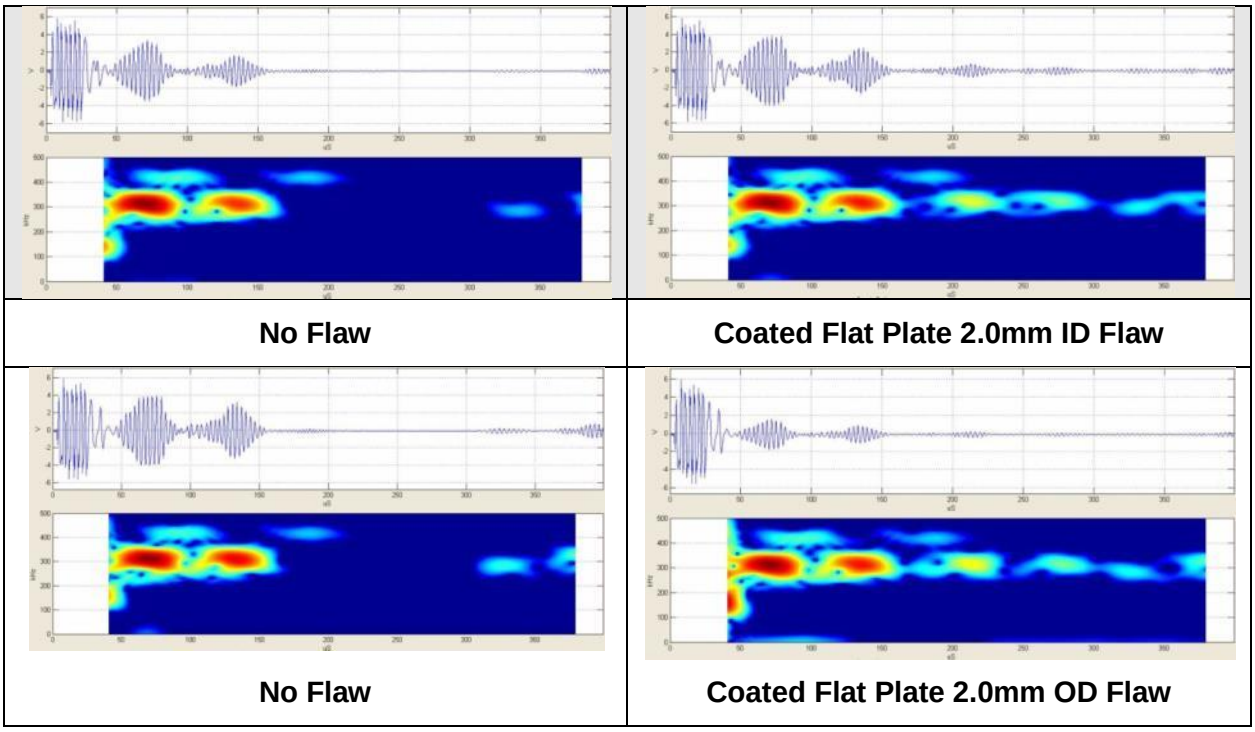

No Flaw	Coated Flat Plate 2.0mm ID Flaw
No Flaw	Coated Flat Plate 2.0mm OD Flaw

Figure 69. Flaw/No Flaw Comparison for Coated 2.0 mm Deep Flaws

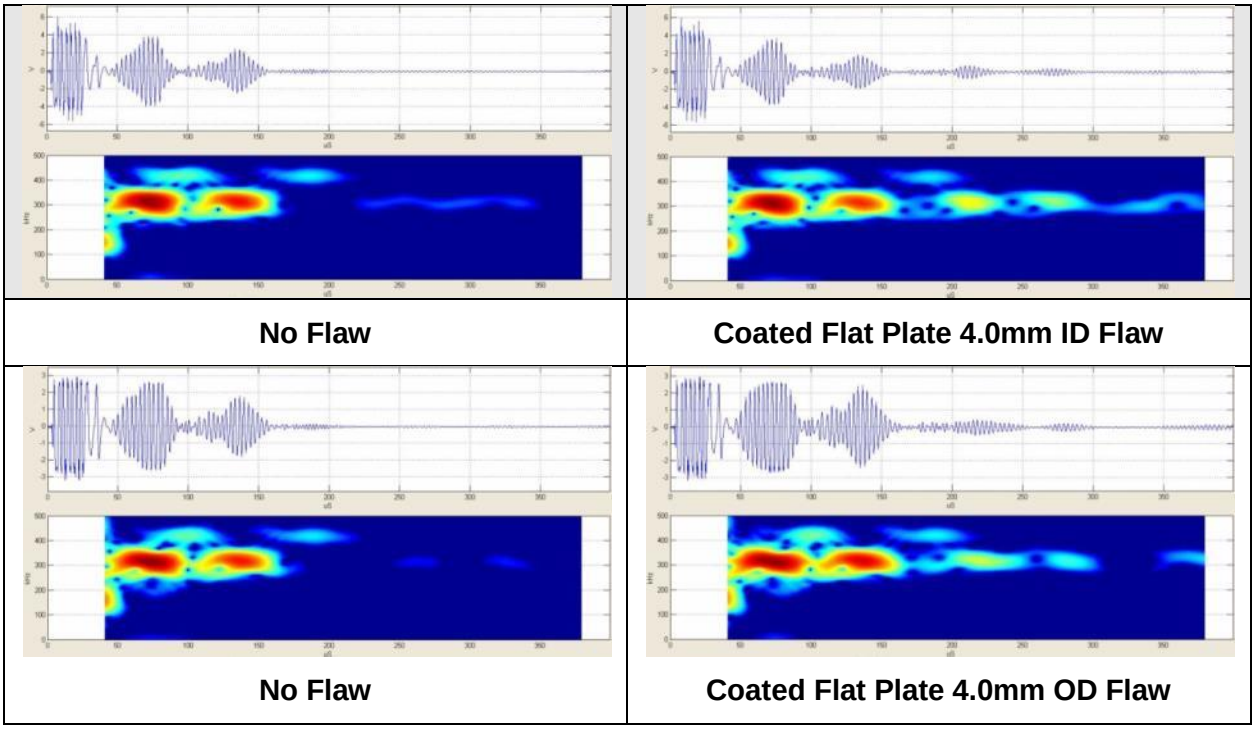

No Flaw	Coated Flat Plate 4.0mm ID Flaw
No Flaw	Coated Flat Plate 4.0mm OD Flaw

Figure 70. Flaw/No Flaw Comparison for Coated 4.0 mm Deep Flaws

Natural flaw sample

QUEST has a stress corroded sample that had been removed from a large diameter pipe that had stress corrosion cracking. There is evidence of corrosion, however the crack itself is not visible as it is apparently a very tight crack. A photograph of the overall sample is shown in Figure 71.

Figure 71. SCC Pipe Sample – OD View

A close up view of the crack location is shown in Figure 72. The irregular black line in the figure is the area where the MOI detected the crack. The overall length of the crack is approximately 120 mm in the axial direction. The yellow rectangle represents the approximate axial length of the receiver. At this time the depth of the crack is unknown as QUEST does not own phased array UT equipment to estimate the depth.

Figure 72. SCC Sample with the Approximate Crack Location Noted – OD View

The SCC sample was scanned with the laboratory setup and a video was produced. The scan was taken with the EMAT sensors positioned on the ID surface. Figure 73 is the no-crack response from the sample. Figure 74 and Figure 75 are when the sensor pair is halfway on and then halfway off the ends of the crack. Figure 76 is when the sensor is in the middle of the crack. The EMAT transmitter and receiver transducers were positioned between the crack and the edge of the sample as shown in Figure 63. The crack response is quite strong.

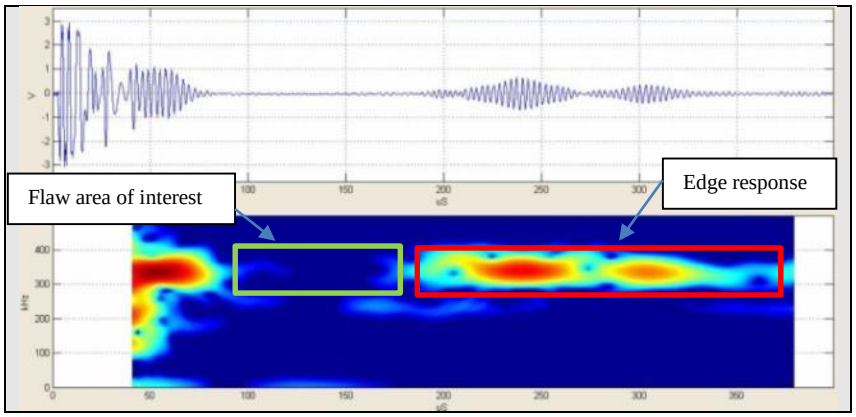

Figure 73. No-Crack EMAT Response

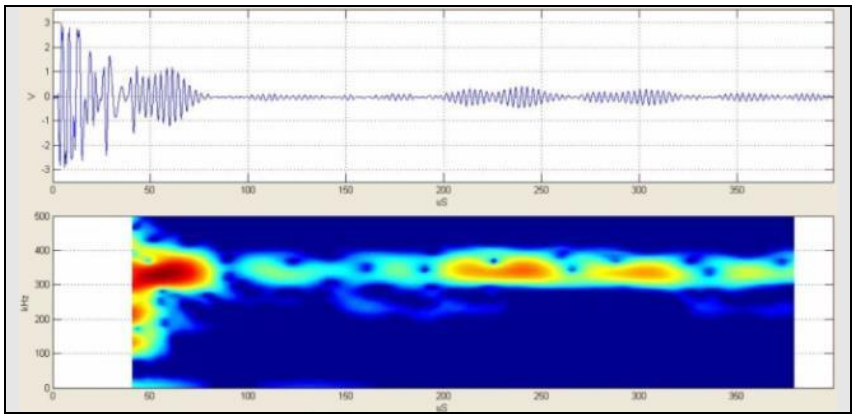

Figure 74. EMAT Response Halfway on the Crack

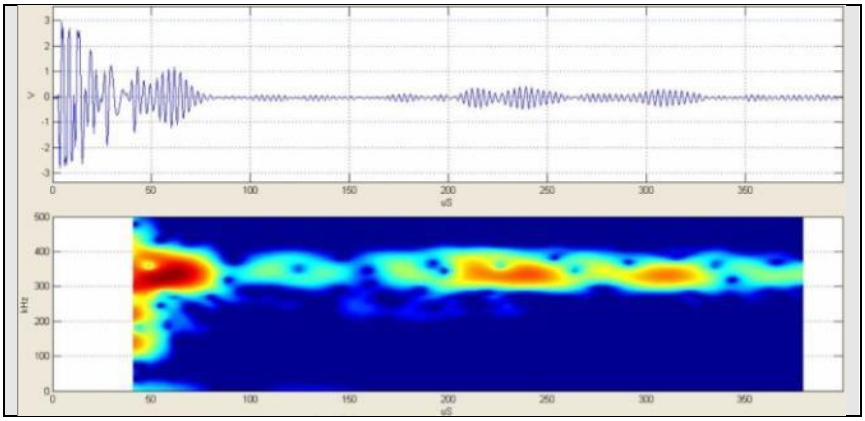

Figure 75. EMAT Response Halfway off the Crack

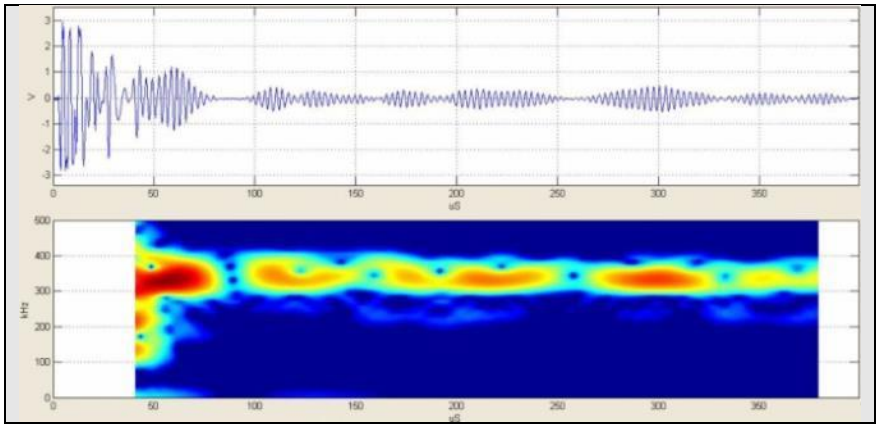

Figure 76. EMAT Response from the Middle of the Crack

Uncoated pipe scans

In a similar manner, the pipes were scanned simply by using the linear motion stage to push or pull the EMAT bench scale prototype through the pipe sample. Figure 77 is from a seamed pipe sample without flaws. Features of the scan are illustrated in the figure. Note that the interfering modes propagate at different group velocities and are at a different frequency. The reflection from the seam is weak but present. The fact that it is a seam was confirmed by rotating the bench-scale prototype relative to the pipe.

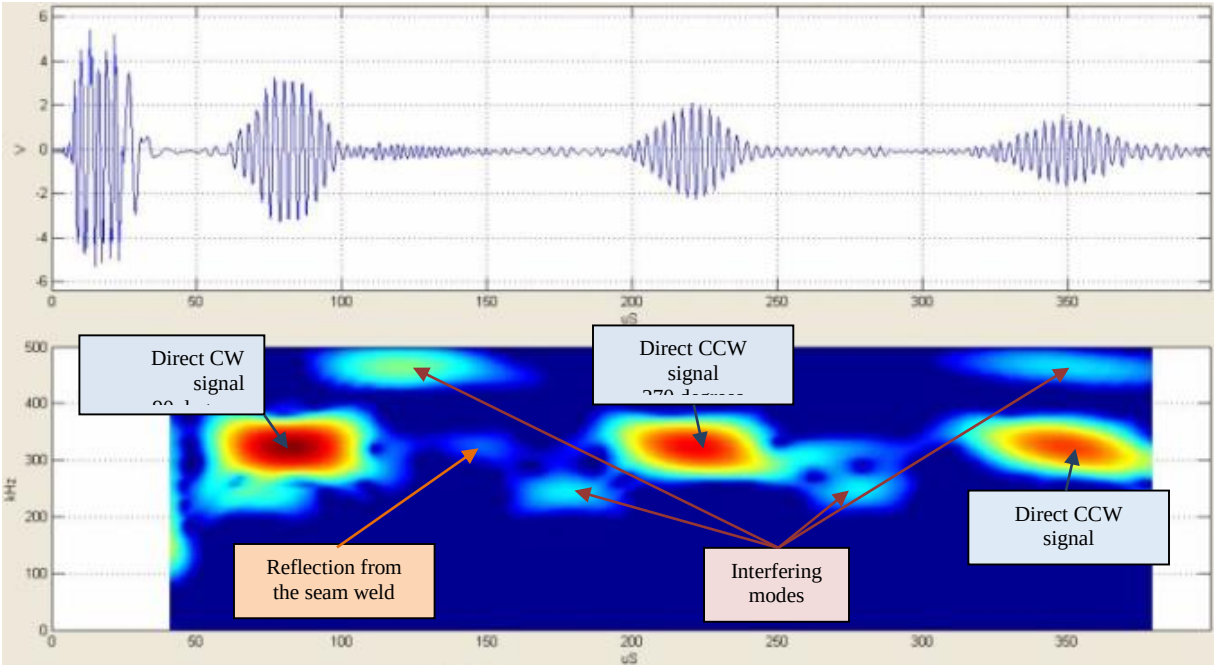

Figure 77. Seamed Pipe Test Scan Illustrating the Structure of the Response

Figure 78 to Figure 81 are the EMAT sensor responses to 0.5, 1.0, 2.0 and 4.0 mm deep EDM notches. The no flaw response is shown on the left of the figure and the flaw response is on the right. Only ID EDM notches were created on the test pipes. Please note that the depths listed in the figures are the specified notch depths. A better estimate of the actual notch depths is provided in Table 10.

Seamed pipe samples

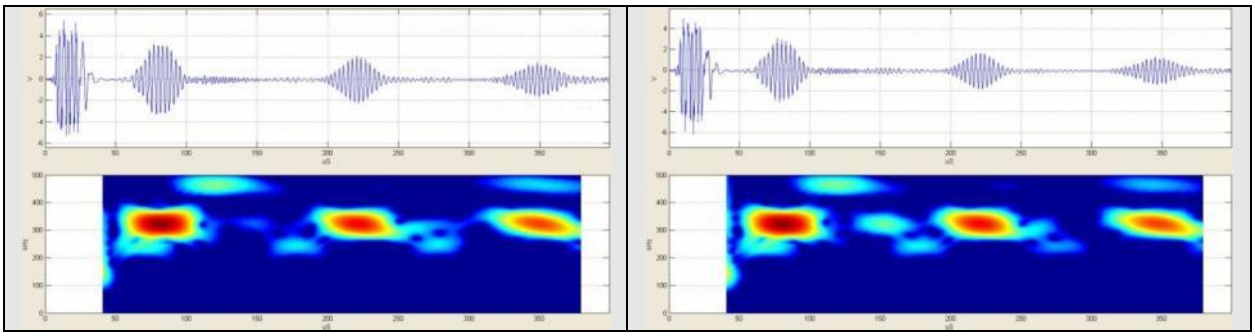

Figure 78. No Flaw on the Left, 0.5 mm ID Flaw on the Right

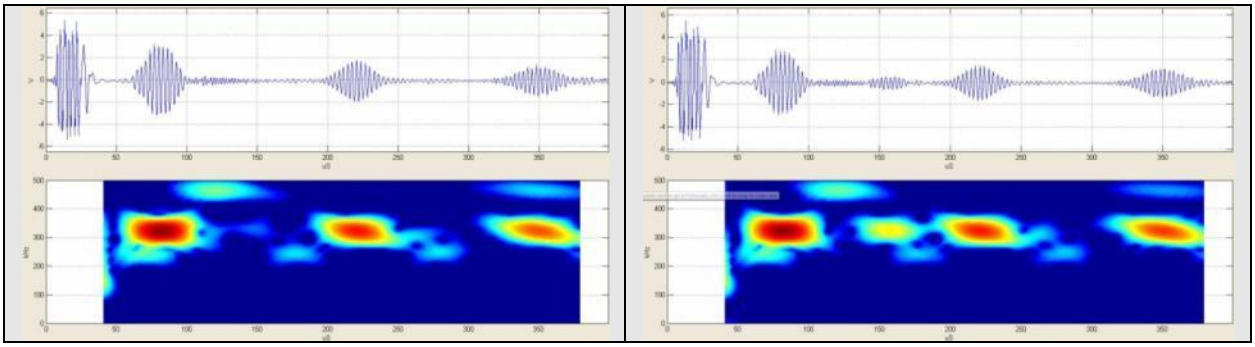

Figure 79. No Flaw on the Left, 1.0 mm ID Flaw on the Right

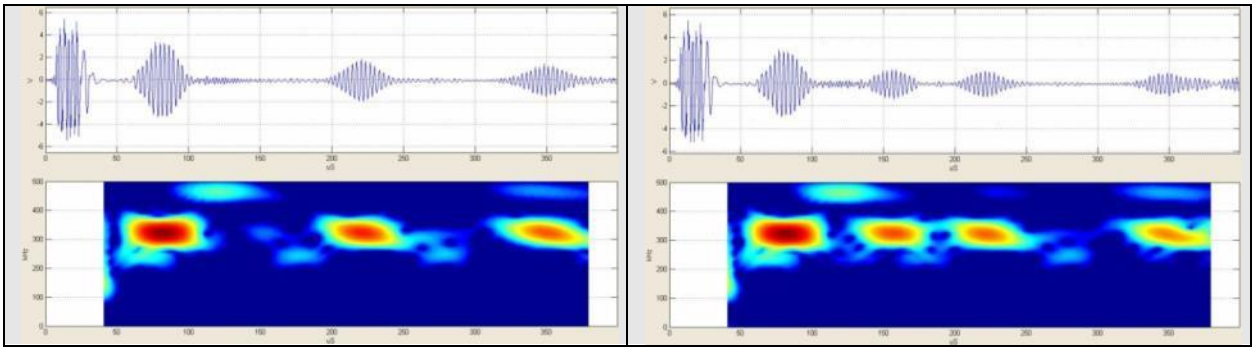

Figure 80. No Flaw on the Left, 2.0 mm ID Flaw on the Right

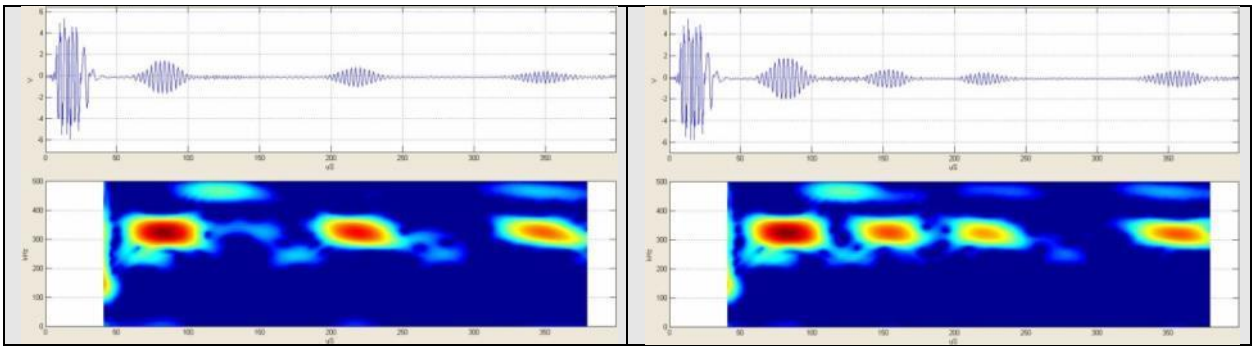

Figure 81. No Flaw on the Left, 4.0 mm ID Flaw on the Right

Seamless pipe samples

Figure 82 to Figure 85 are the EMAT sensor responses to 0.5, 1.0, 2.0 and 4.0 mm deep EDM notches from the two seamless pipe samples. Please note that the depths listed in the figures are the specified notch depths. A better estimate of the actual notch depths is provided in Table 10. The structure of the images are the same format as shown in Figure 77, however note there is no reflection from the seam and the interfering modes are larger before the 270 degree CCW signal. There is also some energy at the mode frequency of interest. The larger interfering mode is due to the thicker walls (11.9 mm) in this sample as compared to the seamed pipe sample. As the wall thickness increases, more wave modes are present in the wall.

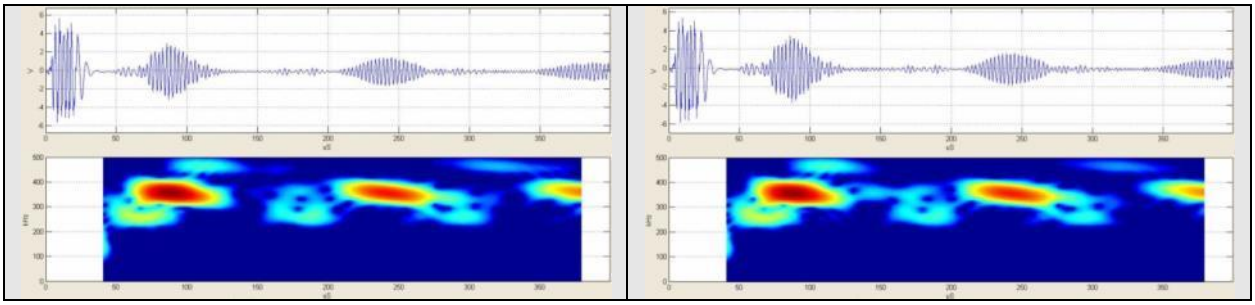

Figure 82. No Flaw on the Left, 0.5 mm ID Flaw on the Right

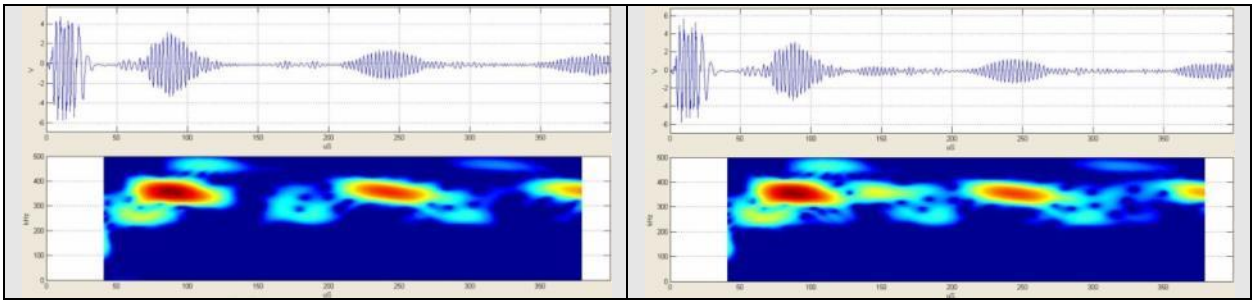

Figure 83. No Flaw on the left, 1.0 mm ID Flaw on the Right

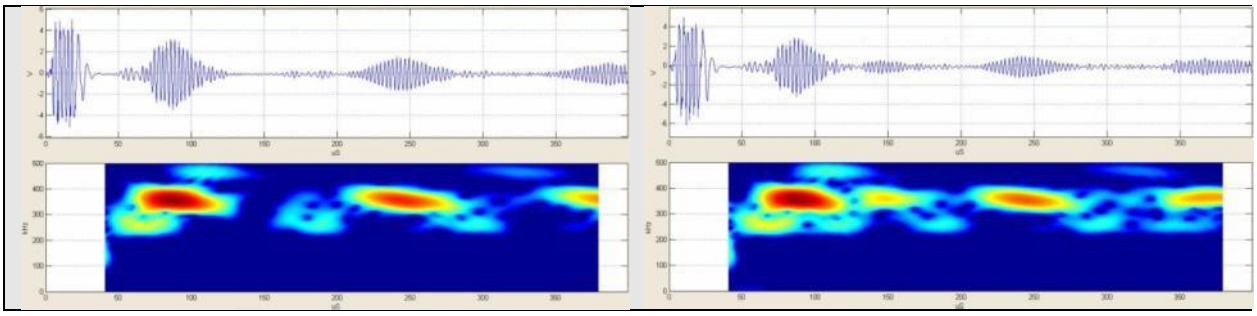

Figure 84. No Flaw on the Left, 2.0 mm ID Flaw on the Right

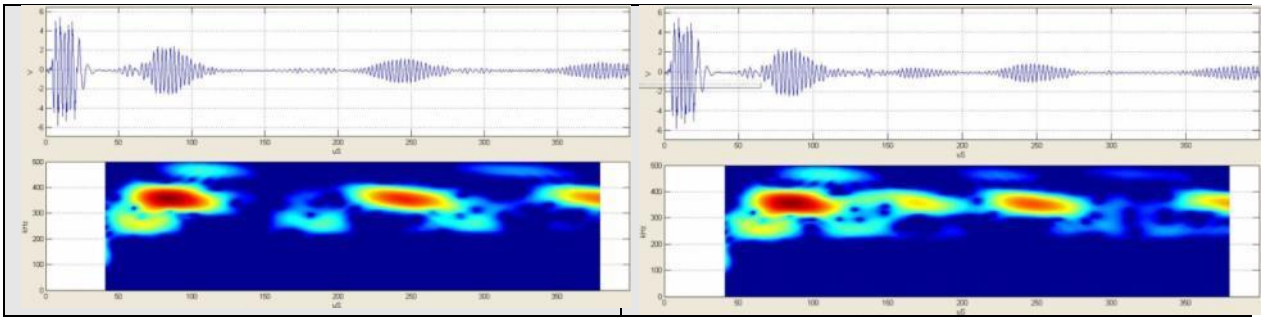

Figure 85. No Flaw on the Left, 4.0 mm ID Flaw on the Right

Flaw Depth Testing

Initial calibration on plates

At the outset, it must be noted that the EDM notch depths as specified to the vendor were 0.5 mm, 2.0 mm, 2.5 mm, 4.0 mm and 4.5 mm, for both the plate and pipe samples. The pipe samples also had a 1 mm deep notch. However as was discussed in the *Sample Preparation* section of this report, the notch depths as measured in-house varied significantly – underlining the need for accurately manufactured and independently verified depth samples for use in the next project phase. For this section of the report, the notch depths used are the ones listed in Table 9 and Table 10. The initial calibration results are presented using twin horizontal axes, one for notch depth in millimeters and the other in percent wall thickness, to facilitate comparison.

The calibrations of flaw reflections against the measured values of notch depth and percentage wall thickness for bare plates are shown in Figure 86 and Figure 87 for the cases corresponding to same-side flaw-sensor and opposite side flaw-sensor configurations. It may be noted that the linear trends correspond to the results from FEA simulations.

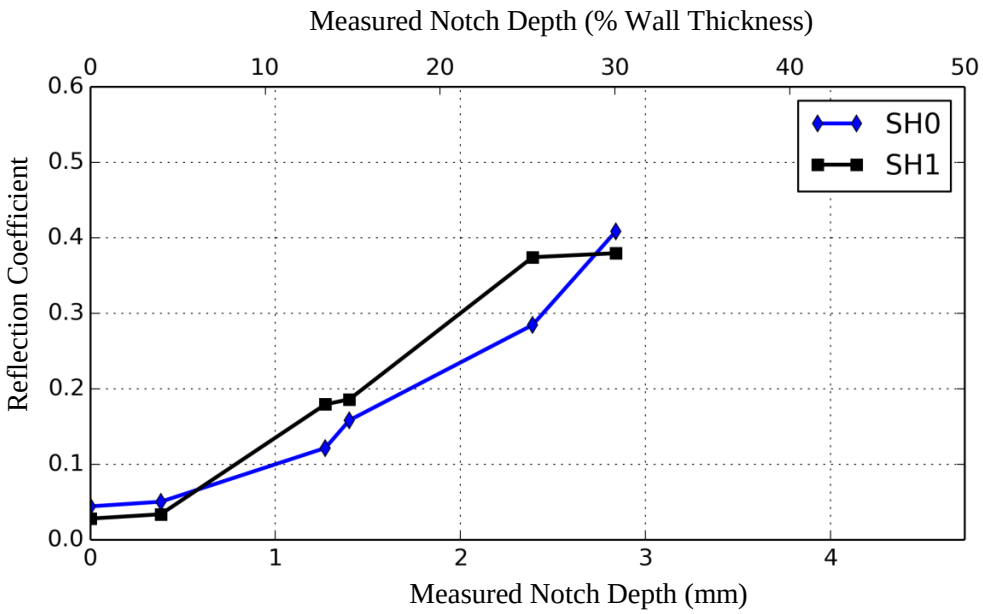

Figure 86. Reflection Coefficient vs. Notch Depth for a Bare Plate when EMATs and Notches are on the Same Side of the Plate

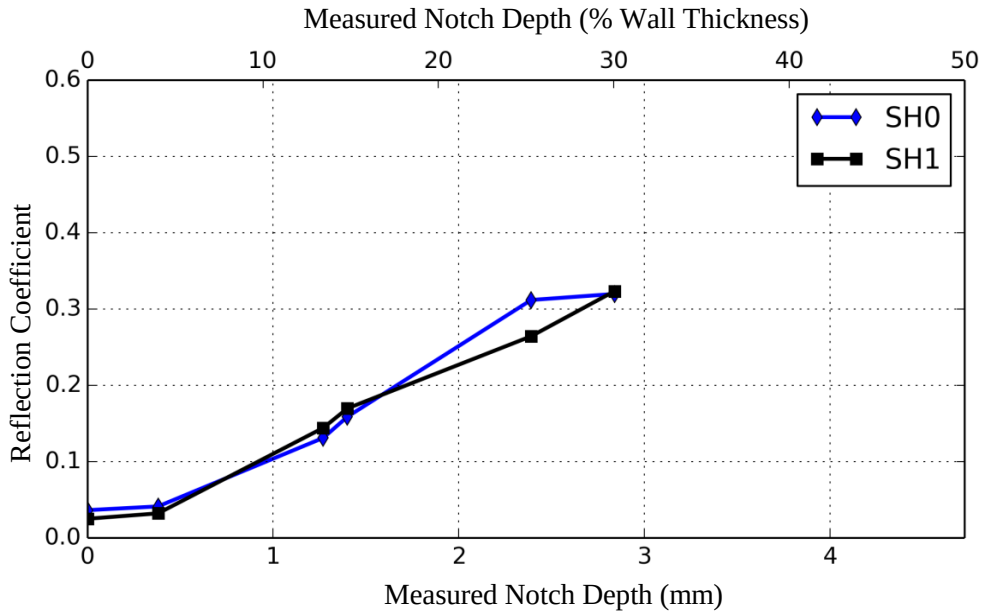

Figure 87. Reflection Coefficients vs. Notch Depth for a Bare Plate when EMATs and Notches are Located on the Opposite Sides of the Plate

The reflection coefficients for coated plates (a scenario similar to Figure 86 and Figure 87) are shown in Figure 88 and Figure 89. Note that the reflection coefficients in this case are very different from those for bare plates. Furthermore, the curves do not trend in a monotonous

fashion, which is counter-intuitive, because a larger flaw must reflect more energy under fixed conditions. As noted in the *Sample Preparation* section of this report, there were drastic variations in the characteristics of the coating between and across the samples – underlining the need for coated pipe samples directly from the field or the manufacturer during the next phase.

It was observed earlier from finite element simulations that the presence of the coating drastically reduced the reflection coefficient values. Hence, results like these were not entirely unexpected, given the quality of the samples. More importantly, it was observed during the course of the experiments that the strength of the generated signal also dropped significantly. The reason for this drop in signal strength becomes apparent if the dispersion curves for coated plates of different thicknesses are analyzed.

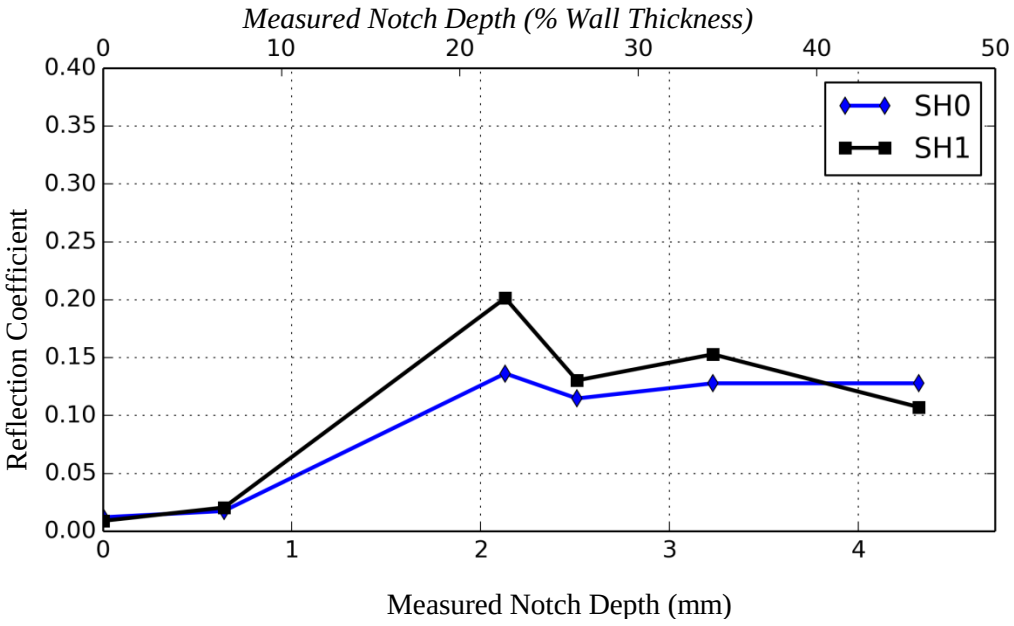

Figure 88. Reflection Coefficients vs Measured Notch Depth for Coated Plate when Notches are on the Bare Side
(EMATs are also mounted on the Bare Side)

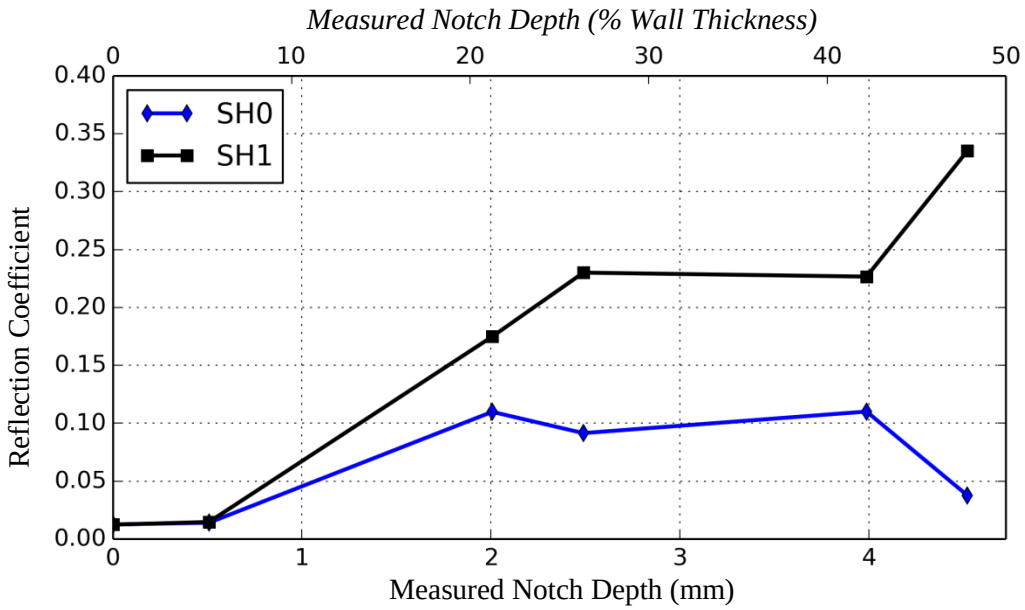

Figure 89. Reflection Coefficients vs Nominal Notch Depth for Coated Plate when Notches are on the Coated Side
(EMATs are mounted on the Bare Side)

3D FEA Simulations

3D FEA simulations using a more efficient open source software collection called FEniCS were completed. Progress of ongoing 3D simulations is demonstrated in Figure 90 to Figure 93. Note that in all these figures, the linear perspective view (objects farther away appear smaller) has been implemented.

The pipe shown in these figures is modeled after the seamless pipe being used for the EMAT-notch-depth sensitivity experiments. Figure 90 shows the original location of the EMAT in the FEA model. The EMAT actuation is modeled as a time varying axial stress distribution. Figure 91 demonstrates that, as anticipated, the bidirectional beams are generated by an EMAT. The beam spread on both the ID and OD is demonstrated in Figure 92 and Figure 93. It may be observed that the beam spread is fairly collimated, i.e., it is centered and narrow in width. As speculated in the experiment results, the narrow width of the beam causes sensitivity of the notch-depth measurements to the relative inclination of the transmitter. Longer and more fine-tuned computations are underway in order to obtain simulated waveform signals for comparison against those obtained by the EMAT bench tests.

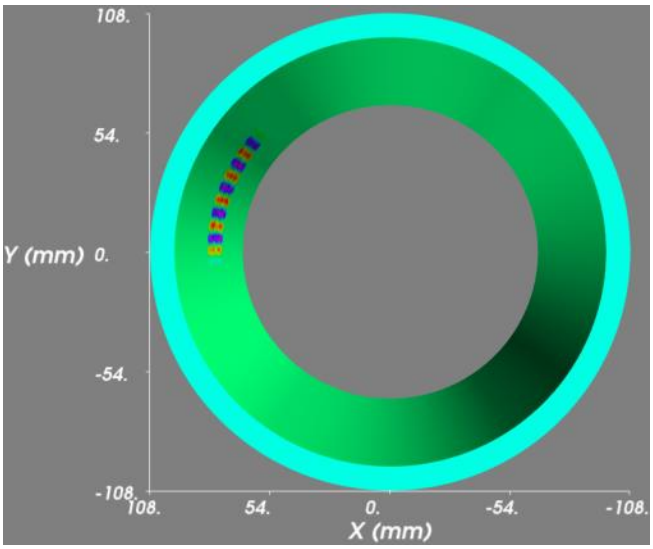

Figure 90. A Perspective Image Showing the Original Location and Shape of the EMAT on the ID of the Pipe when Viewed from the End of the Pipe

Note also from Figure 91 - Figure 93 the lower amplitude side lobe energy as discussed in the Sensitivity Results section of this report.

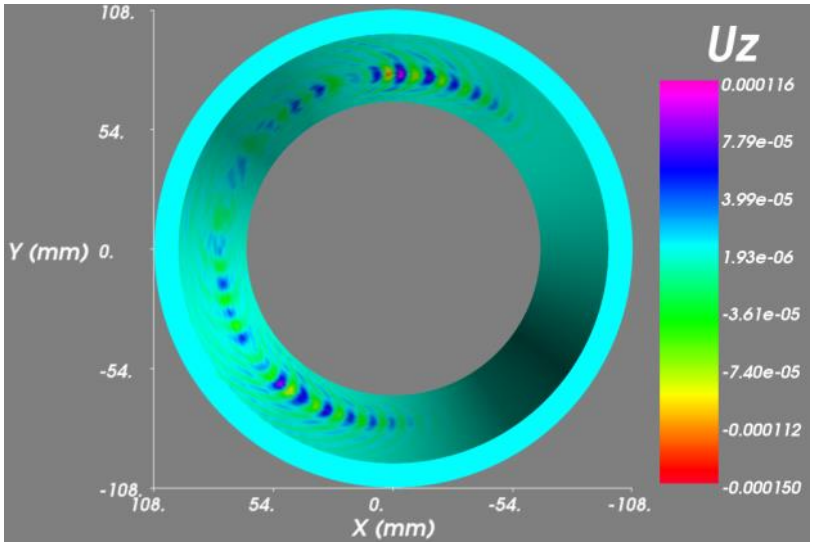

Figure 91. A Perspective Image of the Bidirectional Beams on the ID of the Pipe as Viewed from the End of the Pipe

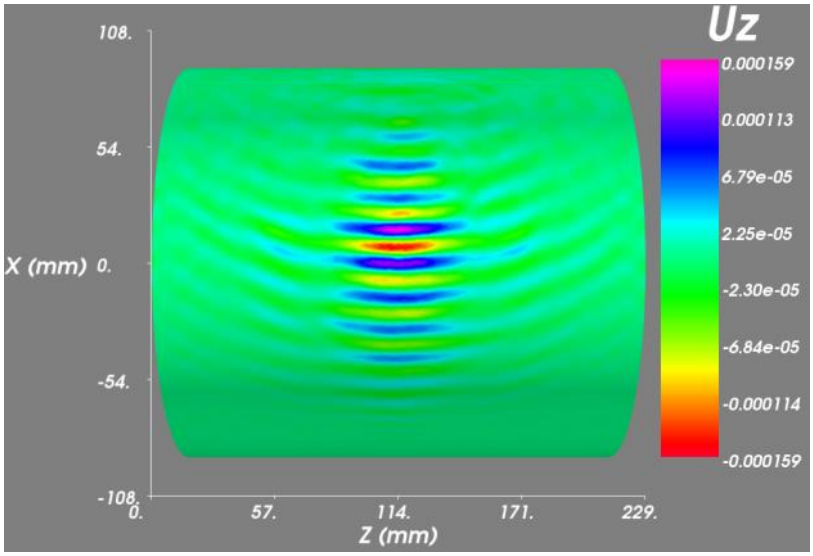

Figure 92. A Perspective Image of the Top View of the Beam Spread on the OD of the Pipe

It may be inferred that the beam is fairly collimated which might be responsible for sensitivity of flaw measurements to angle.

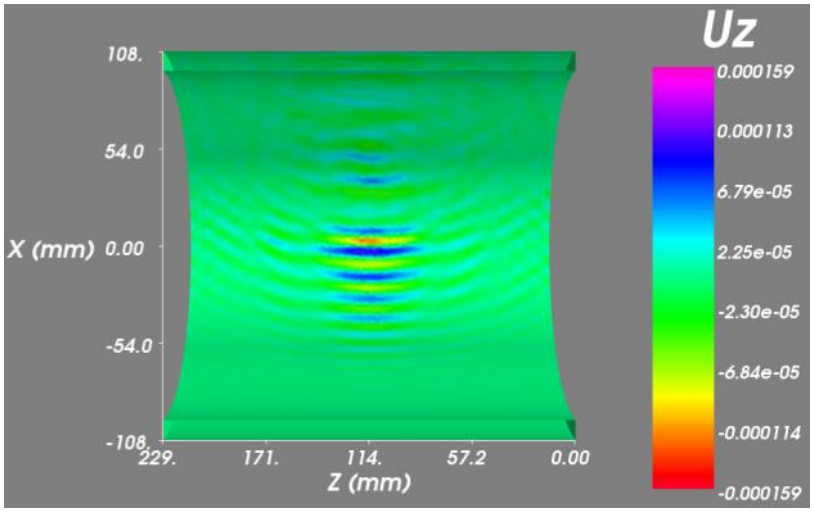

Figure 93. A Perspective Image of the Top View of the Beam Spread on the ID of the Pipe

The relative lack of uniformity of the beam along the circumference indicates presence of multiple modes.

Wear Testing

The purpose of this testing was to determine how well the material selected for fabrication of the EMAT sensor shoes would wear over repeated cycling in the laboratory test setup shown in Figure 61.

The linear motor stage shown in Figure 61 was configured to cycle the bench-scale prototype within one of the two seamed pipe samples. The stroke was set to traverse 1.4 meter (~4.6 feet) during one full cycle. The bench-scale prototype would protrude from the pipe at each end of the cycle however the contact/sensor portion of the EMAT sensors stayed well within the pipe. The linear motor was programmed such that the average speed was 0.35 meters per second (1.15 ft/sec) which includes the acceleration and deceleration times necessary for reversing at each end of the pipe. A 3 mm (0.118") tall weld bead was created 127 mm axially in one end of the pipe such that the sensor would pass over the top of the weld bead when cycling. The weld bead only occupied approximately 100 degrees of the circumference and is shown in Figure 94. This was done so only one of the sensor shoes would pass over the bead and the tool was positioned so the Lorentz dummy shoe was used. We didn't want to destroy one of the actual sensors if the shoe material didn't work as planned.

Figure 94. 3 mm Tall Bead Welded in the Seamed Pipe Sample

The dummy shoe was 29.95 mm (1.179 inches) thick as measured with a set of calipers before testing. The bench scale prototype had been cycled many times during signal testing, however the number of cycles was not recorded. Photographs of the dummy shoe and the sensors are shown in Figure 95 to Figure 97. It is clear that the sensor had been cycled with the laboratory test setup. Note that all surface scratches are quite small because a fingernail scraping across the surface can barely feel the scratches. It is mostly surface roughness variation.

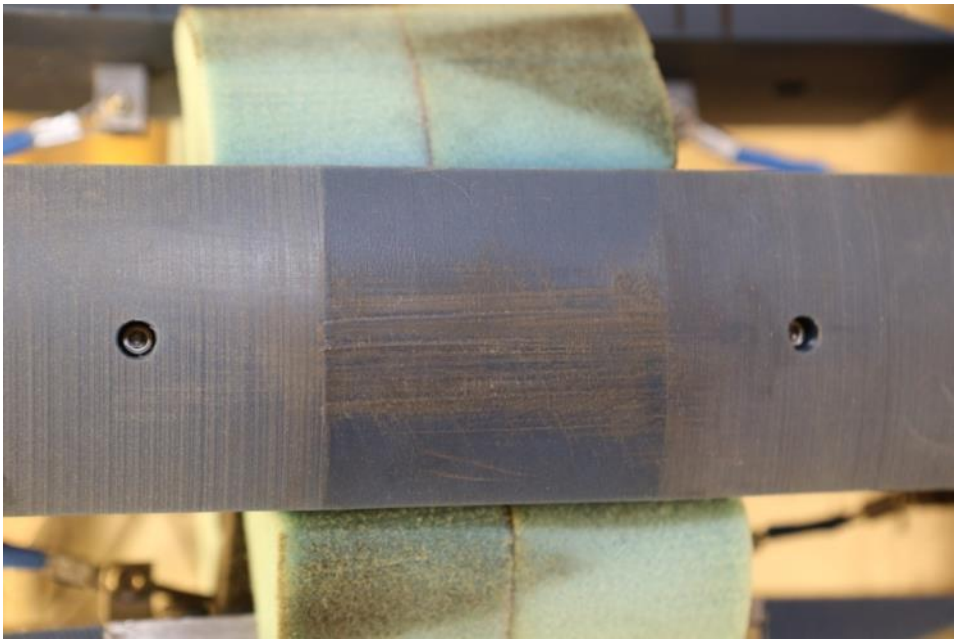

Figure 95. Dummy Shoe before the Cycle Test

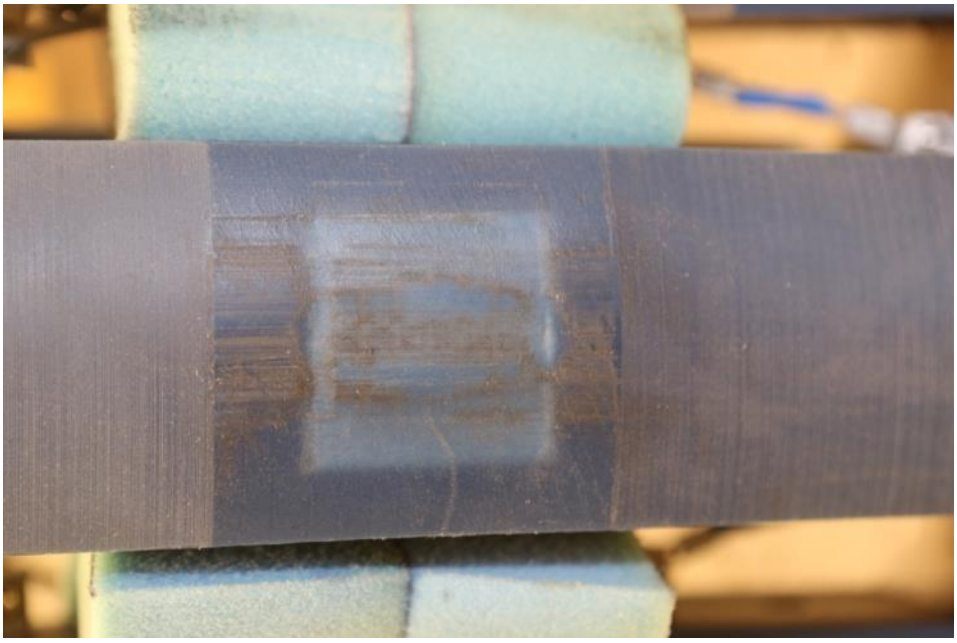

Figure 96. Sensor before the Cycle Test

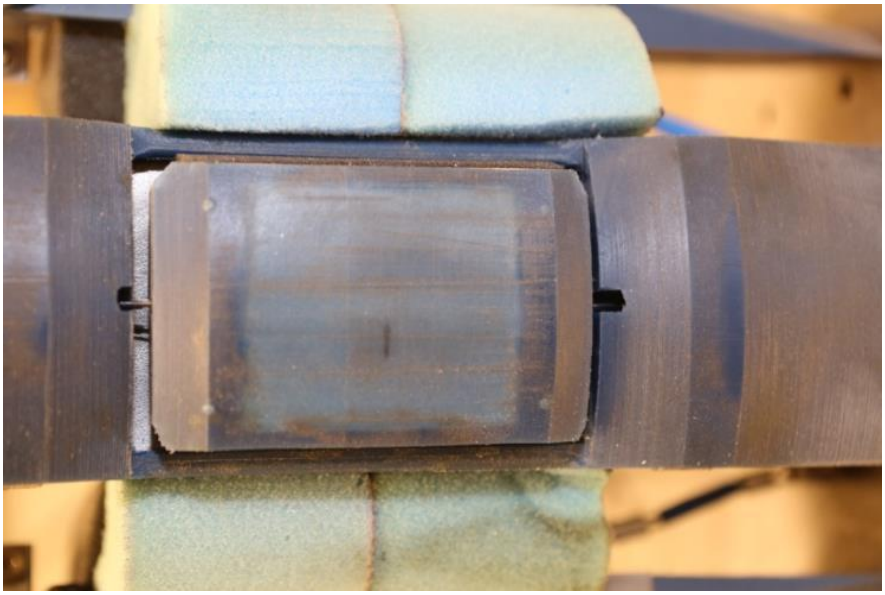

Figure 97. Sensor before the Cycle Test

The bench-scale prototype was cycled 1,030 times representing 1439 meters (4,721 feet) of axial distance and 2,060 cycles across the weld bead. The dummy shoe thickness was 29.90 mm (1.177 inches). This is 0.05 mm (0.002 inches) of wear and is essentially close to the expected measurement variation. As before the cycle testing, there were no deep gouges or wear grooves in the surface. There was nothing that would catch a fingernail sliding across the surface. The surface coloring shows specifically where the sensing surface is rubbing on the pipe ID. The photographs shown in Figure 98 to Figure 103 were taken after this segment of the test.

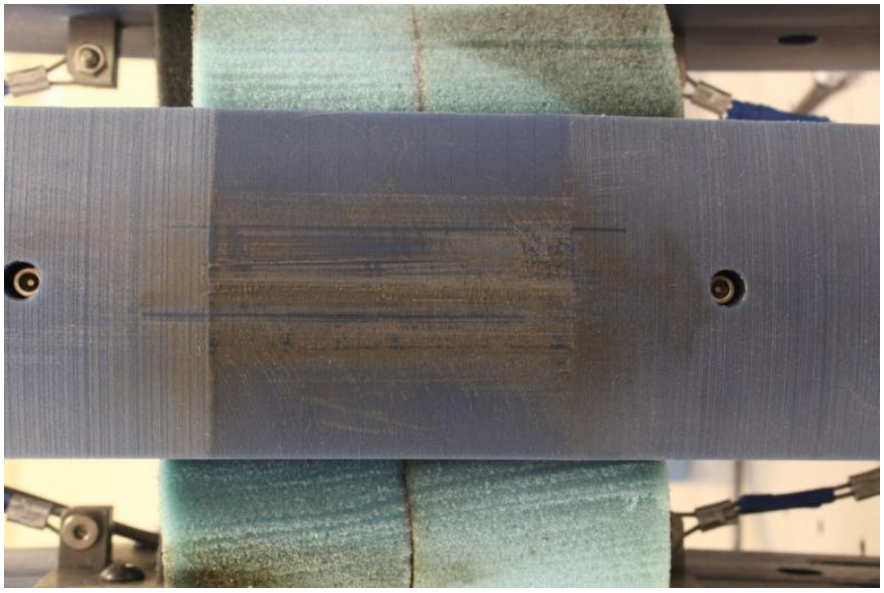

Figure 98. Top View of the Dummy Shoe after 1,439 meters of Axial Travel and 2,060 Weld Bead Transitions

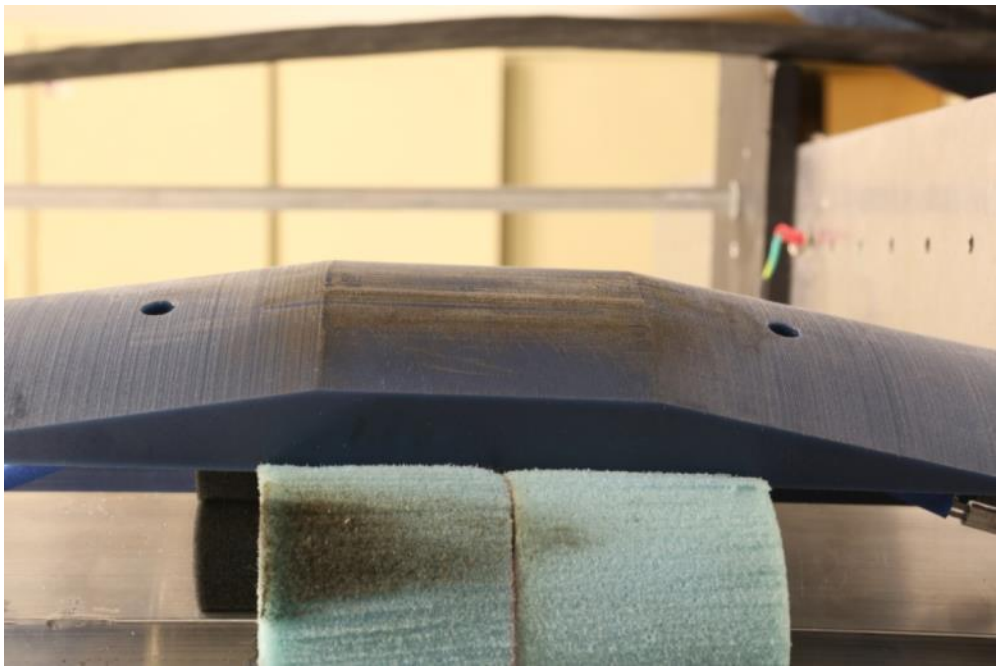

Figure 99. Side View of the Dummy Shoe after 1,439 meters of Axial Travel and 2,060 Weld Bead Transitions

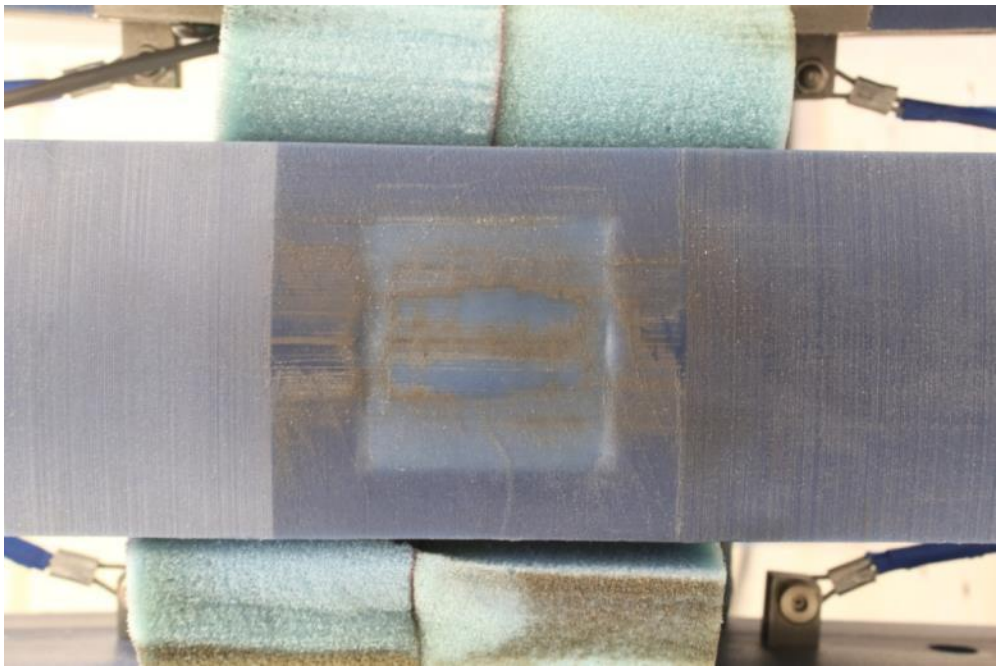

Figure 100. Top View of the Sensor Shoe after 1,439 meters of Axial Travel

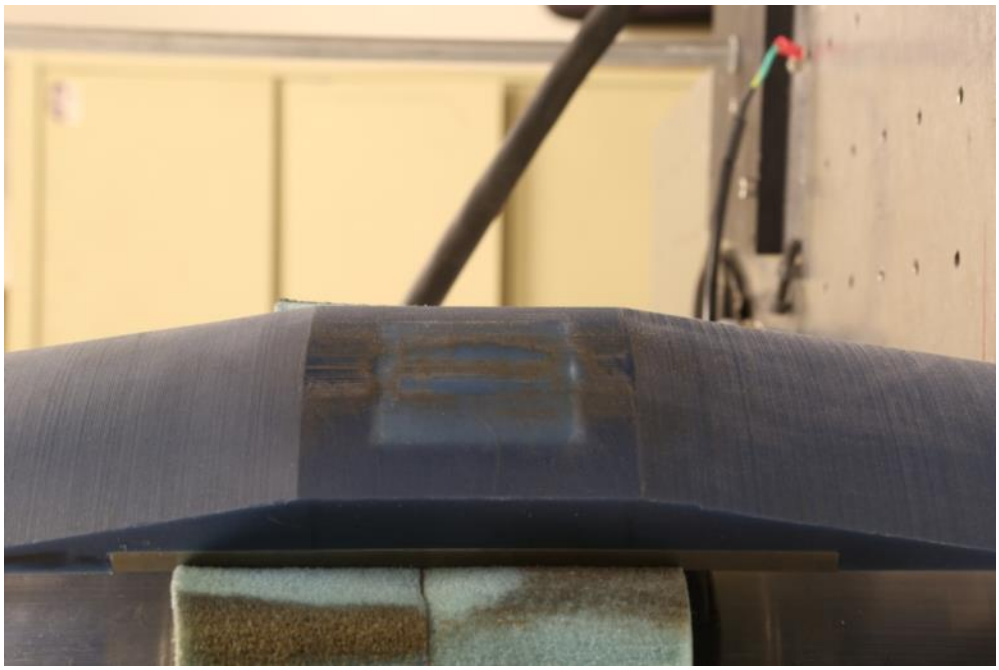

Figure 101. Side View of the Sensor Shoe after 1,439 meters of Axial Travel

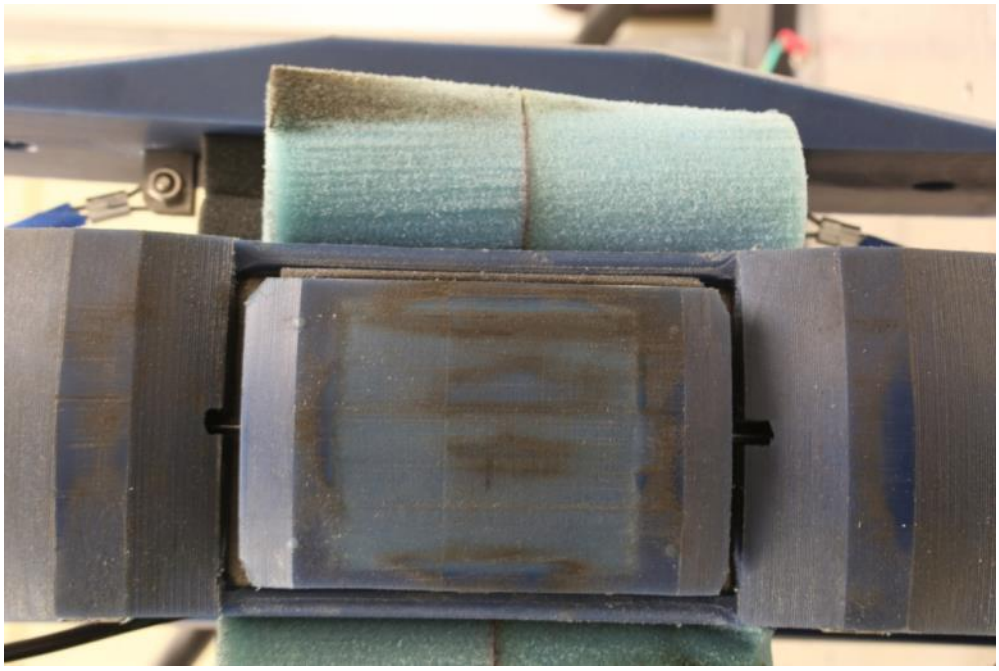

Figure 102. Top View of the Sensor Shoe after 1,439 meters of Axial Travel

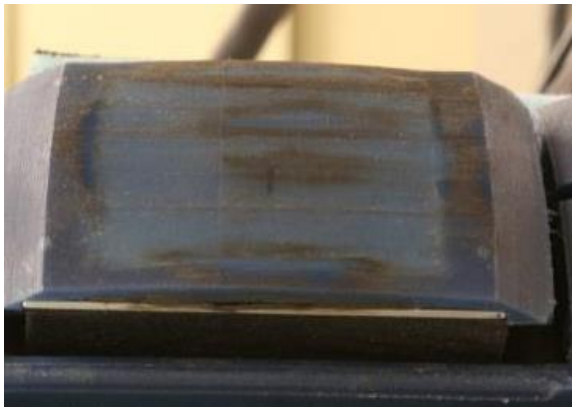

Figure 103. Side View of the Sensor Shoe after 1,439 meters of Axial Travel

The cycle testing was continued for another 2,500 cycles representing an additional 3,492 meters (11,458 feet) of axial distance. Combining the two sets of data, the total axial distance travelled was 4,933 meters (16,179 feet) and the dummy sensor transitioned the weld bead 7,060 times. The measured thickness of the sensor pad was 29.92 mm (1.178 inches). This is thicker than the previous test by 0.02mm, so essentially there was no wear. The fingernail test showed no significant grooving. Also note in the photographs that the transition between the flat sensor area and the sloped portion of the shoe is not distorted between the contact and non-contact area. Figure 104 to Figure 108 are photos of the shoes after the final test segment. The flaw response before the test matched the flaw response after the test.

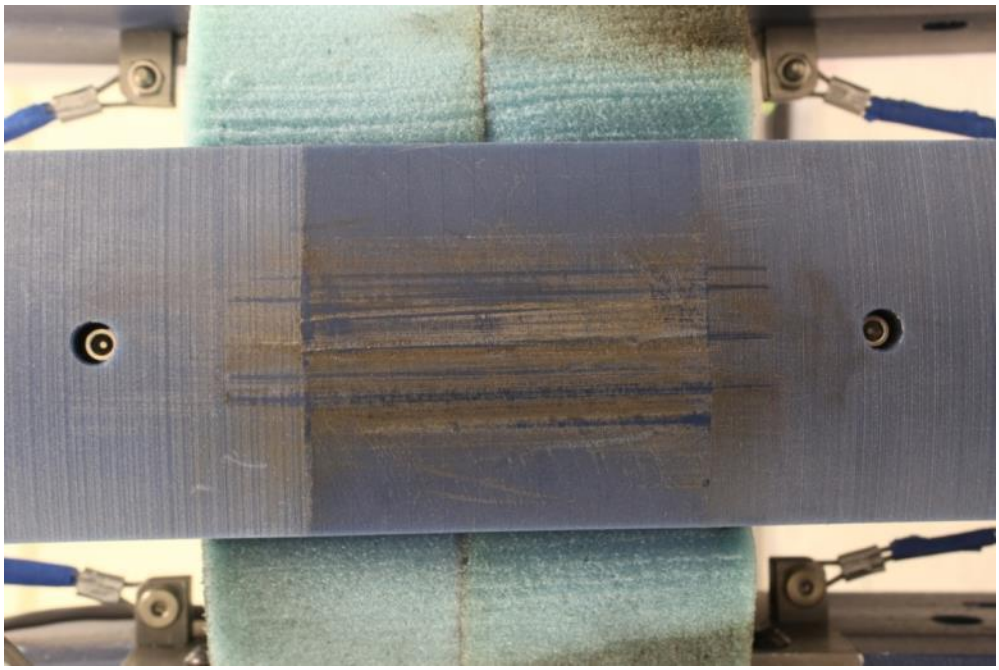

Figure 104. Top View of the Dummy Shoe after 4,933 meters of Axial Travel and 7,060 Weld Bead Transitions

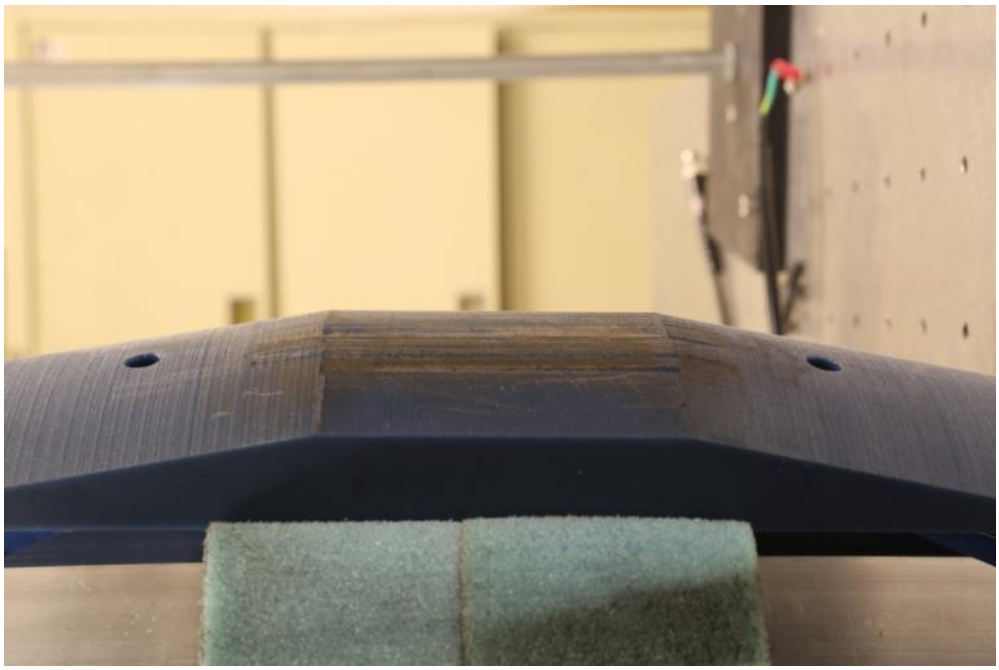

Figure 105. Side View of the Dummy Shoe after 4,933 meters of Axial Travel and 7,060 Weld Bead Transitions

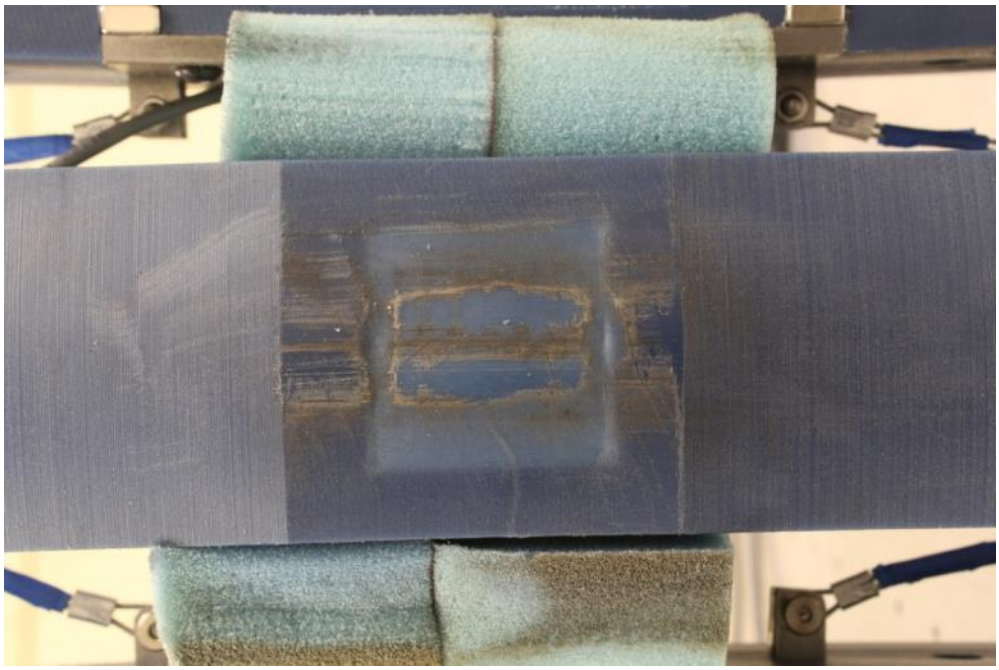

Figure 106. Top View of the Sensor Shoe after 4,933 meters of Axial Travel

Figure 107. Side View of the Sensor Shoe after 4,933 meters of Axial Travel

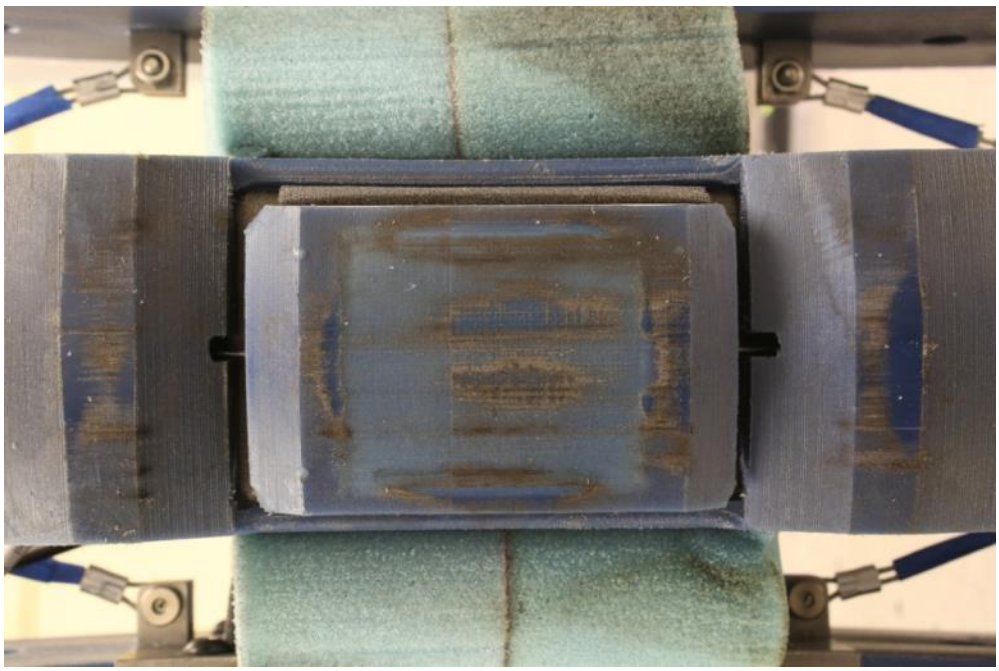

Figure 108. Top View of the Sensor Shoe after 4,933 meters of Axial Travel

7. Recommendations

The recommended next step is to develop the EMAT sensor into a field-ready prototype capable of being tested with various defects and testing conditions in a controlled, unpressurized field environment. Based on controlled field testing, refinements to the sensor would be made in an iterative manner. The sensor could then ultimately be combined onto a platform, and any necessary industry certifications completed, leading up to a field demonstration on a live gas line and commercialization.

END OF REPORT